CMS Draft Analysis Note

2011/07/19
Head Id: 69902
Archive Id: 69994M
Archive Date: 2011/07/18
Archive Tag: trunk

Study of Wγ and Zγ production at CMS with $\sqrt{s}$ = 7 TeV

A.-F. Barfuss[1], T. Bolton[1], A. Bornheim[2], O. Bondu[3], V. Brigljević[4], I. Chakaberia[1], K.-H. Chen[5], S. Dasu[6], S. Duric[4], S. Gascon-Shotkin[3], M. Gataullin[2], L. Gray[6], O. H. Hindrichs[8], F. Raupach[8], A. Kopecky[9], C.-M. Kuo[5], A. Lanaro[6], M. Lethuillier[3], S.-W. Li[5], Z.-K. Liu[5], Y. Maravin[1], T. Miceli[9], H. Newman[2], S. Shrestha[1], I. Svintradze[1], M. Tripathi[9], and J. Veverka[2]

[1] Kansas State University, Manhattan KS, USA
[2] Caltech, Pasadena CA, USA
[3] IPN Lyon/Université Claude Bernard Lyon 1, Villeurbanne, France
[4] Rudjer Boskovic Institute, Zagreb, Croatia
[5] National Central University, Taipei, Taiwan
[6] University of Wisconsin-Madison, Madison WI, USA
[7] University of Delhi,India
[8] RWTH Aachen University, Aachen, Germany
[9] UC Davis, Davis CA, USA

Abstract

We present a study of Wγ and Zγ production in proton-proton collisions at $\sqrt{s}$ = 7 TeV. Results are based on a data sample recorded by the CMS experiment in 2010 and 2011.

This box is only visible in draft mode. Please make sure the values below make sense.

PDFAuthor: C.M. Kuo, Y. Maravin
PDFTitle: Study of Wgamma and Zgamma production at CMS with sqrt"(s") = 7 TeV
PDFSubject: CMS
PDFKeywords: CMS, physics, software, computing

Please also verify that the abstract does not use any user defined symbols

1 Introduction

The self-interactions among the gauge bosons in the standard model (SM) is a direct consequence of the non-Abelian symmetries and their natures, equivalently, the triple and quartic gauge coupling constants (TGC and QGC) are completely fixed in the SM at tree-level. Electroweak measurements at LEP [1–4] Tevatron [5–10], and by several CMS studies [11, 12] with 2010 dataset have already explored some of the parameter space of TGC couplings. As the statistics used in latter CMS analyses was limited, a significant improvement in precision of TGC measurements is expected that will allow testing the SM description of the boson self-interaction at LHC energies. Many extensions of the SM predict additional processes with multiple bosons in the final state, and therefore, any deviation of the observed value from the SM prediction could be an early sign of new physics at high energies. Precise measurements of diboson properties and cross sections are also a crucial step towards understanding the production of major backgrounds of Higgs boson searches at LHC. Among the various diboson processes produced in hadron colliders, $W\gamma$ and $Z\gamma$ have the highest rate. Therefore, the study of these processes allows first tests of diboson production in the electroweak sector of the SM at the LHC.

In this note we report the analysis of inclusive $V\gamma + X$ processes using leptonic decays of $W \to \ell\nu$ and $Z \to \ell\ell$ where $\ell = e, \mu$. The $V\gamma$ productions at tree level can be represented by Feynman diagrams in Figs. 1 and 2 as three processes: initial state radiation (ISR) where a photon is produced from one of the incoming partons, final state radiation (FSR) where a photon is radiated off one of the charged leptons from the V boson decay, and finally when a photon is produced in $s-$channel via TGC $WW\gamma$ for $W\gamma$, and $ZZ\gamma$ and $Z\gamma\gamma$ for $Z\gamma$ production. The last process is allowed only for $W\gamma$ production in the SM, as there are no neutral TGC in the SM.

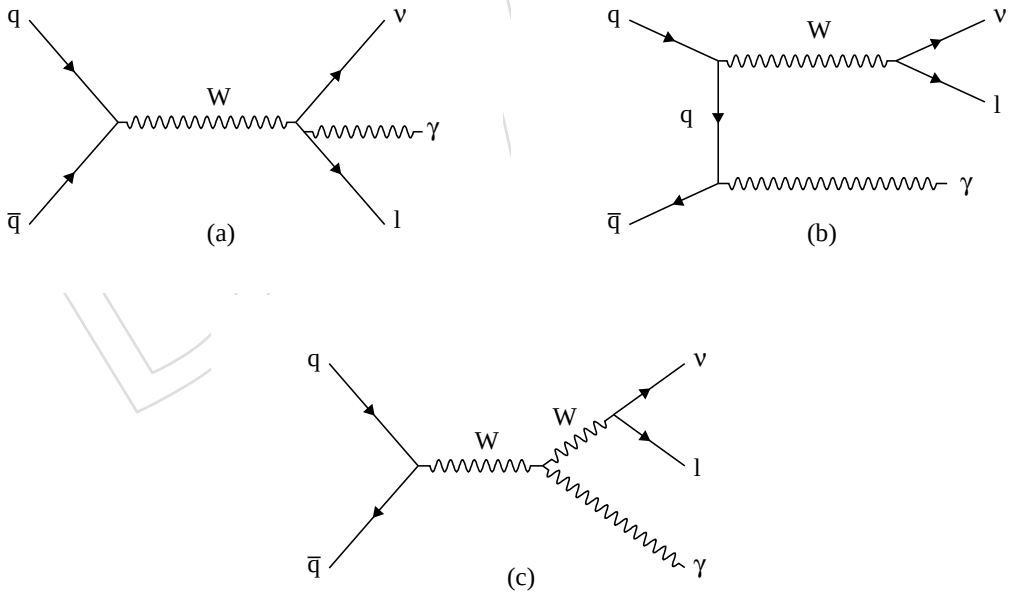

Figure 1: Feynman diagrams of the $W\gamma$ production via final (a) and initial (b) state radiation and via $WW\gamma$ trilinear gauge coupling (c).

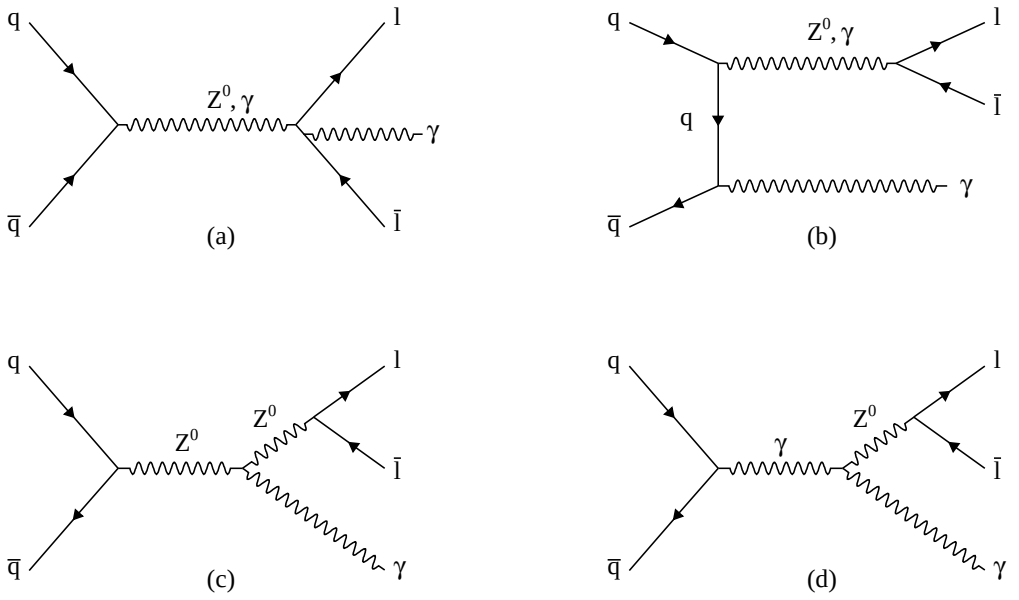

Figure 2: Feynman diagrams of the $Z\gamma$ production via final (a) and initial (b) state radiation, and via the trilinear gauge couplings $ZZ\gamma$ (c) and $Z\gamma\gamma$ (d). The latter two processes are not allowed in the SM.

2 Data and Monte Carlo samples

2.1 Data samples

Information on primary datasets used for this analysis is summarized in Table 1. The official "May10rereco" v1 JSON file *Cert_160404-163869_7TeV_May10ReReco_Collisions11_JSON.txt* and "June17" JSON, *Cert_160404-166861_7TeV_PromptReco_Collisions11_JSON.txt* are applied to "May10rereco" and "PromptReco" v4 AOD, respectively, to select the certified runs and luminosity sections for the analyses. The total integrated luminosity for $W\gamma \to e\nu + \gamma$ and $Z\gamma \to ee + \gamma$ is 715 pb^{-1} and 710.6 pb^{-1} for $W\gamma \to \mu\nu + \gamma$ and $Z\gamma \to \mu\mu + \gamma$, respectively.

The data were reconstructed using *CMSSW_4_2_4_p2* software and analyzed with *CMSSW_4_2_5*.

Table 1: Summary of data samples used for $W\gamma \to \ell\nu\gamma$ and $Z\gamma \to \ell\ell\gamma$ analyses.

CMS Run Range	Dataset Name	Used by
160404 - 163869	/SingleElectron/Run2011A-May10ReReco-v1/AOD	$W\gamma \to e\nu + \gamma$
165071 - 166861	/SingleElectron/Run2011A-PromptReco-v4/AOD	$W\gamma \to e\nu + \gamma$
160404 - 163869	/SingleMuon/Run2011A-May10ReReco-v1/AOD	$W\gamma \to \mu\nu + \gamma$
165071 - 166861	/SingleMuon/Run2011A-PromptReco-v4/AOD	$W\gamma \to \mu\nu + \gamma$
160404 - 163869	/DoubleElectron/Run2011A-May10ReReco-v1/AOD	$Z\gamma \to ee + \gamma$
165071 - 166861	/DoubleElectron/Run2011A-PromptReco-v4/AOD	$Z\gamma \to ee + \gamma$
160404 - 163869	/DoubleMuon/Run2011A-May10ReReco-v1/AOD	$Z\gamma \to \mu\mu + \gamma$
165071 - 166861	/DoubleMuon/Run2011A-PromptReco-v4/AOD	$Z\gamma \to \mu\mu + \gamma$

2.2 Monte Carlo samples

Information on Monte Carlo samples used for the analyses is given in Tables 2 and 3 for signal and background simulations, respectively. The corresponding leading order (LO) and next-to-leading order (NLO) cross sections are also listed in these Tables.

The signal samples used for the cross section measurement are generated privately using MADGRAPH with the following generator-level requirements: $E_T^\gamma > 5(5)$ GeV, $p_T^\ell > 30(5)$ GeV, $|\eta^\ell| < 3(3)$, $|\eta^\gamma| < 3(3)$, $p_T^{parton} > 10(10)$ GeV, and a spatial separation between a photon and any charged lepton in the final state $\Delta R(\ell,\gamma) > 0.6(0.6)$ for $W\gamma(Z\gamma)$. An additional requirement on the dilepton invariant mass of $M_{\ell\ell} > 40$ GeV is used in the generation of the $Z\gamma$ sample. For the signal samples, the cross sections are scaled to NLO using the NLO cross sections extracted from MCFM.

The cross sections for background processes are given at NLO, except for the γ+jets and multijet QCD samples. All MC simulation samples are produced officially in Summer11 production. Events are simulated with 50 ns bunch spacing and out-of-time (OOT) pileup is also included. Multijet QCD and γ+jets samples are simulated with asynchronous OOT ("S3") pileup scenario, and the rest background MC samples are simulated with synchronous OOT ("S4") pileup scenario.

Table 2: Summary of Monte Carlo signal samples used.

Process	$\sigma_{MadGraph}$, pb	σ_{NLO}, pb
$W \to e\nu + \gamma$	16.6	21.41
$W \to \mu\nu + \gamma$	16.6	21.41
$Z \to ee + \gamma$	11.15	13.79
$Z \to \mu\mu + \gamma$	11.12	13.79

Table 3: Summary of Monte Carlo background samples used.

Process	σ, pb	Dataset Name (AODSIM data tier)
$W \to l\nu + jets$	31314	/WJetsToLNu_TuneZ2_7TeV-madgraph-tauola
$Z \to ll + jets$	3048	/DYJetsToLL_TuneZ2_M-50_7TeV-madgraph-tauola
$t\bar{t} + jets$	157.5	/TTJets_TuneZ2_7TeV-madgraph-tauola
WW	5.7	/WWTo2L2Nu_TuneZ2_7TeV_pythia6_tauola
WZ	0.6	/WZTo3LNu_TuneZ2_7TeV_pythia6_tauola
ZZ	0.06	/ZZTo2L2Nu_TuneZ2_7TeV_pythia6_tauola
$\gamma + jets(\hat{p_T} : 0-15)$	8.420×10^7	/G_Pt_0to15_TuneZ2_7TeV_pythia6
$\gamma + jets(\hat{p_T} : 15-30)$	1.717×10^5	/G_Pt_15to30_TuneZ2_7TeV_pythia6
$\gamma + jets(\hat{p_T} : 30-50)$	1.669×10^4	/G_Pt_30to50_TuneZ2_7TeV_pythia6
$\gamma + jets(\hat{p_T} : 50-80)$	2.722×10^3	/G_Pt_50to80_TuneZ2_7TeV_pythia6
$\gamma + jets(\hat{p_T} : 80-120)$	4.472×10^2	/G_Pt_80to120_TuneZ2_7TeV_pythia6
$\gamma + jets(\hat{p_T} : 120-170)$	8.417×10^1	/G_Pt_120to170_TuneZ2_7TeV_pythia6
$\gamma + jets(\hat{p_T} : 170-300)$	2.264×10^1	/G_Pt_170to300_TuneZ2_7TeV_pythia6
$\gamma + jets(\hat{p_T} : 300-470)$	1.493	/G_Pt_300to470_TuneZ2_7TeV_pythia6
$QCD(\hat{p_T} : 5-15)$	3.675×10^{10}	/QCD_Pt_5to15_TuneZ2_7TeV_pythia6
$QCD(\hat{p_T} : 15-30)$	8.159×10^8	/QCD_Pt_15to30_TuneZ2_7TeV_pythia6
$QCD(\hat{p_T} : 30-50)$	5.312×10^7	/QCD_Pt_30to50_TuneZ2_7TeV_pythia6
$QCD(\hat{p_T} : 50-80)$	6.359×10^6	/QCD_Pt_50to80_TuneZ2_7TeV_pythia6
$QCD(\hat{p_T} : 80-120)$	7.843×10^5	/QCD_Pt_80to120_TuneZ2_7TeV_pythia6
$QCD(\hat{p_T} : 120-170)$	1.151×10^5	/QCD_Pt_120to170_TuneZ2_7TeV_pythia6
$QCD(\hat{p_T} : 170-300)$	2.426×10^4	/QCD_Pt_170to300_TuneZ2_7TeV_pythia6
$QCD(\hat{p_T} : 300-470)$	1.168×10^3	/QCD_Pt_300to470_TuneZ2_7TeV_pythia6
$QCD(\hat{p_T} : 470-600)$	7.022×10^1	/QCD_Pt-470to600_TuneZ2_7TeV_pythia6
$QCD(\hat{p_T} > 20)$	84679.3	/QCD_Pt-20_MuEnrichedPt-15_TuneZ2_7TeV_pythia

3 Object selection

In this Section we document the High Level Trigger (HLT) paths used to trigger candidate events; the electron, muon, and photon identification and isolation criteria, and provide the results of comparing Monte Carlo simulation with data.

3.1 Triggers

3.1.1 Electron triggers

The $W\gamma \to e\nu\gamma$ and $Z\gamma \to ee\gamma$ final states are triggered by unprescaled electron triggers with the lowest threshold available. These triggers seeded by the ECAL L1 triggers with $E_T >$ 15 GeV (L1_SingleEG15) or with $E_T > 20$ GeV (L1_SingleEG20). The run history of the relevant triggers together with the identification and isolation requirements are given in Tables 4, 6, 5 and 7, respectively.

Table 4: Single electron trigger requirement used for the different run ranges.

Run range	L1 threshold	HLT threshold	HLT path	Luminosity (pb^{-1})
160431-161176	15	27	HLT_Ele27_CaloIdVT_CaloIsoT_TrkIdT_TrkIsoT_v1	6.4
161217-163261	15	27	HLT_Ele27_CaloIdVT_CaloIsoT_TrkIdT_TrkIsoT_v2	38.5
163270-163869	15	27	HLT_Ele27_CaloIdVT_CaloIsoT_TrkIdT_TrkIsoT_v3	159.8
165088-165633	20	32	HLT_Ele32_CaloIdVT_CaloIsoT_TrkIdT_TrkIsoT_v3	133.3
165970-166861	20	32	HLT_Ele32_CaloIdVT_CaloIsoT_TrkIdT_TrkIsoT_v4	385.9

Table 5: Double electron trigger requirement used for the different run ranges.

Run range	L1 threshold	HLT path	Luminosity (pb^{-1})
160431-161176	12	HLT_Ele17_CaloIdL_CaloIsoVL_Ele8_CaloIdL_CaloIsoVL_v1	6.4
161217-163261	12	HLT_Ele17_CaloIdL_CaloIsoVL_Ele8_CaloIdL_CaloIsoVL_v2	38.5
163270-163869	12	HLT_Ele17_CaloIdL_CaloIsoVL_Ele8_CaloIdL_CaloIsoVL_v3	159.8
165088-165633	12	HLT_Ele17_CaloIdL_CaloIsoVL_Ele8_CaloIdL_CaloIsoVL_v4	133.3
165970-166861	12	HLT_Ele17_CaloIdL_CaloIsoVL_Ele8_CaloIdL_CaloIsoVL_v5	385.9

Table 6: The summary of calorimeter identification for single electron triggers. Here (EB) and (EE) stand for barrel and endcap portions of the ECAL, respectively.

H/E	$\Delta\eta_{in}$	$\Delta\phi_{in}$	$\sigma_{i\eta i\eta}$
0.05	0.008 (EB) 0.008 (EE)	0.07 (EB) 0.05 (EE)	0.011 (EB) 0.031 (EE)

The performance of these triggers and comparisons of simulation with data is given below in Section 3.2.1.

3.1.2 Muon triggers

The $W\gamma \to \mu\nu\gamma$ process is selected using `HLT_Mu30_v*`for the entire run period presented in this note, it is seeded by `L1_SingleMu12`. The $Z\gamma \to \mu\mu\gamma$ processes are triggered using both muons of the Z boson decay by using the double muon triggers `HLT_DoubleMu7_v*` and `HLT_Mu13_Mu8_v*` the latter being the lowest unprescaled double muon trigger after the LHC achieved $10^{33}/cm^2/s$. While both triggers are seeded by `L1_DoubleMu3`, the second double muon trigger has an additional L2 (muon system only) p_{T} requirement of 7 GeV on the muon which passes the 13 GeV L3 (tracker + muon system) leg of `HLT_Mu13_Mu8_v*`.

The performance of these triggers and comparison of simulation with data is given below in Section 3.3.1.

Table 7: The summary of isolation requirements for single electron trigger. Here (EB) and (EE) stand for barrel and endcap portions of the ECAL, respectively.

$Iso_{ECAL}/E_{\mathrm{T}}$	$Iso_{HCAL}/E_{\mathrm{T}}$	Iso_{TRK}/E_{T}
0.125 (EB) 0.075 (EE)	0.125 (EB) 0.075 (EE)	0.125 (EB) 0.075 (EE)

Table 8: Trigger history for $\mu\nu\gamma$ and $\mu\mu\gamma$ final states in the SingleMu primary dataset.

Run	Trigger	Integrated luminosity (pb^{-1})
From 160404 to 166861	`HLT_Mu30_v*`	706.4
From 160404 to 163869	`HLT_DoubleMu7_v*`	199.8
From 165088 to 166861	`HLT_Mu13_Mu8_v*`	506.6

3.2 Electron selection

In this analysis we consider electrons with the identification and isolation optimized using Spring11 MC samples. The optimization procedure was the used in previous analyses that studied $W \to e\nu$ and $Z \to ee$ production [**?**]. We summarize electron identification and isolation requirements below.

The ECAL fiducial region is defined in terms of barrel and endcap sections with pseudorapidity ranges of $|\eta| < 1.4442$ and $1.566 < |\eta| < 3.0$, respectively. An electron is considered to be within this ECAL acceptance if its associated SuperCluster (SC) is within the ECAL acceptance.

Electron identification comprises of cuts on a cluster shape variable ($\sigma_{i\eta i\eta}$), and on track-cluster matching variables ($\Delta\phi_{in}$ and $\Delta\eta_{in}$). Due to pileup effect, the hadronic activity behind the cluster (H/E) is included in HCAL isolation (I_{HCAL}). Electrons from photon conversions are suppressed by requiring that the electron track has no missing tracker hits before the first hit in the reconstructed track assigned to the electron. Furthermore, electrons are rejected when a partner track is found which is consistent with a photon conversion, based on the opening angle, the separation in the transverse plane, and the point at which the electron and partner tracks are parallel (Dcot and Dist). Electron isolation is comprises of cuts on the combined relative isolation with fastjet correction ($(I_{\mathrm{HCAL}} + I_{\mathrm{ECAL}} + I_{\mathrm{trk}} - \rho \times \pi \times \Delta R^2)/E_T$). In order to suppress the faked electron from pileup, vertex d_0 should be less than 0.02 cm and vertex d_z should be less than 0.1 cm.

We consider three electron selection working points, WP80, WP85 and WP95, which have been obtained by optimizing simultaneously identification and isolation criteria in the Monte Carlo simulation, and giving approximately 80%, 85% and 95% selection efficiency, respectively. The WP80 selection gives a purer sample of prompt electrons, and is used for $W\gamma$, while the looser WP85 selection is used for the $Z\gamma$ analysis. The values of the cuts for WP80, WP85 and WP95 are listed in Table 9.

3.2.1 Performance of electron triggers and electron selection criteria

The performance of the electron triggers and the electron selection criteria are estimated using the tag and probe method using electrons from $Z \to ee$ production. The events for this study are selected using one of the single electron triggers described in Section 3.1.1 and with a requirement that at least one tag electron passes the stringent selection requirements:

- must have $p_T^e > 35$ GeV and be in the ECAL fiducial region,
- must pass WP80 selection criteria,

Table 9: Selection criteria for the WP80, WP85 and WP95 electron candidates in Barrel and Endcap sections of the calorimeter.

	WP95		WP85		WP80	
	Barrel	Endcap	Barrel	Endcap	Barrel	Endcap
Combined relative isolation	0.15	0.1	0.053	0.042	0.04	0.033
Missing hits $\leq$	0	0	0	0	0	0
Dcot	–	–	0.02	0.02	0.02	0.02
Dist	–	–	0.02	0.02	0.02	0.02
$\sigma_{i\eta i\eta}$	0.012	0.031	0.01	0.031	0.01	0.031
$\Delta\phi_{in}$	0.8	0.7	0.039	0.028	0.027	0.021
$\Delta\eta_{in}$	0.007	0.011	0.005	0.007	0.005	0.006

- must satisfy unprescaled electron trigger.

We also require events to have at least one additional SuperCluster reconstructed within the ECAL acceptance. The events are further pre-selected by requiring the invariant mass of the tag and probe pair to be consistent with the Z boson mass, *i.e.* within 80 and 120 GeV. We do not require the tag and probe electron candidates to have opposite electric charges.

The following definitions of probe electron and the passing criteria are used to study reconstruction, selection, and trigger efficiencies:

- *Reconstruction efficiency* We require the probe SuperCluster to pass the following additional cleaning requirements:
  - $H/E < 0.15$ for EB, and < 0.07 for EE,
  - $\sigma_{i\eta i\eta} < 0.01$ for EB, and < 0.03 for EE.

  The passing probe is defined as a probe spatially matched to a reconstructed GsfElectron.
- *Selection efficiency* The probe SuperCluster is spatially matched to the GsfElectron with $p_T > 35(20)$ GeV. A passing probe must satisfy the WP80 (WP85) criteria.
- *Trigger efficiency* The probe SuperCluster is spatially matched to the GsfElectron with $p_T > 35(20)$ GeV, and passes the electron WP80 (WP85) selection. A passing probe must satisfy the trigger requirements.

After applying the dielectron invariant mass cut some events are left with more than one Z candidate. In the case that there is more than one Z candidate to choose from, we make the following arbitration. We consider only those events which have at least one tag candidate.

If the event has two probe electrons, and only one of them passes the tag criteria, we choose that electron for the probe. If the event has two probe electrons and both of them either pass or fail tag requirements together, we choose one of these electrons randomly. If the event contains more than two probe candidates, the event is vetoed.

We take into account tag and probe permutations in both numerator and denominator of the efficiency calculation formula, *i.e.*, the events with both electrons passing tag criteria contribute twice in numerator and in denominator.

The number of Z boson candidates is determined from the invariant mass distribution fit to the convolution of a Breit-Wigner and a Crystal Ball function for signal and an exponential function for modeling the background. The counting method is used to compute the trigger efficiency because we assume there is no background to the $Z \to ee$ candidate events after applying the

Table 10: Summary of the measured efficiencies in data, MC simulation, and a data/simulation ratio for electron recontruction ϵ_{RECO}; selection ϵ_{WP80} and ϵ_{WP85}; and trigger efficiencies with respect to reconstructed electrons passing WP80, ϵ_{TRG80}; and WP85, ϵ_{TRG85}.

Efficiency	Data	Simulation	Data/Simulation
Barrel ECAL			
ϵ_{RECO}	$99.2\% \pm 0.02\%$	99.3%	0.999 ± 0.001
ϵ_{WP80}	$85.5\% \pm 0.1\%$	86.7%	0.986 ± 0.001
ϵ_{WP85}	$88.0\% \pm 0.09\%$	88.8%	0.991 ± 0.0013
ϵ_{TRG80}	$97.7\% \pm 0.1\%$	98.2%	0.995 ± 0.001
ϵ_{TRG85}	-	-	-
Endcap ECAL			
ϵ_{RECO}	$98.2\% \pm 0.03\%$	98.4%	0.998 ± 0.001
ϵ_{WP80}	$73.7\% \pm 0.2\%$	74.0%	0.996 ± 0.003
ϵ_{WP85}	80.41 ± 0.035	80.6%	0.9975 ± 0.004
ϵ_{TRG80}	$97.0\% \pm 0.1\%$	98.2%	0.993 ± 0.001
ϵ_{TRG85}	-	-	-

Description	criterion
Kinematical (loose)	$p_T > 20$ GeV and $\lvert\eta\rvert < 2.4$
Kinematical (tight)	$p_T > 35$ GeV and $\lvert\eta\rvert < 2.1$
Number of pixel hits	> 0
Number of tracker hits	> 10
χ^2/n.d.f	< 10
Number of muon hits	> 0
Number of chambers with matched segments	> 1
vertex d_0	< 0.02 cm
vertex d_z	< 0.1 cm
combined relative isolation	< 0.1

Table 11: Muon identification and isolation requirements. The loose selection is used to identify muons from Z candidates, while the tight selection is used for the W candidates.

full WP80 (WP85) selection criteria on both of the electron candidates. The trigger efficiency from MC is only for the HLT path HLT_Ele32_CaloIdVT_CaloIsoT_TrkIdT_TrkIsoT. These electron reconstruction, WP80, WP85 selection and HLT efficiencies are given Figs. **??**, 4, 5, and **??**, respectively.

The resultant efficiencies in data and simulation are given in Table 10 together with a ratio of efficiencies in the data and the simulation.

3.3 Muon selection

The events for $W\gamma \to \mu\nu\gamma$ channel are selected by requiring the events to fire the single muon trigger `HLT_Mu30_v*`, which is unprescaled for the run period being examined. The triggers required for $Z\gamma \to \mu\mu\gamma$ are `HLT_DoubleMu7_v*` and `HLT_Mu13_Mu8_v*`, the former becoming prescaled after the first $200 pb^{-1}$ of integrated luminosity in 2011.

Furthermore, the muons in $Z\gamma$ ($W\gamma$) are required to pass loose (tight) kinematical requirements as well as identification criteria.

Cosmic ray muon contamination is significantly reduced by the requirement of $|d_{xy}|$ and $|d_z|$

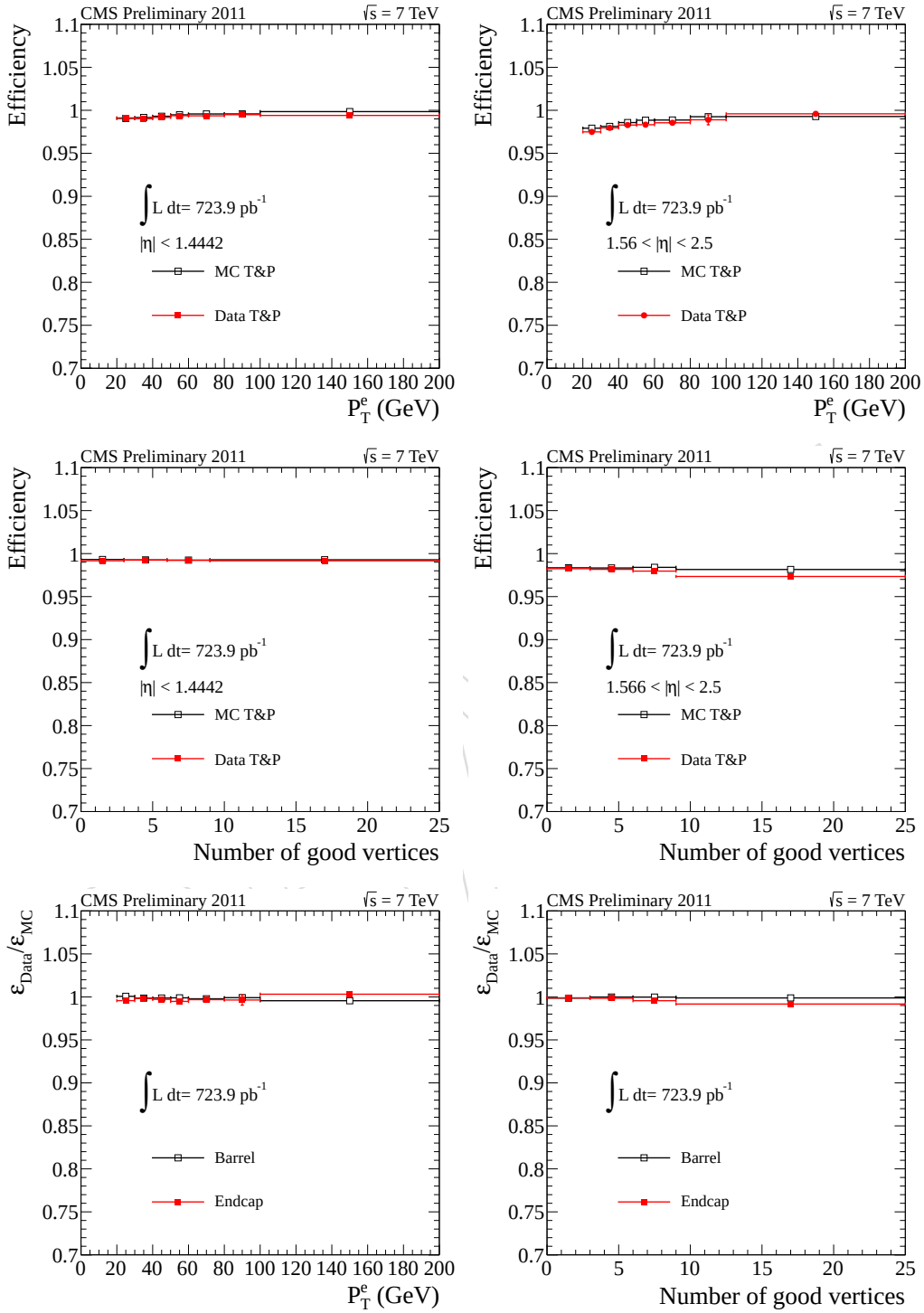

Figure 3: A p_T-dependent and verteices-dependent electron reconstruction efficiencies in the data and MC for barrel and endcap.

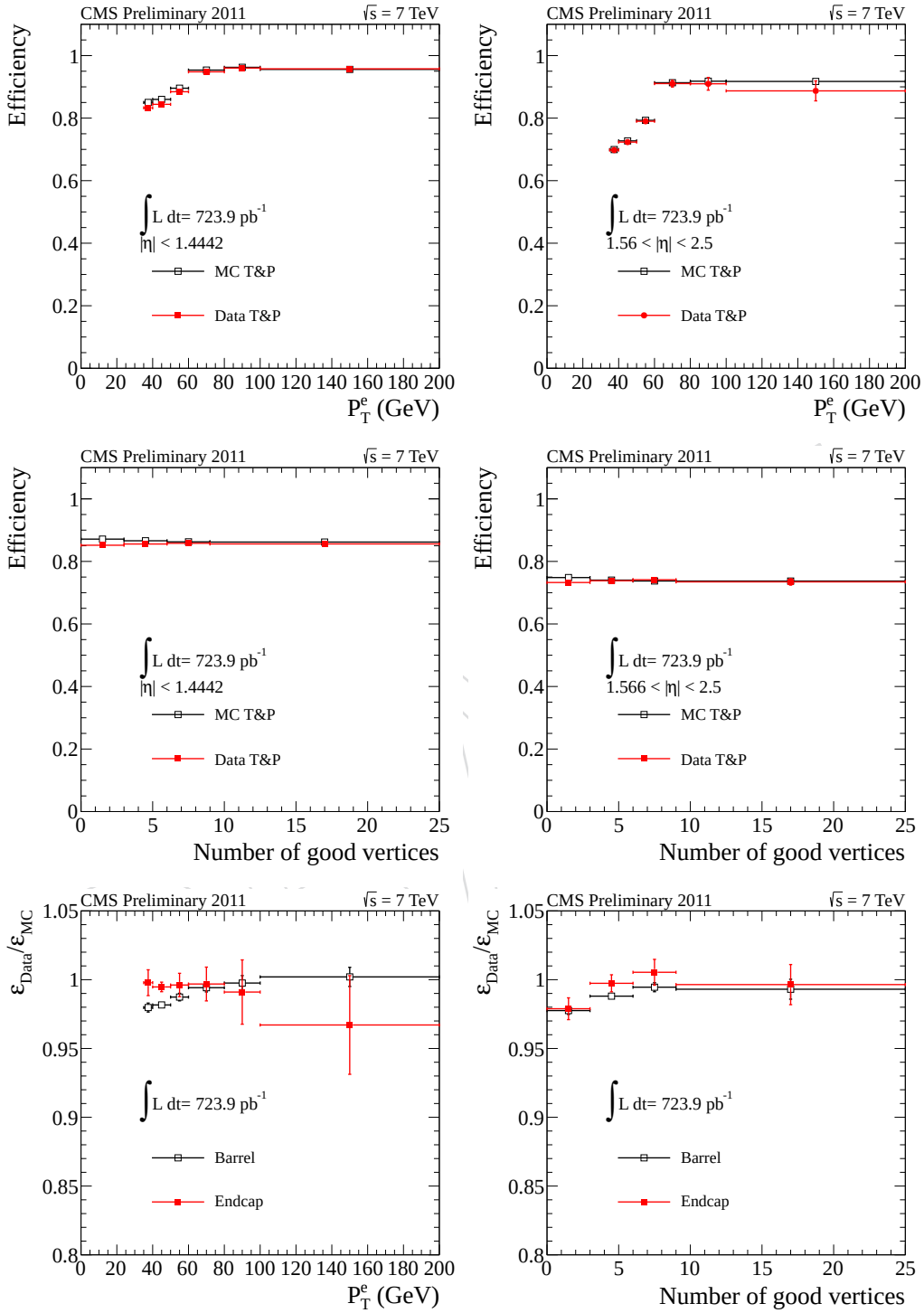

Figure 4: A p_T-dependent and verteices-dependent electron WP80 efficiencies in the data and MC for barrel and endcap.

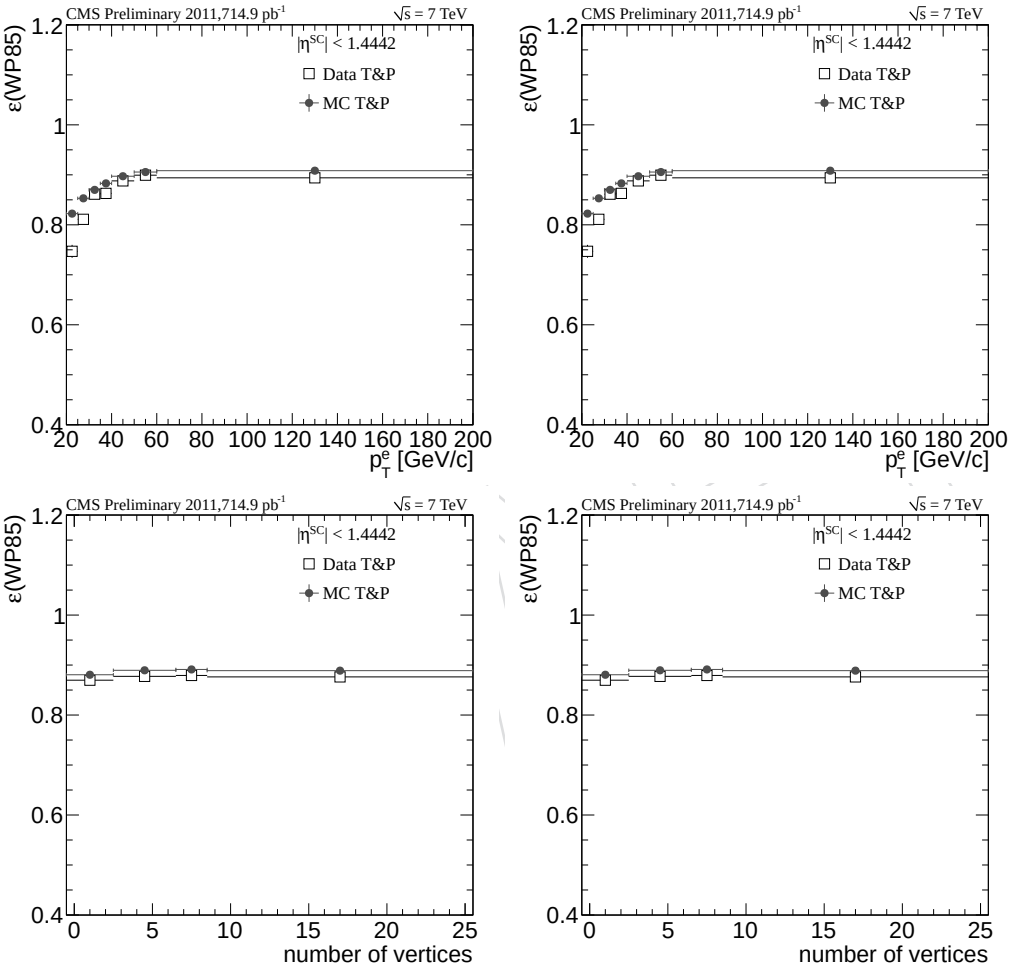

Figure 5: A p_{T}-dependent and verteices-dependent electron WP85 efficiencies in the data and MC for barrel and endcap.

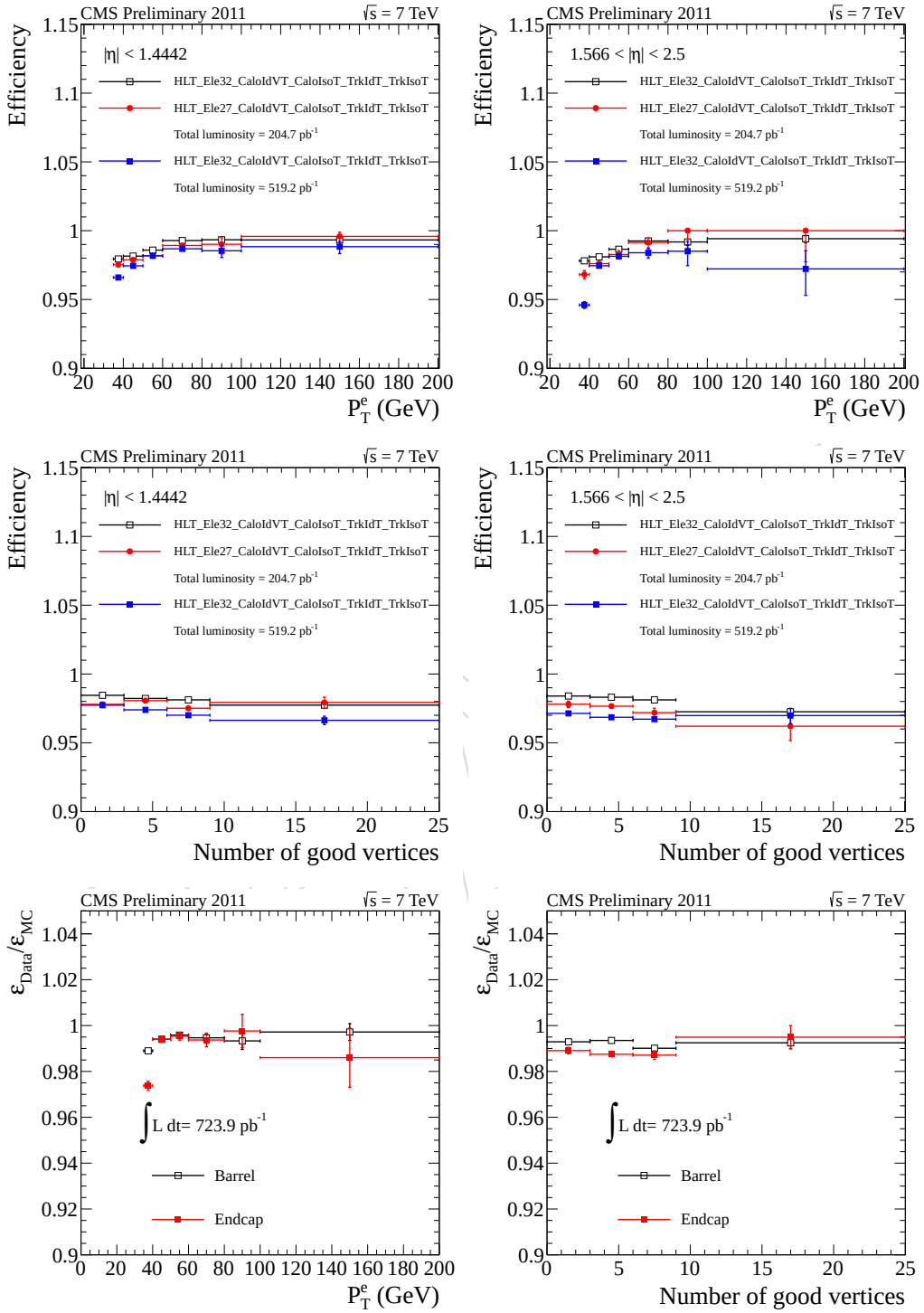

Figure 6: A p_T-dependent and verteices-dependent HLT efficiencies in the data and MC for barrel and endcap.

to be consistent with the prompt muon production. Further cross-checks of timing and cosmic tagger information [**?**] indicate negligible contribution from the cosmic background.

3.3.1 Performance of muon triggers and muon selection criteria

The performance of muon triggers and the overall muon reconstruction criteria is estimated using the tag and probe method.

The overall muon identification efficiency is factorized as a product of efficiencies of several consecutively applied requirements:

$$\epsilon_{tot} = \epsilon_{TRK} \cdot \epsilon_{SA} \cdot \epsilon_{ID} \cdot \epsilon_{ISO} \cdot \epsilon_{HLT}, \quad (1)$$

where individual efficiencies are defined below:

- ϵ_{TRK}: the efficiency of reconstructing a track in the Tracker with the required number of pixel and tracker hits,
- ϵ_{SA}: the efficiency of reconstructing a track in the muon system, *i.e.*, a stand-alone (SA) muon with at least two muon stations and one matched chamber hit,
- ϵ_{ID}: the efficiency of passing the GlobalMuon and TrackerMuon algorithms with the required cuts on $|d_{xy}|$, $|d_z|$ and χ^2/n.d.f,
- ϵ_{ISO}: the efficiency of passing the required isolation,
- ϵ_{HLT}: the efficiency of satisfying the requirements of the single muon trigger or double muon trigger leg.

As the requirements are applied sequentially, the efficiency for both data and MC simulation is estimated with respect to the previously applied criteria. ϵ_{TRK} is approximated by the efficiency of reconstructing a track given a stand-alone muon. For simplicity of implementation in the case of the dimuon triggers, the harder muon is required to pass the harder leg of the dimuon trigger. Given that the loose p_T requirement is at 20 GeV for each muon, the efficiency loss due to this construction is minimal.

3.3.2 Tag and Probe method

The tag is defined as a muon that satisfies all muon selection criteria and is matched with a trigger object. There is no requirement on the charge of the tag as to avoid ambiguousness of the tag selection. The probes are defined to estimate each of the individual efficiencies defined by Eq. 1 with definitions and passing criterion summarized in Table 12. All probes together with the tag are supposed have an invariant mass 60 GeV$< M_{TP} <$ 120 GeV and the opposite charge.

Table 12: Definition of selected probes and the passing criterion.

ϵ	Probe definition	Passing criteria
TRK	SA muon	Track in Tracker
SA	Track in Tracker	SA muon
ID	Track in Tracker and SA muon	Global/Tracker muon
ISO	Global/Tracker muon	Isolated Global/Tracker muon
HLT	Isolated Global/Tracker muon	Isolated Global/Tracker muon matched to HLT

The efficiency is determined by measuring the number of Z boson candidates in passing and failing categories by fitting the dimuon invariant mass distribution in the requisite mass range. The signal shape is described by a Breit-Wigner distribution convoluted with a Crystal Ball function where its width is fixed to the width of the Z boson as determined by the PDG global average. The Crystal Ball function is numerically convoluted with the Breit-Wigner function to account for detector resolution and final state radiation effects in measured distribution. The background is described by an exponential function.

The results for the overall muon identification efficiency of the selected probes are given in Table 13 together with the Monte Carlo results of tag and probe method and those obtained using the Monte Carlo truth information.

The same method is used to get results for the efficiencies as a function of p_{T} and η of the probe and as a function of the number of primary vertices in the event. The latter gives the direct estimate of the pile up dependence, which is found to be minimal. The results are shown in Figs. 7 through 11.

3.4 Photon selection

Photon candidates are reconstructed as SuperClusters with $E_T > 15$ GeV in the fiducial volume of the ECAL detector: barrel (EB) with $|\eta| < 1.44$ and endcap (EE) with $1.57 < |\eta| < 2.5$. The efficiency of identification of photons as SuperClusters is measured in MC simulation and is found to be very close to 100%.

To reduce copious background objects from jets misidentified as photons we apply the same identification, except for η-width in EB, and isolation criteria used in the first Vγ paper [12]:

- Jurassic ECAL isolation $< 4.2 + 0.006\ E_T^{\gamma}$; this isolation variable is built by summing the transverse energy deposited in the ECAL in an annulus $0.06 < R < 0.40$, excluding a rectangular strip of $\Delta\eta \times \Delta\phi = 0.04 \times 0.40$.
- Tower-based HCAL isolation $< 2.2 + 0.0025\ E_T^{\gamma}$,
- Hadronic/EM < 0.05,
- Hollow cone track isolation $< 2 + 0.001\ E_T^{\gamma}$,
- η-width < 0.011 (EB), < 0.030 (EE),
- Track veto: require no pixel seeds.

The η-width requirement in EB is tighter than the one used in the previous CMS analysis [12] to increase the purity of the signal and populate the background sideband for the ratio method of estimation the V+jet background. The other change from the photon identification is the correction of the isolation ρ due to pile-up events:

$$Iso^{new} = Iso^{original} - \rho_{event} \times \frac{< Iso >}{< \rho >} \tag{2}$$

, where $\frac{<Iso>}{<\rho>}$ is also called A_{eff}, where ρ is the median background density per unit area and computed using FASTJET package [**?**]. **I do not really understand what is given below. How can you use acceptance for pile-up correction? You can use acceptance to measure the cross section. Please revise!**

Comparison of corrected photon isolation variable shapes for data and MC simulation after applying full selection criteria is shown in Fig. 12. The results are in good agreement between data and MC simulation for all three isolation variables.

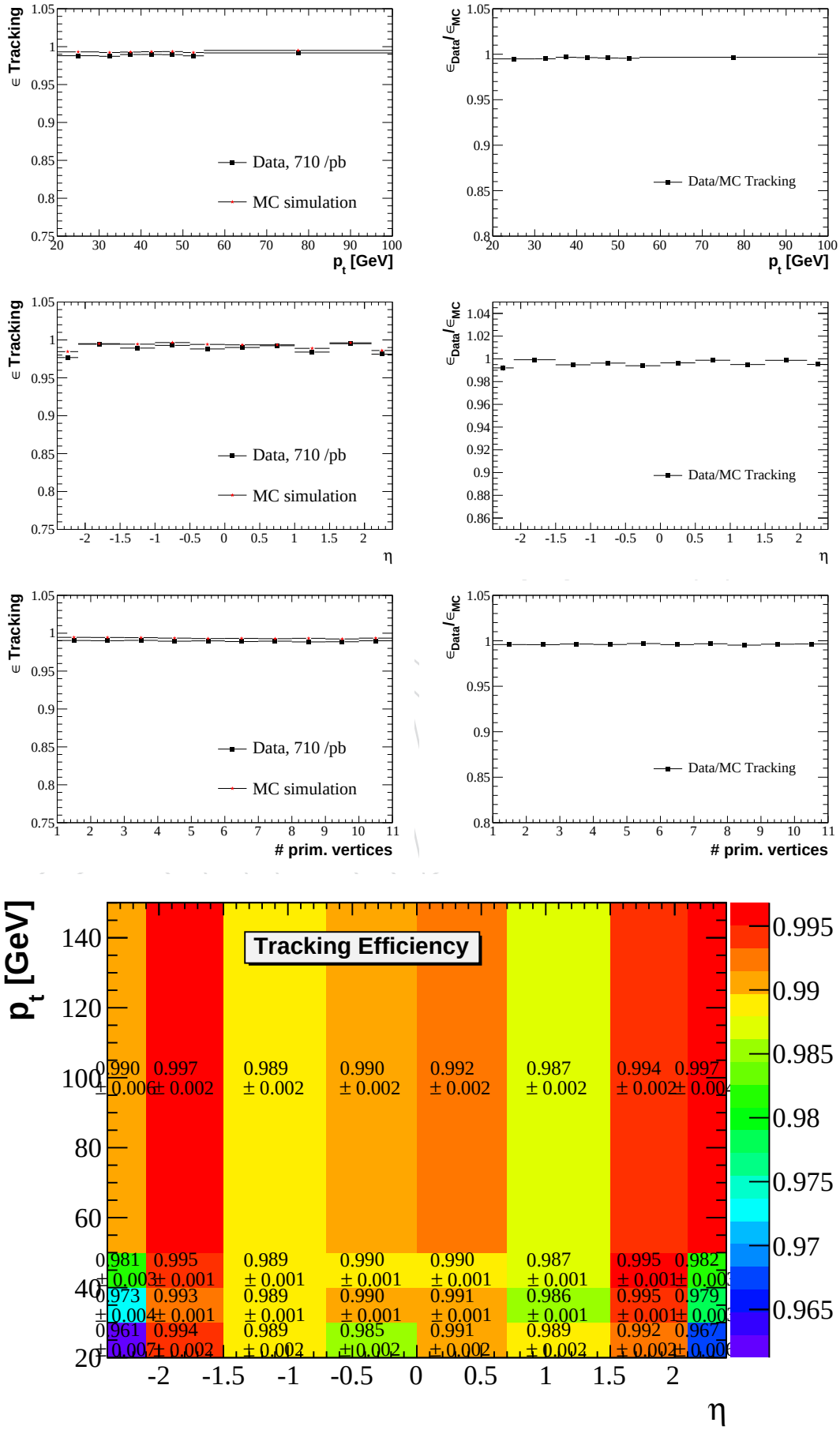

Figure 7: Top: tracking efficiency depending on p_{T}, η, and number of primary vertices together with Data-Monte Carlo ratio. Bottom: $p_{\mathrm{T}} - \eta$ dependent efficiency.

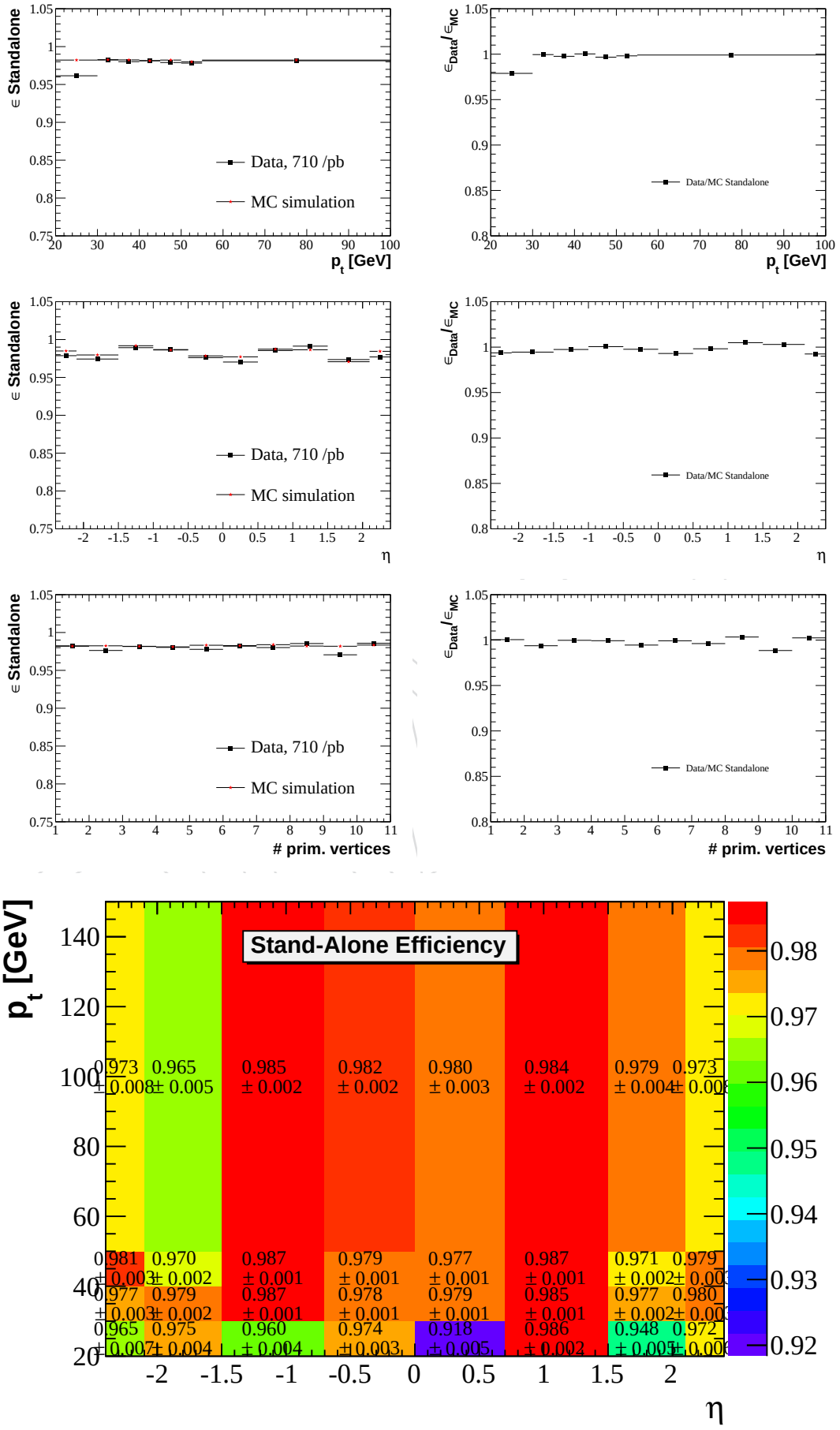

Figure 8: Top: stand-alone efficiency depending on p_{T}, η, and number of primary vertices together with Data-Monte Carlo ratio. Bottom: $p_{\mathrm{T}} - \eta$ dependent efficiency.

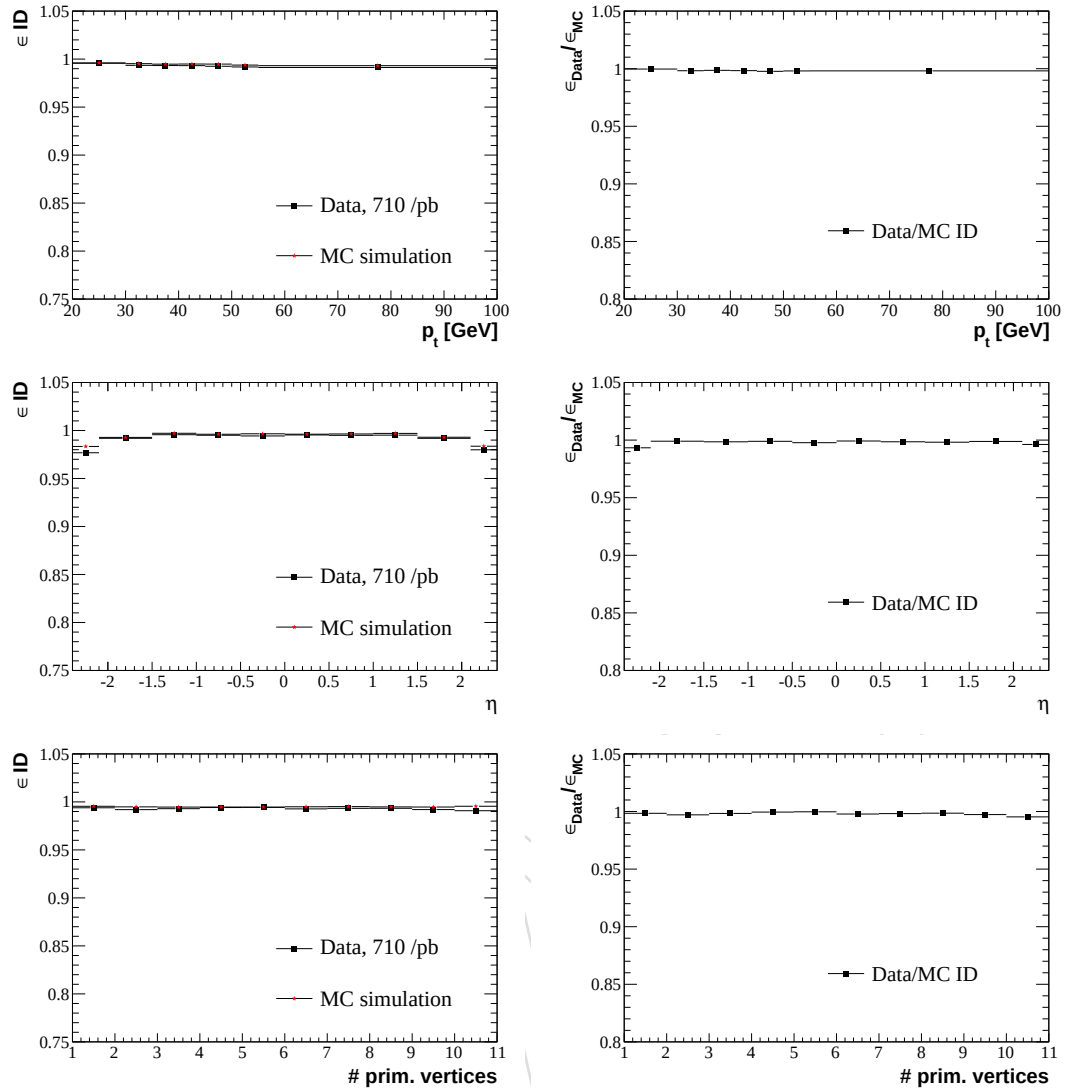

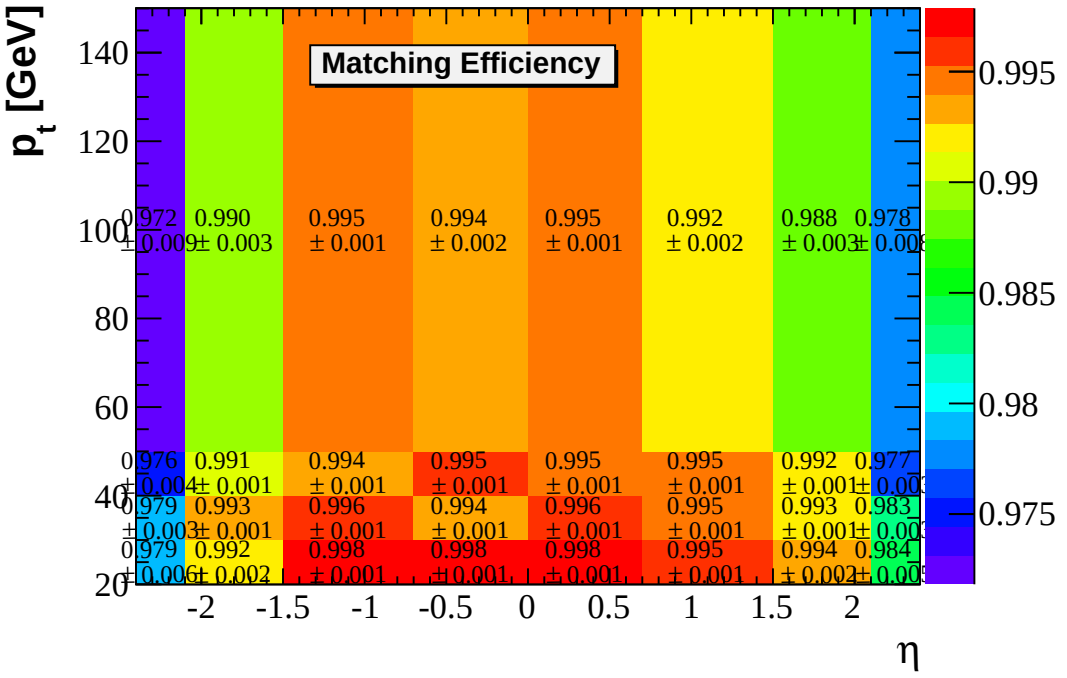

Figure 9: Top: matching efficiency depending on p_{T}, η, and number of primary vertices together with Data-Monte Carlo ratio. Bottom: $p_{\mathrm{T}} - \eta$ dependent efficiency.

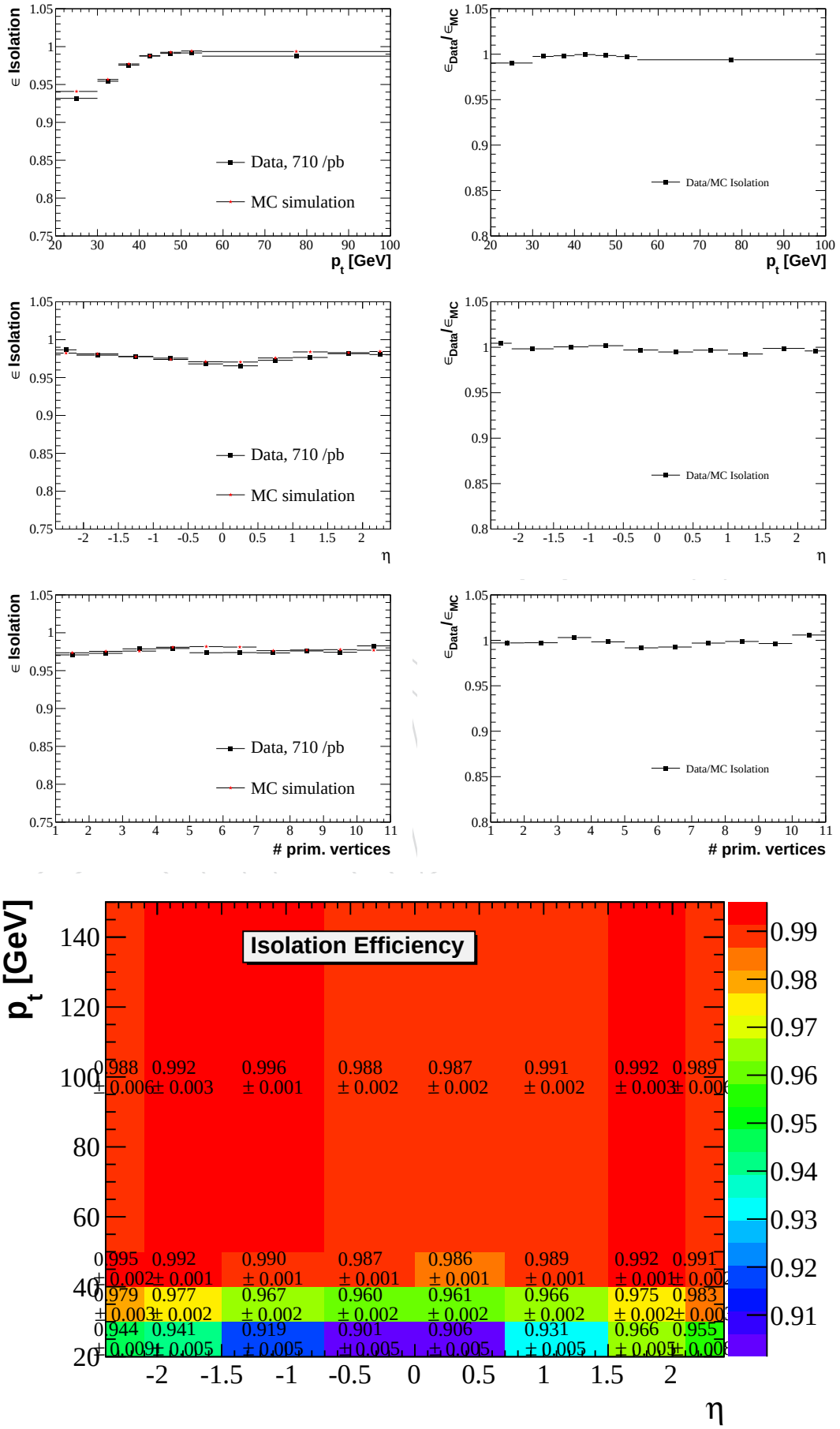

Figure 10: Top: isolation efficiency depending on p_T, η, and number of primary vertices together with Data-Monte Carlo ratio. Bottom: $p_T - \eta$ dependent efficiency.

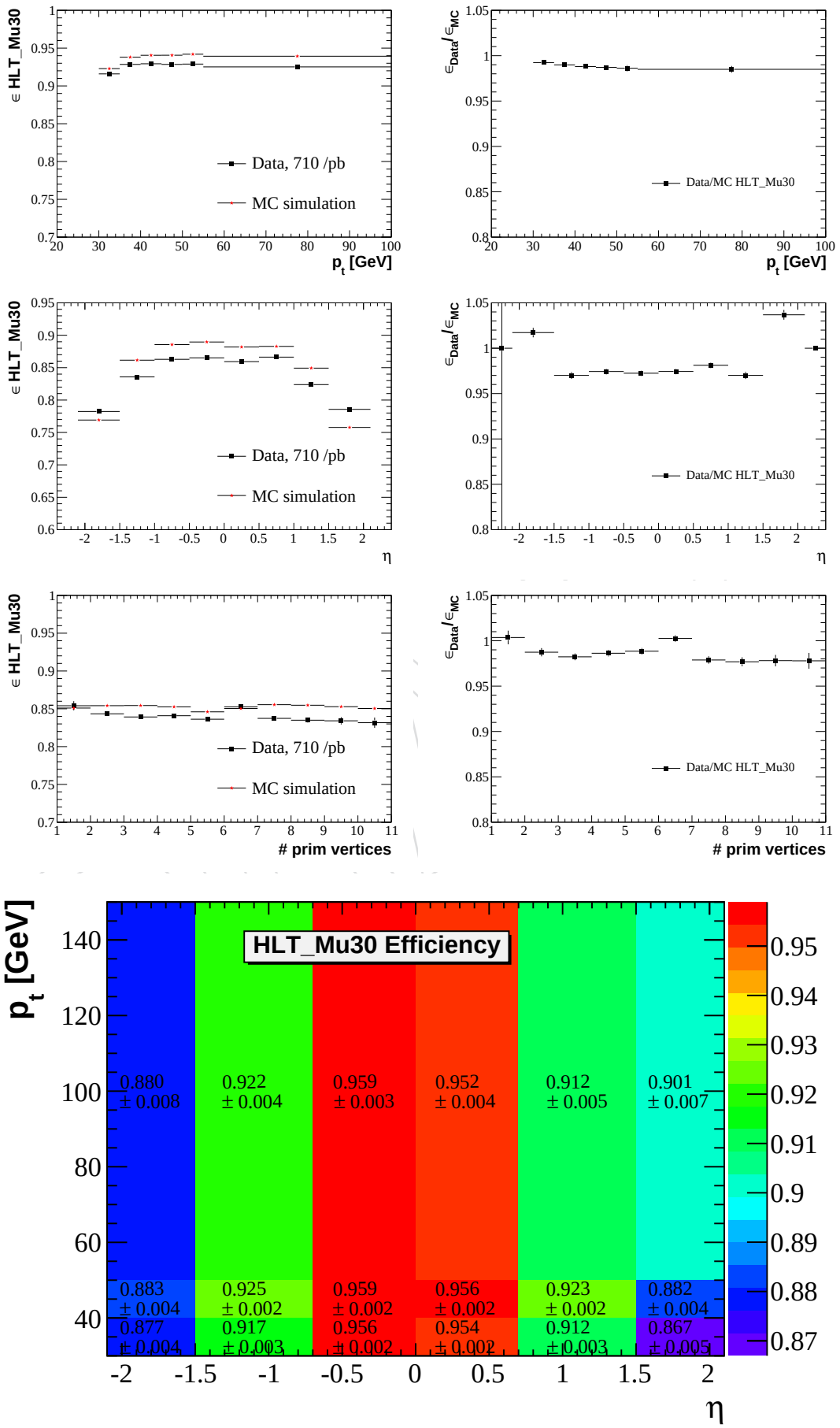

Figure 11: Top: trigger efficiency depending on p_T, η, and number of primary vertices together with Data-Monte Carlo ratio. Bottom: $p_T - \eta$ dependent efficiency.

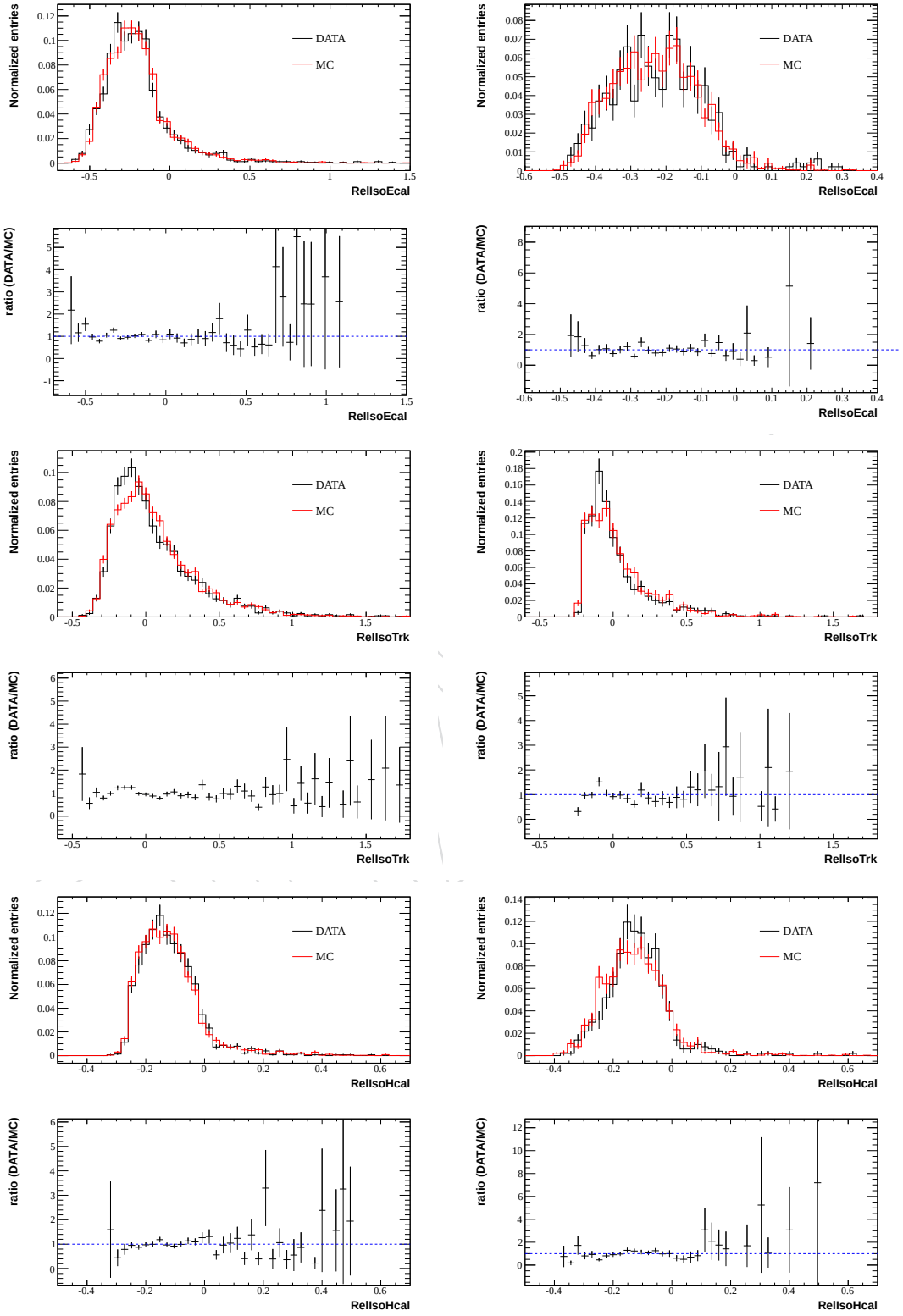

Figure 12: Pileup corrected photon isolation variables for barrel (left) and endcap (right).

We cross-check that the photons are simulated well in Monte Carlo by comparing the performance of the full photon selection criteria without pixel veto requirements on electrons from Z boson decay.

We use the official "Tag and Probe" tool to perform this comparison Both tag and probe electrons must have hadronic over electromagnetic fraction less then 0.5, $E_T > 20$ GeV, positioned in the ECAL fiducial region and be spatially separated by $\Delta R > 0.4$ from jets that are identified by the anti-k_T algorithm with $\Delta R = 0.5$ and meet the following selection criteria:

- $p_T^{jet} > 10$ GeV,
- $|\eta_{\text{jet}}| < 3.0$,
- electromagnetic energy fraction between 1 and 90%,
- $n90 > 5$.

We plot the di-electron invariant mass and obtain the number of signal events from fit. The signal shape is taken from POWHEG at the generator level, and is convolved with a resolution function with floating mean and width. Background is described by exponential function.

Di-electron mass distributions for electrons in data and MC are given in Fig. 14

The selection criteria agrees well between that obtained in electron data and simulation samples. The efficiencies and their ratios from tag and probe and mc truth are shown in Fig. 14 as well as a ratio of *"isTight"* efficiencies measured for electrons and photons in the EB and EE sections of the ECAL are given in Fig. **??**.

As the Monte Carlo simulation describes data well, and results agree within 1% uncertainties from each other, we rely fully on Monte Carlo simulation to extract photon identification efficiency and we take a conservative systematic uncertainty of 2% due to potential discrepancy in modeling of the photon selection efficiency as function of photon E_T. **One needs to move efficiencies and scale factors from FSR photons here and somehow integrate with results from Zee**

3.5 MET reconstruction

4 Measurement of Wγ production cross section

In this section we document the measurement of the production cross section for $W\gamma \to \ell\nu\gamma$, where $\ell = e,\ \mu$. As the cross section diverges at LO for soft photons or those that are spatially close to charged lepton, we restrict our measurement to the following kinematic range:

- The transverse photon energy must be larger than 15 GeV.
- The lepton and the photon must spatially separated by $\Delta R(\ell, \gamma) > 0.7$.

4.1 Selection of $W\gamma \to \ell\nu\gamma$ final state

The $W\gamma \to \ell\nu\gamma$ final state is characterized by a prompt, energetic, and isolated lepton, significant missing energy due to a neutrino, and a prompt isolated photon. The basic requirements are similar for the electron and muon channels. We describe them together and point out the differences when present.

Events are selected with either single electron or single muon triggers for the electron or muon channels, respectively. In both cases, we use the unprescaled triggers with the lowest lepton p_T threshold available for a given run range, as given in Tables 8 and 4. We then require a charged

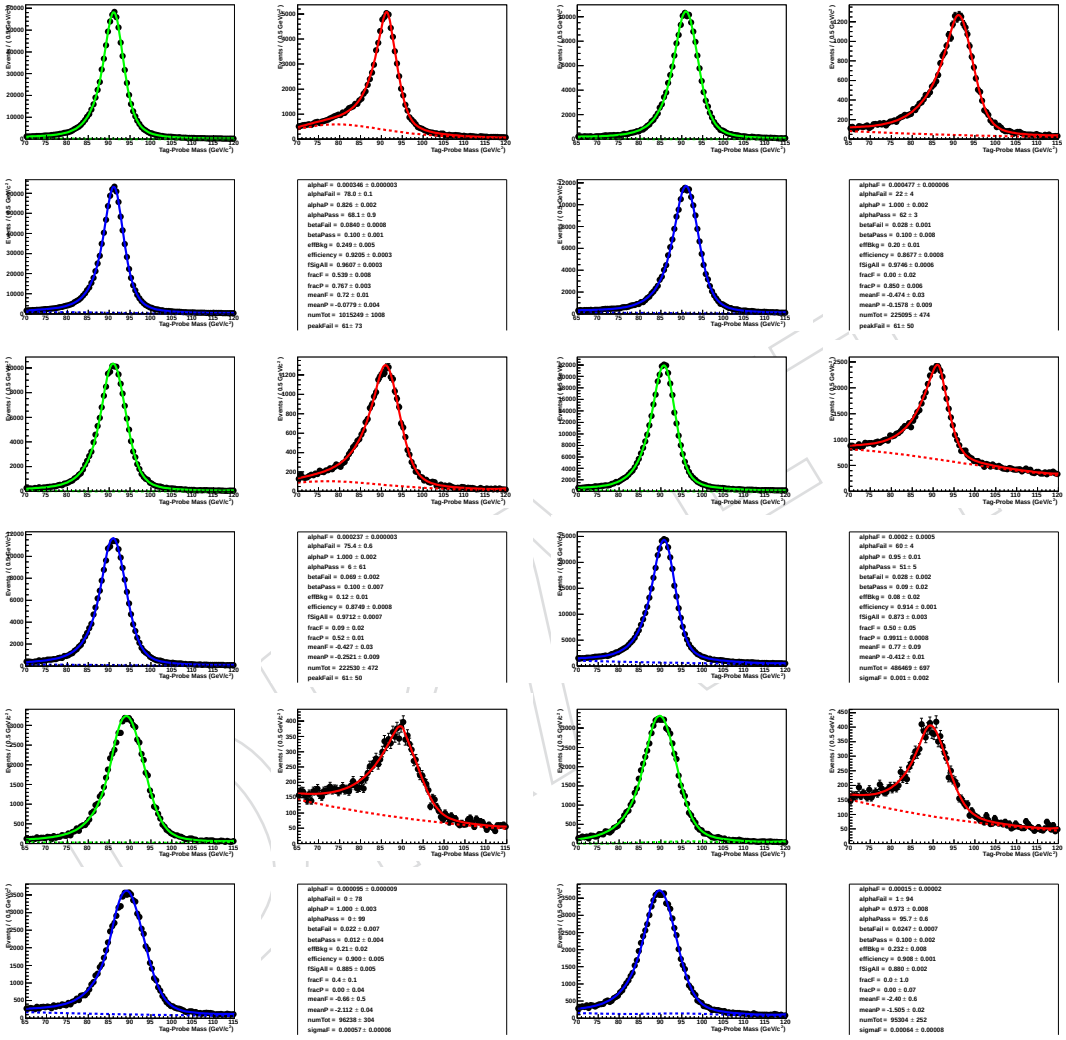

Figure 13: Fits to di-electron mass distribution in mc EB, EE-, EE+ and data EB, EE-, EE+

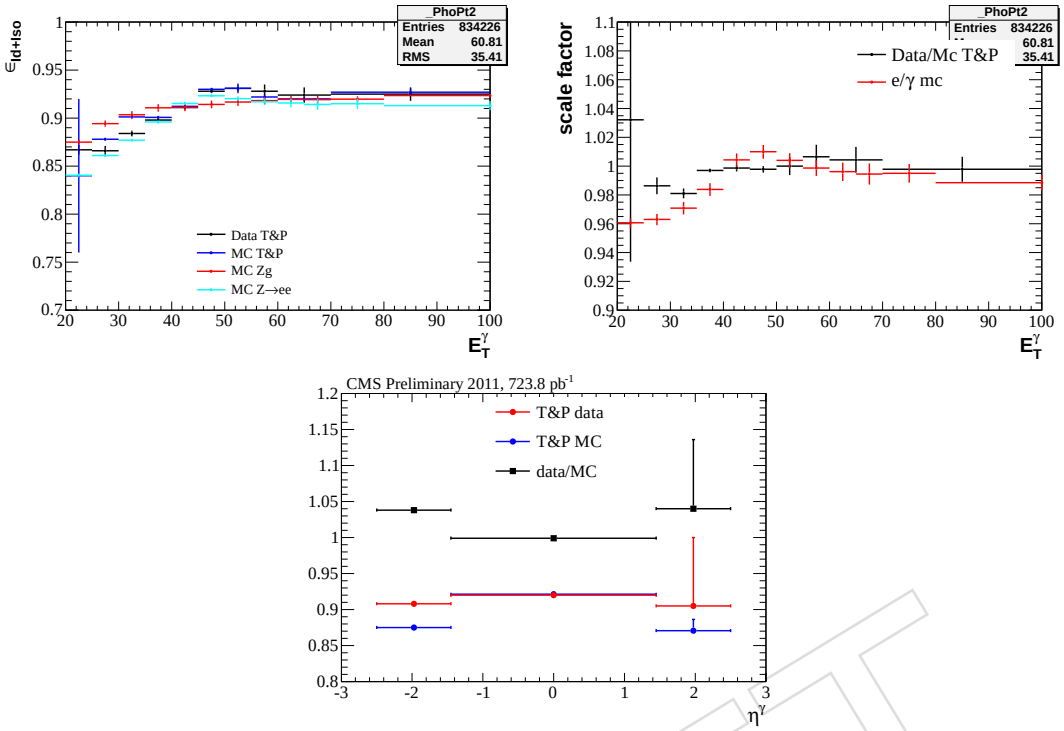

Figure 14: Efficiencies and their ratios from tag and probe method and mc truth

lepton, electron or muon, with $p_T > 35$ GeV, which has to be matched to the trigger object firing the HLT.

For the electron channel, we require one electron within the ECAL fiducial region to satisfy the WP80 set of identification and isolation criteria, described in Section 3.2. In addition, we remove the events having two or more electrons which satisfy the WP95 set of identification and isolation criteria, with $p_T > 20$ GeV. This veto criterion is used to reduce a large fraction of Drell-Yan background.

For the muon channel, we select events by requiring at least one muon with $p_T > 35$ GeV that satisfies selection criteria outlined in Section 3.3. We reject events that have more than one muon candidates if the next-to-leading muon has $p_T > 10$ GeV to reduce Drell-Yan background.

The missing transverse energy in the event is computed using the Particle Flow algorithm (pfMET). pfMET is required to be larger than 25 GeV. This requirement suppresses the backgrounds from Z/γ^*+jets, multijet QCD backgrounds, and γ+jets processes. The threshold value has been optimized to achieve the best significance defined as $S/\sqrt{B}$, where S is the number of signal events, and B is the estimated background.

Finally, we require the presence of a photon candidate with $E_T > 15$ GeV within the ECAL fiducial region. The photon candidate is required to pass the *isTight* photon selection described in Section **??**.

After the full selection, 2845 events are selected in the $e\nu\gamma$ channel in the data with 723.9 pb^{-1} of integrated luminosity and 3228 events are selected in the $\mu\nu\gamma$ channel in the data with 711 pb^{-1} of integrated luminosity. Expected yields for the signal and background processes from Monte Carlo simulation are given in Table 16 for the $e\nu\gamma$ channel and Table 17 for the $\mu\nu\gamma$

channel. A comparison of several kinematic distributions between data and Monte Carlo after the full event selection is shown in Fig. 15 for the muon channel and in Fig. 16 for the electron channel.

4.2 Background determination

The largest background to $W\gamma$ events comes from events in which the photon is a faked by a jet that has a large fraction of electromagnetic energy. The following background processes fall into this category:

- W+jets where the jet fakes a photon.
- Z+jets where one of the leptons from the Z boson decay is lost and a jet is misidentified as a photon.
- $t\bar{t}$+jets where one of the W bosons from the $t\bar{t}$-pair decays into a lepton and a jet is misidentified as a photon.

The fake photon background is estimated with the ratio and template methods described in Section **??** for both final states, $e\nu\gamma$ and $\mu\nu\gamma$.

For electron channel, the second major background to $W\gamma$ events comes from events in which electrons misidentified as photon in Drell-Yan or multiboson events. This background is estimated by the invariant mass of electron and photon. For muon channel, this background is small and is estimaed by using MC.

Further backgrounds may come from:

- Misidentified leptons from QCD γ+jet events which is negligible according to studies based on Monte Carlo simulation samples.
- $W\gamma \to \tau\nu\gamma$ where the τ decays to $\ell\nu\gamma$.
- $Z\gamma$ events.

The estimation of all these background sources is described in the following subsections.

4.2.1 Estimated background from a jet faking a photon in $W\gamma \to \mu\nu\gamma$.

The results of background estimation using the template and ratio method for the $\mu\nu\gamma$ final state are shown in Fig. 17. The estimated background is 1585.7 $\pm$ 36.3 (stat.) $\pm$ - (syst.) events using the template method. The estimated background yields for the template and ratio methods are given in Table 18.

4.2.2 Estimated background from a jet faking a photon in $W\gamma \to e\nu\gamma$.

For the $e\nu\gamma$ channel, the results from template and ratio background estimation is shown in Fig. 18. The estimated background is 1139.3 $\pm$ 27.2 (stat.) $\pm$ - (syst.) events by the template method and - $\pm$ - (stat.) $\pm$ - (syst.) events by the ratio method. The fitted template shapes for each E_T^γ bin are shown in Fig. 19 for photon candidates in the barrel and in Fig. 20 for those in the endcaps. The estimated background yields are listed in Table 19. The statistical errors of the template method come from the extended-ML fit. The systematic errors are described in Section **??**.

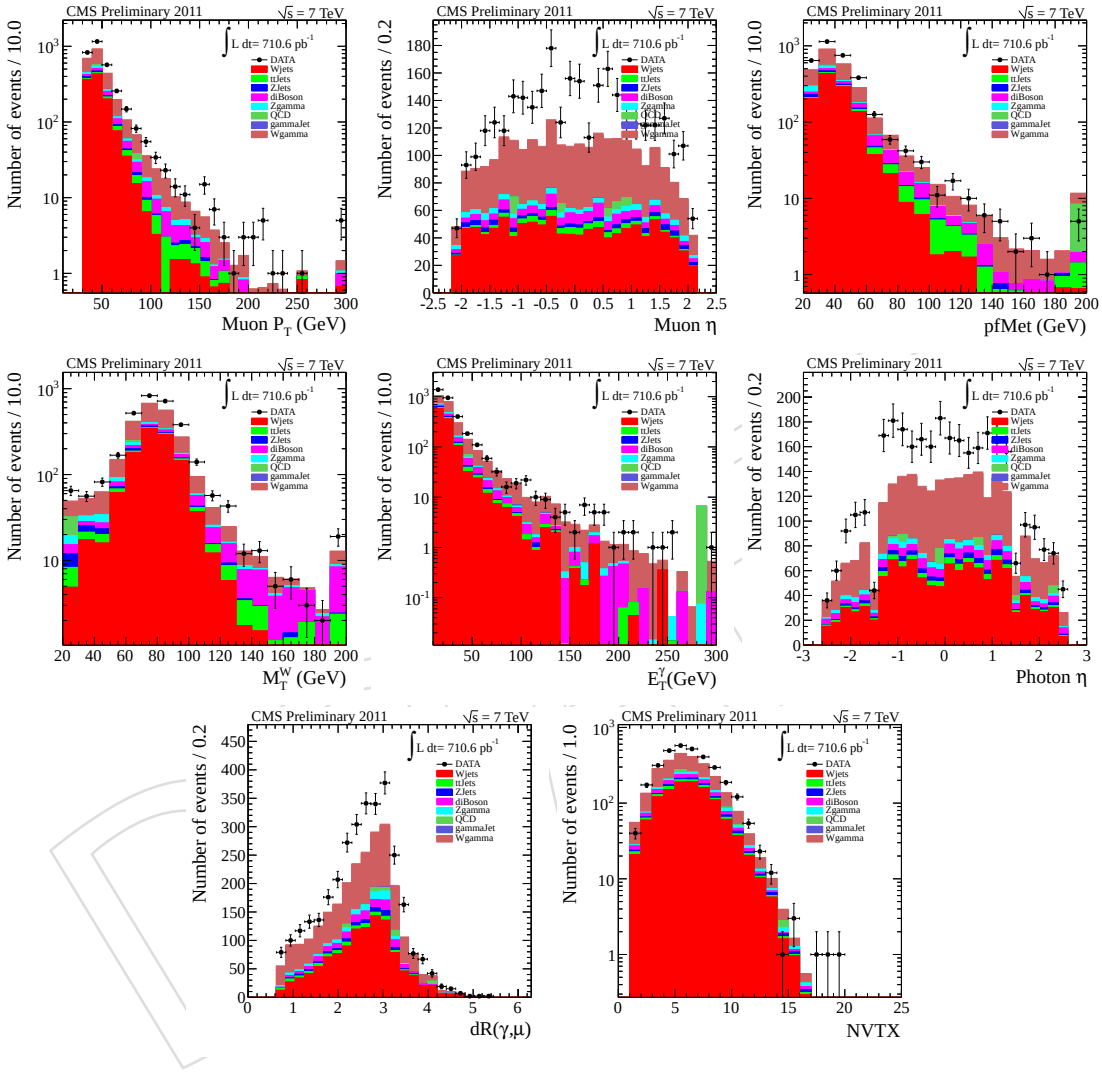

Figure 15: Muon candidate p_T , pseudorapidity, missing transverse energy, invariant transverse mass, photon candidate E_T, pseudorapidity, $\Delta R(\mu, \gamma)$, and number of good vertices overlaid distributions of the $W\gamma$ candidates in data, signal MC, and background MC for $W\gamma \to \mu\nu\gamma$.

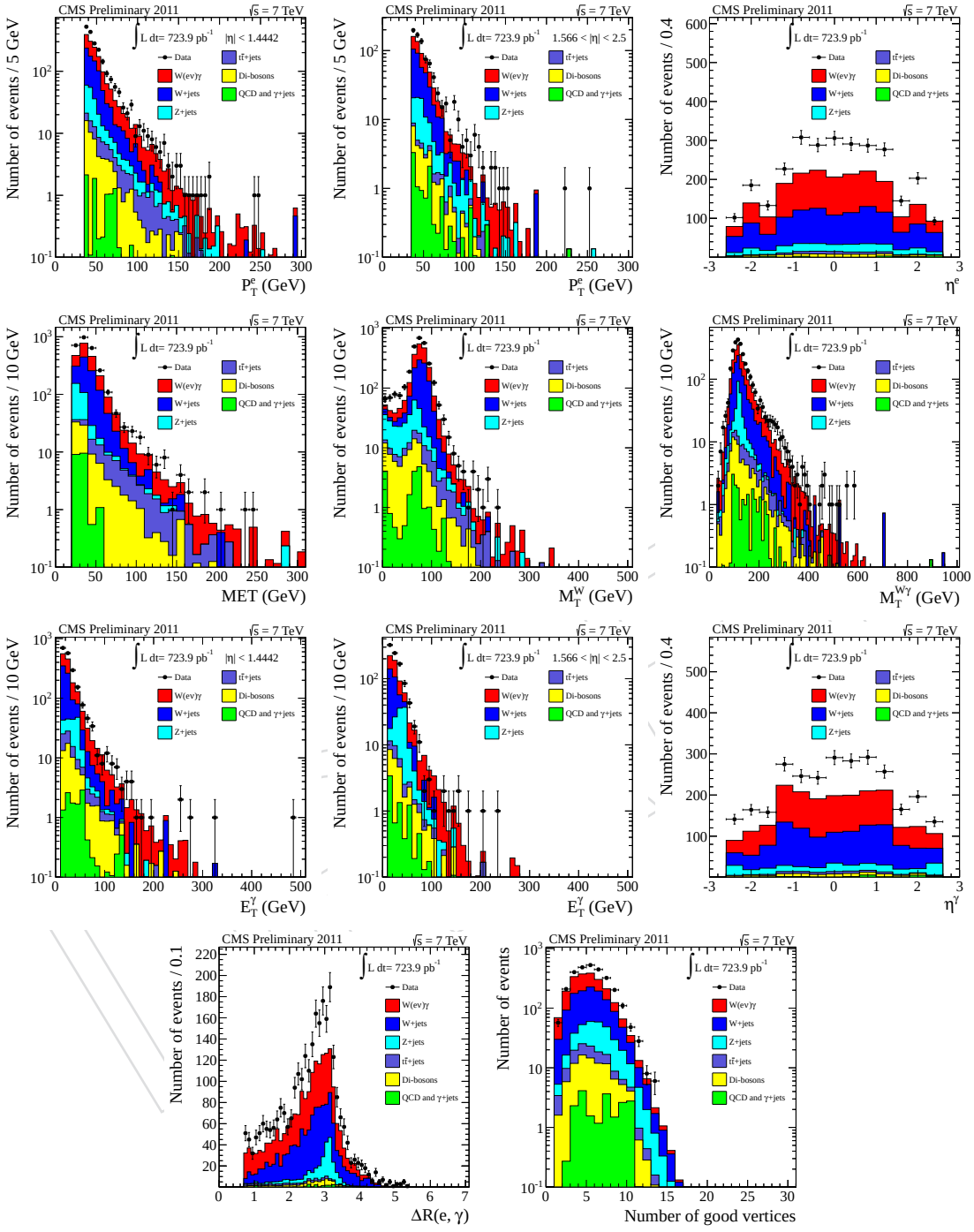

Figure 16: Electron candidate E_T in EB ECAL, that in EE ECAL, pseudorapidity, missing transverse energy, invariant transverse mass, cluster transverse mass, photon candidate E_T in EB ECAL, that in EE ECAL, pseudorapidity, $\Delta R(e,\gamma)$, and number of good vertices overlaid distributions of the $W\gamma$ candidates in data, signal MC, and background MC for $W\gamma \to e\nu\gamma$.

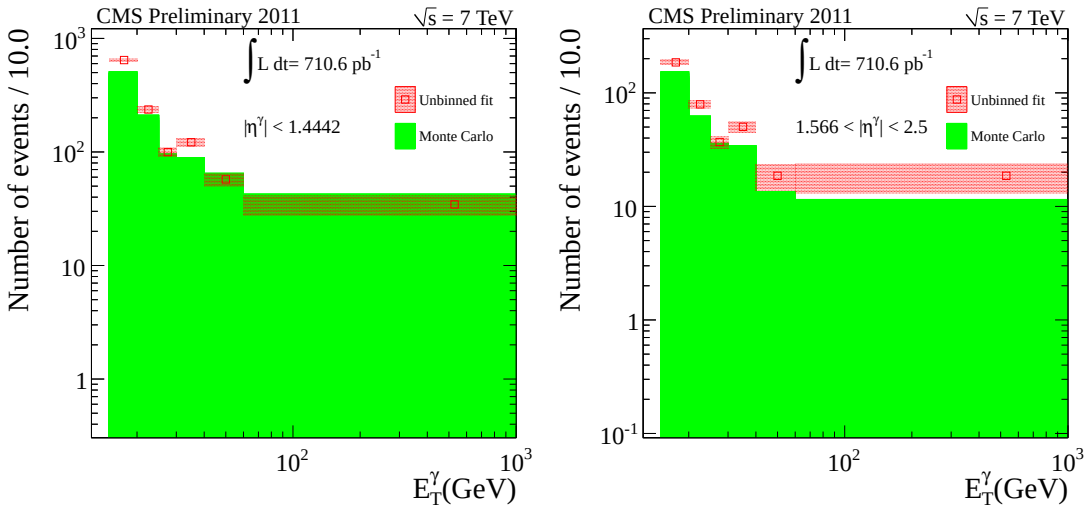

Figure 17: $W\gamma \rightarrow \mu\nu\gamma$ estimated background for the barrel (left) and endcap (right) photon candidates, using template (red solid square dots) method. The errors are from the statistical uncertainty only. The MC background estimation is shown as filled histograms.

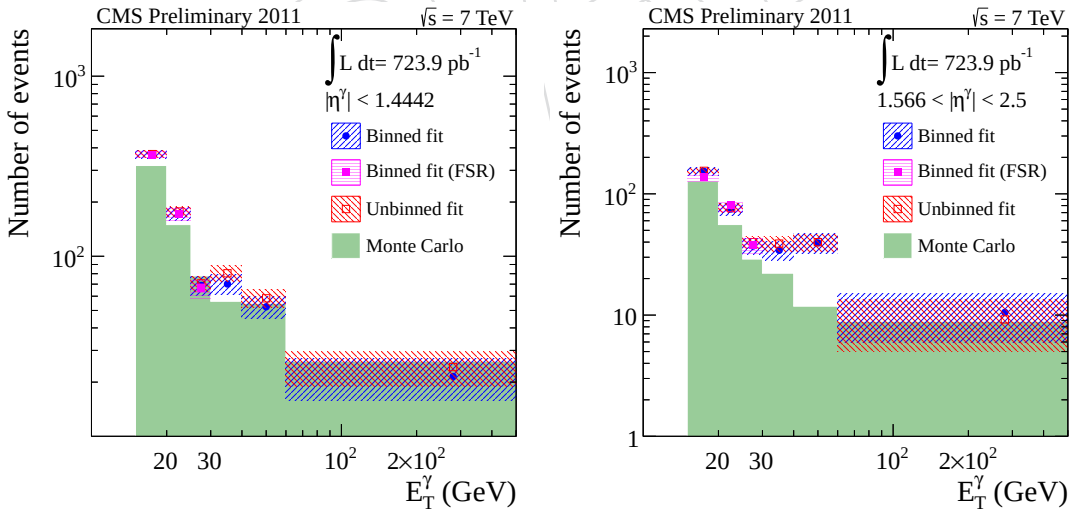

Figure 18: $W\gamma \rightarrow e\nu\gamma$ estimated background for the barrel (left) and endcap (right) photon candidates, using template (red solid square dots) and ratio (blue hollow square dots) methods. The errors are from the statistical uncertainty only. The MC background estimation is shown as filled histograms.

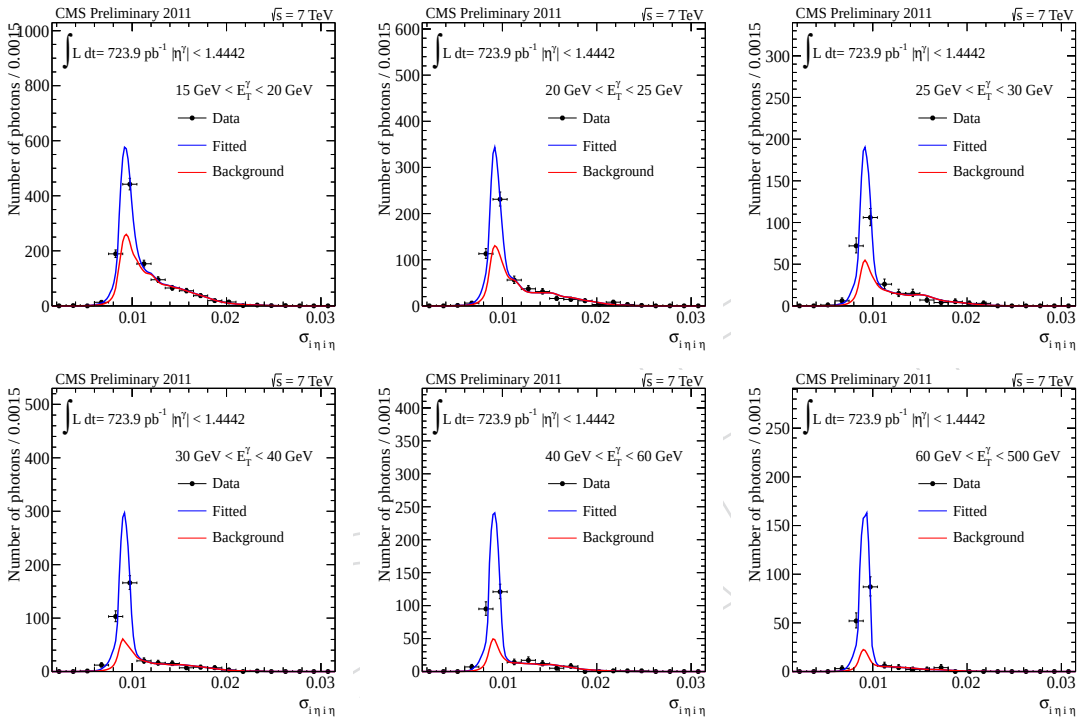

Figure 19: The $\sigma_{i\eta i\eta}$ distributions for the selected $W\gamma \rightarrow e\nu\gamma$ events with photon candidates identified in the barrel with the E_T of 15-20 GeV (top left), 20-25 GeV (top middle), 25-30 GeV (top right), 30-40 GeV (bottom left), 40-60 GeV (bottom middle), and 60-500 GeV (bottom right) in data (black squares). The unbinned fit result is shown by the blue solid line, and the background component is shown in red.

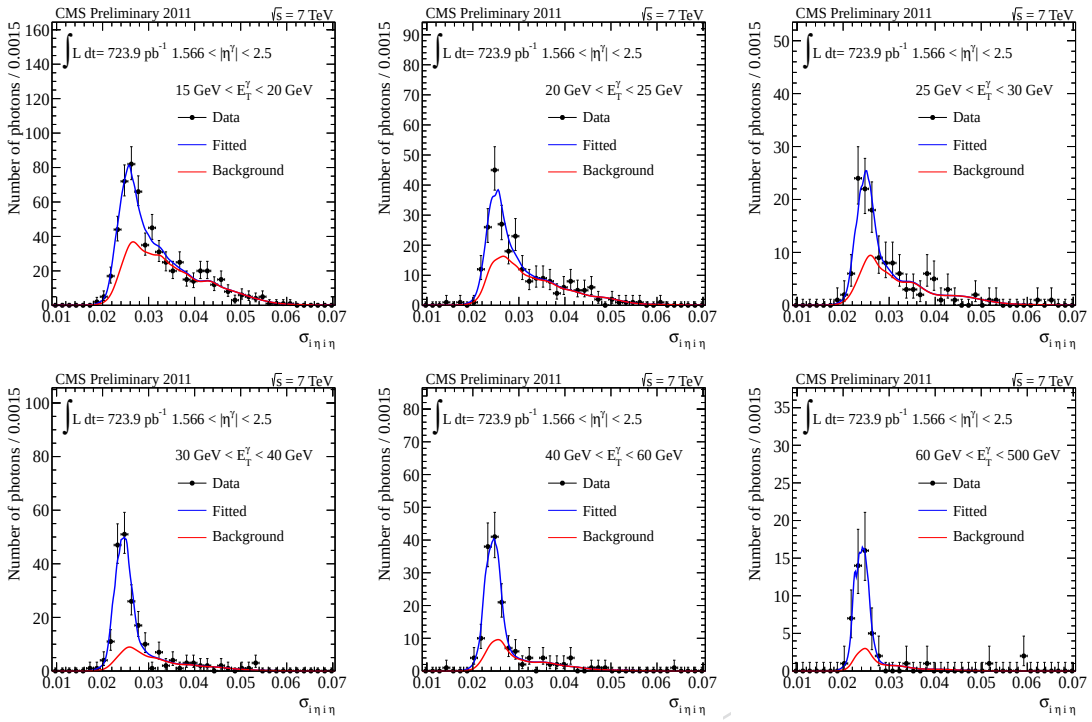

Figure 20: The same as in Fig. 19 but for the photon candidates reconstructed in the endcaps.

4.2.3 Estimation of background due to electrons misidentified as photons in $W\gamma \to \ell\nu\gamma$

Among background contributions from processes without genuine photons, Drell-Yan, and multiboson production contaminate the signal when an electron is misidentified as a photon. This background is caused by the inefficiency of GsfElectron reconstruction, and by the inefficiency of the pixel seed veto in discriminating photons from electrons.

This contribution for $W\gamma \to e\nu\gamma$ is estimated using data-driven method. For $Z + X$ process, if an electron passes electron selection and the other electron is misidentified as a photon, the invariant mass of electron and photon will have a resonance at Z mass. The number of $Z + X$ events is determined from the invariant mass of electron and photon distribution fit to the convolution of a Breit-Wigner and a Crystal Ball function for signal and an exponential function for modeling the background. The distribution of $M_{e,\gamma}$ and fitting results are shown in Fig. 21.

Besides $Z + X$ process, electron misidentification can also come from W+jets, $t\bar{t}$+jets, and WW. This contribution is estimated using MADGRAPH W+jets, $t\bar{t}$+jets, and WW samples, where we require photon candidates to be spatially matched to generator-level electrons. We estimated the yield to be 449.0 $\pm$ 47.4 (stat.) $\pm$ - (syst.) events after the full event selection for the $e\nu\gamma$ final state. The uncertainty includes the statistical uncertainty of the simulated sample as well as the systematic uncertainties on the electron and photon energy scales.

4.2.4 Estimation of $W\gamma \to \tau\nu\gamma$ background in $W\gamma \to \ell\nu\gamma$

A small fraction of $W(e\nu)\gamma$ candidates come from $W\gamma \to \tau\nu\gamma$ events. This background is estimated using Monte Carlo. The MADGRAPH generator used to generate the $W\gamma \to e\nu\gamma$ and $W\gamma \to \mu\nu\gamma$ Monte Carlo is also used to generate the $W\gamma \to \tau\nu\gamma$ Monte Carlo. The estimated

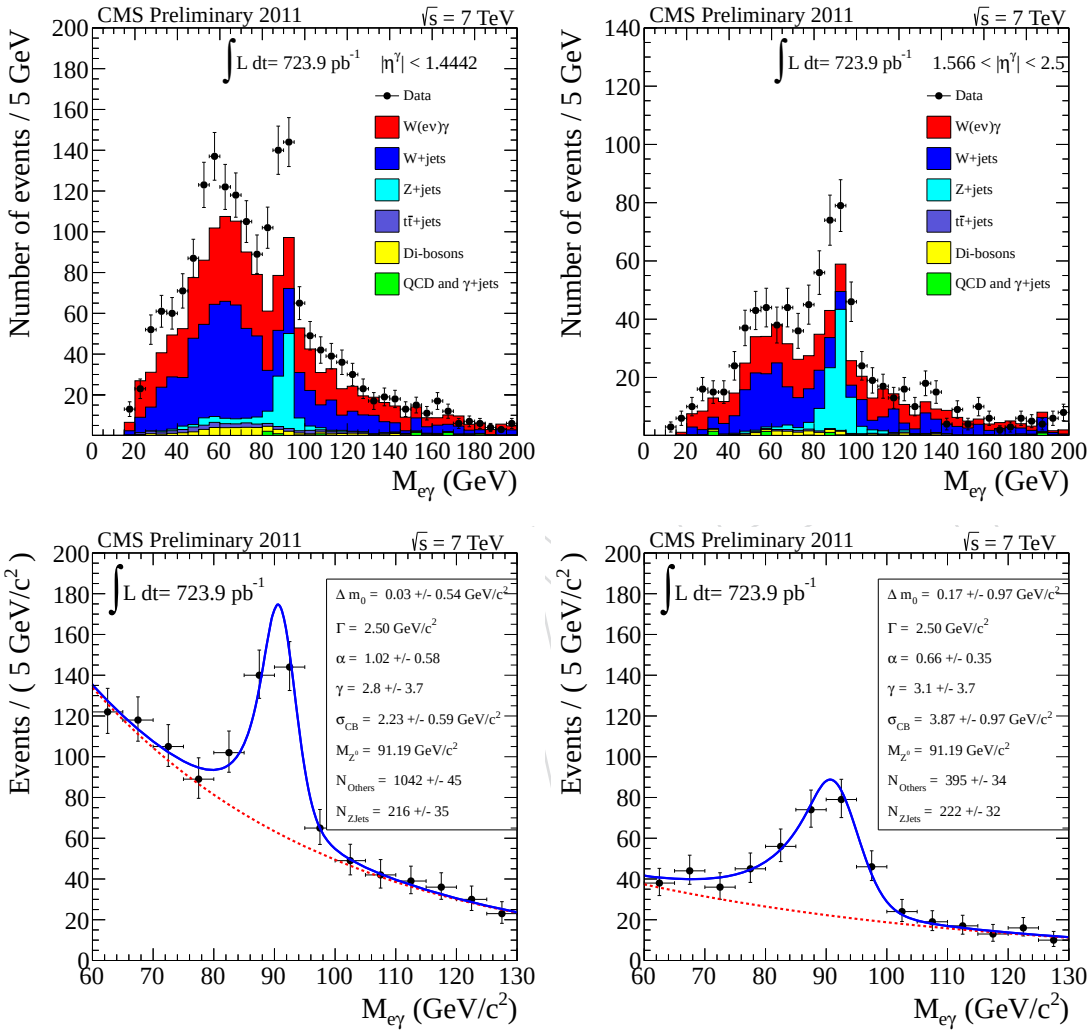

Figure 21: The distributions of $M_{e,\gamma}$ for photon in barrel (top left) and in endcap (top right). The fitting result for photon in barrel (bottom left) and in endcap (bottom right).

number of selected $W\gamma \to \tau(\to e\nu_e\nu_\tau)\nu\gamma$ events is 26.2 $\pm$ 1.1 (stat.) $\pm$ - (syst.). The fraction

$$f_{\tau\to e} \equiv \frac{\sigma_{W(\tau\nu)\gamma} \times \varepsilon_{W(\tau\nu)\gamma}}{\sigma_{W(e\nu)\gamma} \times \varepsilon_{W(e\nu)\gamma}}, \tag{3}$$

is estimated to be $f_{\tau\to e}$ = 0.03 $\pm$ 0.001 (stat.) $\pm$ - (syst.). The uncertainty includes the statistical uncertainty of the simulation sample as well as the systematic uncertainties of the electron and photon energy scales.

For the muon channel, the expected number of selected $W\gamma \to \tau(\to \mu\nu_\mu\nu_\tau)\nu_\tau\gamma$ events is determined to be 28.9 $\pm$ - (stat.) $\pm$ - (syst.) using Monte Carlo samples (see Table 17).

4.2.5 Estimation of $Z\gamma \to \ell\ell\gamma$ background in $W\gamma \to \ell\nu\gamma$

The contribution from $Z\gamma \to ee\gamma$ events is suppressed by the second electron veto, and by the $\not{E}_{\mathrm{T}}$ requirement. The remaining background from electrons that fail reconstruction is estimated using Monte Carlo simulation samples. The number of selected $Z\gamma \to ee\gamma$ in the $e\nu\gamma$ final state is estimated to be 32.8 $\pm$ 1.2 (stat.) $\pm$ - (syst.). The fraction

$$f_{Z\gamma} \equiv \frac{\sigma_{Z(ee)\gamma} \times \varepsilon_{Z(ee)\gamma}}{\sigma_{W(e\nu)\gamma} \times \varepsilon_{W(e\nu)\gamma}}, \tag{4}$$

is estimated to be $f_{Z\gamma}$ = 0.037 $\pm$ 0.001 (stat.) $\pm$ - (syst.). The uncertainty includes statistical uncertainty of the simulation sample as well as systematic uncertainties on electron and photon energy scales.

For the muon channel, the number of $Z\gamma \to \mu\mu\gamma$ and $Z\gamma \to \tau\tau\gamma$ events passing the full $W(\mu\nu)\gamma$ selection is estimated to be 94.5 $\pm$ - (stat.) $\pm$ - (syst.).

A study of the differences between the $Z\gamma$ background yields in the electron and muon channels can be found in Appendix **??**.

4.2.6 Summary of background estimation to $W\gamma \to \ell\nu\gamma$ processes

The expected background contributions from all considered sources for the $W\gamma$ final states is summarized in Table 20. The ratio and template method results agree very well with each other. Because the systematic uncertainties on the ratio method are smaller than those on the template method (see section **??**), we chose the ratio method result for the cross section determination.

4.3 Measurement of the $W\gamma$ cross section

4.3.1 Procedure for the cross-section determination

The measurement of cross sections is based on the formula:

$$\sigma = \frac{N_{sig}}{A \cdot \epsilon \cdot \mathcal{L}} \tag{5}$$

where N_{sig} is the number of observed signal events, A is the fiducial and kinematic acceptance, ϵ is the selection efficiency for events in the acceptance, and $\mathcal{L}$ is the integrated luminosity. The value of A is affected by the PDF and other theoretical uncertainties, while the value of ϵ is susceptible to errors from triggering and reconstruction. In order to control the efficiency uncertainties, we concentrate on the extraction of corrections to the efficiencies obtained from the simulation. These correction factors come from efficiency ratios $\rho = \epsilon/\epsilon_{\mathrm{sim}}$ derived by measuring ϵ and ϵ_{sim} in the same way on data and simulation, respectively. We then replace

the product $A \times \epsilon$ by the product $\mathcal{F} \times \rho$, where $\mathcal{F} \equiv A \times \epsilon_{\text{sim}}$ is the fraction of generated events selected in the simulation. Furthermore, the number of signal events N_{sig} is not measured directly but is obtained by subtracting the estimated number of background events N_{backg} from the observed number of selected events N_{obs}.

Equation (5) can therefore be rewritten as

$$\sigma = \frac{N_{obs} - N_{backg}}{\mathcal{F} \cdot \rho \cdot \mathcal{L}}. \tag{6}$$

We calculate $\mathcal{F} \equiv A \cdot \epsilon_{MC,W\gamma\to\ell\nu\gamma}$ using MC simulation, as $\mathcal{F}$ is defined as $N_{accept}/N_{gen,\,kin}$, where N_{accept} is the number of events passing all selection cuts, and $N_{gen,\,kin}$ is the number of generated events with $E_T^{\gamma} > 15$, $\Delta R_{\ell,\gamma} > 0.7$.

In the next subsections, we first list the systematic uncertainties affecting the measurement, and we then give the results for the measurement of the $W\gamma$ cross section for both the electron and muon channels.

4.3.2 Systematic uncertainties

We divide systematic uncertainties into 3 groups: those affecting $\mathcal{F}$, those affecting the efficiency ratios, ρ, and those affecting the background estimation.

The following systematic uncertainties affect $\mathcal{F} \equiv A \cdot \epsilon_{MC,W\gamma\to\ell\nu\gamma}$:

- Uncertainties in the electron and photon energy scales. The uncertainty on $\mathcal{F}$ is estimated by varying the electron and photon energy scales. Uncertainties in the electron energy scale and resolution only affect the electron channel.
- $\mathcal{F}$ varies by less than 1% by applying an additional smearing of the electron and photon energies.
- Uncertainties due to pileup. To account for this, we recalculate $\mathcal{F}$ using the MC signal samples which include simulated pileup.
- Uncertainties of the PDF.

The overall uncertainties on $\mathcal{F}$ are -% for the electron channel and -% for the muon channel.

The correction factor (ρ_{eff}) takes into account the difference of efficiency between data and simulation. The ρ_{eff} includes the lepton trigger, and the lepton and photon reconstruction and identification, *eg.*, $\rho_{Trg80} \cdot \rho_{Reco} \cdot \rho_{WP80} \cdot \rho_{\gamma} \cdot \rho_{MET}$. The latter is the corresponding ratio for $\not\!\!E_{\text{T}}$ as evaluated in Section **??**. The overall uncertainty on the correction factor (ρ_{eff}) is -% for $e\nu\gamma$ and -% for $\mu\nu\gamma$.

The uncertainties from the background estimation (ratio method) are -% for the barrel and -% for the endcap. The overall uncertainty on background estimation is -% for $e\nu\gamma$ and -% for $\mu\nu\gamma$.

Finally, an uncertainty coming from the measurement of the integrated luminosity, amounting to -%, is also taken into account.

A summary of all of the systematic uncertainties is given in Table 21 for both the electron and muon channels. The main source of uncertainty in both cases, apart from the uncertainty on luminosity, is due to the data-driven background estimation from the ratio method. A detailed description of the estimation of this uncertainty can be found in Section **??**.

More detailed information can be found in Section **??**.

4.3.3 Results for the Electron channel

The cross-section is calculated using the expression in Equation (6).

There are 2845 $W\gamma \rightarrow e\nu\gamma$ candidates after full event selection in data with 723.9 pb^{-1} of integrated luminosity. The estimated background of W+jets is 1139.3 $\pm$ 27.2 (stat.) $\pm$ - (syst.) events using the template method and - $\pm$ - (stat.) $\pm$ - (syst.) events using the ratio method. We use results of the ratio method because it gives the most accurate measurement. The estimated background of eeX is 449 $\pm$ 47.4 (stat.). The value of N_{sig} is obtained from the number of observed events and the estimated number of background events with the following equation:

$$N_{sig} = N_{obs} - N_{bkg}^{Wjet} - N_{bkg}^{eeX} - N_{bkg}^{W(\tau\nu)\gamma} - N_{bkg}^{Z\gamma}, \tag{7}$$

where N_{obs} is the number of observed events, N_{bkg}^{Wjet} is the estimated number of background in which jets fake photons, N_{bkg}^{eeX} is the estimated number of background in which an electron is misidentified as a photon, $N_{bkg}^{W(\tau\nu)\gamma}$ is the estimated number of background due to the $W(\tau\nu)\gamma$ process, and $N_{bkg}^{Z\gamma}$ is the estimated number of background due to the $Z\gamma$ process,

The numbers that are used to calculate the cross section are summarized in Table 25.

Finally, the estimated cross section is:

$$\sigma(pp \rightarrow W\gamma \rightarrow e\nu\gamma) = 45.4 \pm 2.9 \text{ (stat.)} \pm - \text{ (syst.)} \pm 2.7 \text{ (lumi.) pb.}$$

This is consistent with the theoretical NLO cross section 31.47 $\pm$ 0.1 pb.

4.3.4 Results for the Muon channel

We obtain 3228$\pm$57 events in data corresponding to 711 pb^{-1} of integrated luminosity after the full set of selection criteria. Referring to Eqn. (6), N_{sig} is obtained by subtracting the estimated backgrounds from the $W\gamma \rightarrow \mu\nu\gamma$ candidate yield. The estimated total backgrounds from all sources is given in Table 23. The full set of parameters used for the cross-section measurement is listed in Table 24 and the value for the cross-section for the process $pp \rightarrow W(\mu\nu_\mu)\gamma + pp \rightarrow W \rightarrow \mu\nu_\mu\gamma$ with p_T^γ >15 GeV/c and $\Delta R(\mu, \gamma) > 0.7$ is evaluated to be

$$\sigma(pp \rightarrow W\gamma \rightarrow \mu\nu\gamma) = 48.59 \pm - \text{ (stat.)} \pm - \text{ (syst.)} \pm - \text{ (lumi.) pb.}$$

The theoretical prediction is 31.47 $\pm$ − pb.

5 Measurement of Zγ production cross section

In this chapter we describe the measurement of the Zγ production cross section with Z boson decaying to either electrons or muons. In the following we collectively refer ISR $Z/\gamma^* \gamma \rightarrow \ell\ell\gamma$ and FSR $Z/\gamma^* \rightarrow \ell\ell\gamma$ processes to as a Zγ production.

Similarly to Wγ cross section measurement, it is impossible to measure the full Zγ cross section, so we restrict our measurement to the measurement of the Zγ production within the following kinematic requirements:

1. photon $E_{\text{T}} > 15$ GeV
2. the photon should be spatially separated from either of the leptons by $\Delta R(\ell, \gamma) > 0.7$

3. the dilepton invariant mass should be above 50 GeV.

This production is well-modeled [**?**] in a number of generators described in Section 2. Given an excellent agreement in modeling this process between samples, we choose to use the MADGRAPH generator, that models Zγ LO production with up to one jet. To simulate NLO effects, we scale the NLO cross section from MCFM.

Data samples for the Zγ study are described in Section 2. The corresponding integrated luminosity are 723.7 pb^{-1} for both $Z\gamma \to ee\gamma$ and $Z\gamma \to \mu\mu\gamma$ channels.

The main background to this process is the Z+jets with one of the jets in the final state misidentified as a photon candidate. We use template method described in Section **??** as it offers a more precise measurement of the background at lower photon E_T values. Other background sources coming from multijet QCD, diboson, and $t\bar{t}$ processes are estimated from MC simulation and found to be negligible.

5.1 Zγ event selection

Events for electron channel are selected using a set of di-electron High Level Triggers, described in Section 3.1.1. These events are further required to have at least two electron candidates with $p_T > 20$ GeV, within ECAL acceptance and passing the WP85 selection criteria described in Section 3.2 and at least one photon that satisfies photon selection desribed in Section **??**.

Similarly, events for $Z\gamma \to \mu\mu\gamma$ study are selected by one of the unprescaled dimuon triggers with the lowest-available p_T threshold, given in Section 3.1.2. These events are further required to have at least two muons with $p_T > 20$ GeV and passing selection criteria given in Section 3.3 and a photon passing selection criteria.

Applying the selection criteria yields 706 $Z\gamma \to ee\gamma$ candidate events. This is consistent with the MC prediction of 662.1 ± 4.7 events comprised of 537.9 ± 3.8 from signal and 121.0 ± 2.8 from background.

The $Z\gamma \to \mu\mu\gamma$ selection criteria yields 1108 candidate events. The observed number of events agrees well with 993.6 ± 35.9 of MC prediction with 776.5 ± 17.9 of expected $Z\gamma \to \mu\mu\gamma$ events and 217.1 ± 31.1 of background events.

The photon E_T, η, dielectron, and dielectron+photon invariant mass distributions for data and MC simulation, after applying full selection criteria, are shown in Fig. 22, and Fig. 23, and 24 for the $ee\gamma$ and $\mu\mu\gamma$ final states, respectively.

5.2 Determination of backgrounds

The dominant background to Zγ production is Z/γ^*+jets processes, where a jet is misidentified as a photon. For the cross section measurement we use the template method to estimate this background. The results from both methods are given in Table 26, The background distribution as function of photon E_T are shown in Fig. **??** with the systematic uncertainty calculated following the procedure described in Section **??**.

The other backgrounds from QCD multijet, photon+jets, $t\bar{t}$, and other di-boson processes are estimated from MC simulation to contribute $X \pm X$ and $X \pm X$ events for $ee\gamma$ and $\mu\mu\gamma$ channels, respectively, and therefore neglected in this analysis.

5.3 Systematic uncertainties

Systematic uncertainties in $Z\gamma$ production cross section measurement are described in Section **??**.

The sources of systematic uncertainties on signal estimation are summarized in Table 27 for both $Z\gamma \to ee\gamma$ and $Z\gamma \to \mu\mu\gamma$ channels. Uncertainty on the background estimation is dominated by the statistical sample of non-isolated photons used to derive the background using the ratio method. We treat this uncertainty as systematic and estimate it to be X% and X% for the $ee\gamma$ and $\mu\mu\gamma$ channels, respectively. The uncertainties on $\mathcal{F} = A \cdot \epsilon_{MC}$ are from energy scale and PDF. The systematic uncertainty on the efficiency is determined from the propagation of the statistical errors on the correction factor ρ_{eff}. The systematic uncertainty on the $\mathcal{F}$ is determined from the MC simulation. We vary the photon energy by X% in EB and X% in EE, and with X% additional energy resolution. Those values are discussed in Section **??**. For the electrons, the energy is varied by X% for EB and X% for EE, and smeared with an additional X% energy resolution. For uncertainties on pileup effect, we use MC singal sample with pileup scenario and recalculate $\mathcal{F}$. The deviation of $\mathcal{F}$ due to these variations is taken as the systematic uncertainty.

5.4 Measurement of the Zγ cross section

We calculate the cross section separately for $ee\gamma$ and $\mu\mu\gamma$ channels using the following formula:

$$\sigma_{Z\gamma\to ll\gamma} = \frac{N_{\text{observed}} - N_{\text{background}}}{A \cdot \epsilon_{MC,Z\gamma\to ll\gamma} \cdot \rho_{eff} \cdot \int \mathcal{L}\, dt'} \tag{8}$$

where N_{observed} is number of observed $Z\gamma$ candidates after the full selection, $N_{\text{background}}$ is the estimated number of background events, A is the signal acceptance, $\epsilon_{MC,Z\gamma\to ll\gamma}$ is the efficiency for all requirements of the event selection. The $A \cdot \epsilon$ is defined as $N_{\text{accept}}/N_{gen,\ kin}$, where the N_{accept} is the number of events passing all selection cuts, and the $N_{gen,\ kin}$ is the number of generated events with $E_T^{\gamma} > 15$ GeV, $\Delta R_{\ell,\gamma} > 0.7$ and $M_{\ell\ell} > 50$ GeV. for $Z\gamma \to ee\gamma$ and $Z\gamma \to \mu\mu\gamma$, respectively. The $\int L\, dt$ is the integrated luminosity, and ρ_{eff} is a correction factor that takes into account the data/simulation efficiency difference described in Section 3.

For $Z\gamma \to ee\gamma$, ρ_{eff} is calculated as a product of data/MC correction factors for electron and photon reconstrution and identification, *i.e.*, $\rho^2_{\text{reco}} \cdot \rho^2_{WP85} \cdot \rho_{\gamma}$. As electrons and photons reconstructed in barrel and endcap have different correction factors, we rely on signal simulation to estimate the average correction factor for the signal. We do not take into account data/MC correction due to trigger efficiency modeling, as the overall trigger efficiency for $ee\gamma$ channel is close to 100% and any modeling differences below 10% are negligible.

Similar to electron channel, ρ_{eff} in $Z\gamma \to \mu\mu\gamma$ is calculated as a product of data/MC correction factors for muon and photon reconstrution and identification.

The numbers that are used to calculate the cross sections are summarized in Table **??**. The estimated cross section of $Z\gamma \to \mu\mu\gamma$ is $6.30 \pm 0.39(\text{stat.}) \pm 0.81(\text{syst.}) \pm 0.38(\text{lumi.})$ pb. The estimated cross section of $Z\gamma \to ee\gamma$ is $5.57 \pm 0.35(\text{stat.}) \pm 0.30(\text{syst.}) \pm 0.34(\text{lumi.})$ pb.

Table 13: Summary of measured efficiencies in data, MC simulation compared to MC truth values.

Efficiency	Data	Simulation	MC truth information
ϵ_{TRK}	98.96 ± 0.02	99.34 ± 0.01	99.27 ± 0.01
ϵ_{SA}	97.80 ± 0.03	98.23 ± 0.02	98.24 ± 0.01
ϵ_{ID}	99.32 ± 0.02	99.49 ± 0.01	99.57 ± 0.01
ϵ_{ISO}	97.36 ± 0.4	97.58 ± 0.02	97.58 ± 0.02
ϵ_{HLT_Mu30}			
$\epsilon_{HLT_DoubleMu7}$			
$\epsilon_{HLT_Mu13_Mu8}$			

Table 14: A_{eff} used for PU correction for photon selection for EB and EE, respectively.

Isolation	EB	EE
Tracker	0.167	0.032
ECAL	0.183	0.090
HCAL	0.062	0.180

Table 15: photon identification scale factors

ECAL	scale factor	lower error	upper error
Endcap+	1.053	0.002	0.004
Barrel	0.999	0.002	0.002
Endcap+	1.040	0.002	0.095

Table 16: Data and simulation yields in $W\gamma \to e\nu\gamma$ channel for 723.9 pb^{-1}.

	cross section(pb)	number of events
$W\gamma \to e\nu\gamma$	21.41	885.5 ± 6.0
$W\gamma \to \tau\nu\gamma$	21.41	26.2 ± 1.1
W+jets	31314	886.5 ± 18.7
Z+jets	3048	210.4 ± 3.2
$Z + \gamma \to ll\gamma$	41.37	35.1 ± 1.0
$t\bar{t}$+jets	157.5	47.3 ± 1.2
$\gamma + jets$	by $\hat{p_T}$	7.8 ± 0.6
QCD	by $\hat{p_T}$	12.4 ± 2.9
$WW \to 2L2Nu$	5.7	7.4 ± 0.4
$WZ \to 3LNu$	0.6	1.6 ± 0.1
$ZZ \to 2L2Nu$	0.06	0.1 ± 0.005
MC(all)		2120.5 ± 20.2
data		2845

Table 17: Data and simulation yields in $W\gamma \to \mu\nu\gamma$ channel for 711 pb^{-1}.

	cross section(pb)	number of events
$W\gamma \to \mu\nu\gamma$	21.41	971.4
$W\gamma \to \tau\nu\gamma$	21.41	28.9
W+jets	31314	1147.4
Z+jets	3048	70.0
$Z + \gamma \to ll\gamma$	101.2	94.5
$t\bar{t}$+jets	157.5	72.2
Incl. μ QCD	84679.3	38.9
$\gamma + jets$	by $\hat{p_T}$	1.2
WW	5.7	10.5
WZ	0.6	2.2
MC (Total)		2480.4
data		3228$\pm$57

Table 18: Fake photon background yields for $W\gamma \to \mu\nu\gamma$ by the ratio and template methods.

Barrel		
Photon E_T, GeV	Background yields (Ratio)	Background yields (Template)
15-20	- $\pm$ - (stat.) $\pm$ - (syst.)	643.7 $\pm$ 23.5 (stat.) $\pm$ - (syst.)
20-25	- $\pm$ - (stat.) $\pm$ - (syst.)	239.3 $\pm$ 14.4 (stat.) $\pm$ - (syst.)
25-30	- $\pm$ - (stat.) $\pm$ - (syst.)	98.3 $\pm$ 9.5 (stat.) $\pm$ - (syst.)
30-40	- $\pm$ - (stat.) $\pm$ - (syst.)	120.1 $\pm$ 10.8 (stat.) $\pm$ - (syst.)
40-60	- $\pm$ - (stat.) $\pm$ - (syst.)	58.9 $\pm$ 7.8 (stat.) $\pm$ - (syst.)
60-500	- $\pm$ - (stat.) $\pm$ - (syst.)	35.5 $\pm$ 7.1 (stat.) $\pm$ - (syst.)
Total	- $\pm$ - (stat.) $\pm$ - (syst.)	1195.8 $\pm$ 32.9 (stat.) $\pm$ - (syst.)
Endcap		
15-20	- $\pm$ - (stat.) $\pm$ - (syst.)	185.5 $\pm$ 9.3 (stat.) $\pm$ - (syst.)
20-25	- $\pm$ - (stat.) $\pm$ - (syst.)	79.0 $\pm$ 6.8 (stat.) $\pm$ - (syst.)
25-30	- $\pm$ - (stat.) $\pm$ - (syst.)	37.2 $\pm$ 4.7 (stat.) $\pm$ - (syst.)
30-40	- $\pm$ - (stat.) $\pm$ - (syst.)	50.6 $\pm$ 5.6 (stat.) $\pm$ - (syst.)
40-60	- $\pm$ - (stat.) $\pm$ - (syst.)	18.6 $\pm$ 4.8 (stat.) $\pm$ - (syst.)
60-500	- $\pm$ - (stat.) $\pm$ - (syst.)	18.9 $\pm$ 5.4 (stat.) $\pm$ - (syst.)
Total	- $\pm$ - (stat.) $\pm$ - (syst.)	389.9 $\pm$ 15.4 (stat.) $\pm$ - (syst.)
Barrel + Endcap		
15-20	- $\pm$ - (stat.) $\pm$ - (syst.)	829.3 $\pm$ 25.3 (stat.) $\pm$ - (syst.)
20-25	- $\pm$ - (stat.) $\pm$ - (syst.)	318.3 $\pm$ 15.9 (stat.) $\pm$ - (syst.)
25-30	- $\pm$ - (stat.) $\pm$ - (syst.)	135.5 $\pm$ 10.6 (stat.) $\pm$ - (syst.)
30-40	- $\pm$ - (stat.) $\pm$ - (syst.)	170.7 $\pm$ 12.2 (stat.) $\pm$ - (syst.)
40-60	- $\pm$ - (stat.) $\pm$ - (syst.)	77.5 $\pm$ 9.2 (stat.) $\pm$ - (syst.)
60-500	- $\pm$ - (stat.) $\pm$ - (syst.)	54.3 $\pm$ 9.0 (stat.) $\pm$ - (syst.)
Total	- $\pm$ - (stat.) $\pm$ - (syst.)	1585.7 $\pm$ 36.3 (stat.) $\pm$ - (syst.)

Table 19: Fake photon background yields for $W\gamma \to e\nu\gamma$ by the ratio and template methods.

Barrel		
Photon E_T, GeV	Background yields (Ratio)	Background yields (Template)
15-20	- $\pm$ - (stat.) $\pm$ - (syst.)	369.2 $\pm$ 15.0 (stat.) $\pm$ - (syst.)
20-25	- $\pm$ - (stat.) $\pm$ - (syst.)	177.2 $\pm$ 10.7 (stat.) $\pm$ - (syst.)
25-30	- $\pm$ - (stat.) $\pm$ - (syst.)	70.7 $\pm$ 6.7 (stat.) $\pm$ - (syst.)
30-40	- $\pm$ - (stat.) $\pm$ - (syst.)	80.4 $\pm$ 8.0 (stat.) $\pm$ - (syst.)
40-60	- $\pm$ - (stat.) $\pm$ - (syst.)	58.4 $\pm$ 6.7 (stat.) $\pm$ - (syst.)
60-500	- $\pm$ - (stat.) $\pm$ - (syst.)	24.3 $\pm$ 5.2 (stat.) $\pm$ - (syst.)
Total	- $\pm$ - (stat.) $\pm$ - (syst.)	780.1 $\pm$ 22.8 (stat.) $\pm$ - (syst.)
Endcap		
15-20	- $\pm$ - (stat.) $\pm$ - (syst.)	154.8 $\pm$ 8.3 (stat.) $\pm$ - (syst.)
20-25	- $\pm$ - (stat.) $\pm$ - (syst.)	76.5 $\pm$ 6.4 (stat.) $\pm$ - (syst.)
25-30	- $\pm$ - (stat.) $\pm$ - (syst.)	40.0 $\pm$ 4.8 (stat.) $\pm$ - (syst.)
30-40	- $\pm$ - (stat.) $\pm$ - (syst.)	38.9 $\pm$ 5.6 (stat.) $\pm$ - (syst.)
40-60	- $\pm$ - (stat.) $\pm$ - (syst.)	40.0 $\pm$ 6.3 (stat.) $\pm$ - (syst.)
60-500	- $\pm$ - (stat.) $\pm$ - (syst.)	9.2 $\pm$ 4.2 (stat.) $\pm$ - (syst.)
Total	- $\pm$ - (stat.) $\pm$ - (syst.)	359.3 $\pm$ 14.9 (stat.) $\pm$ - (syst.)
Barrel + Endcap		
15-20	- $\pm$ - (stat.) $\pm$ - (syst.)	524.0 $\pm$ 17.2 (stat.) $\pm$ - (syst.)
20-25	- $\pm$ - (stat.) $\pm$ - (syst.)	253.6 $\pm$ 12.5 (stat.) $\pm$ - (syst.)
25-30	- $\pm$ - (stat.) $\pm$ - (syst.)	110.7 $\pm$ 8.2 (stat.) $\pm$ - (syst.)
30-40	- $\pm$ - (stat.) $\pm$ - (syst.)	119.3 $\pm$ 9.8 (stat.) $\pm$ - (syst.)
40-60	- $\pm$ - (stat.) $\pm$ - (syst.)	98.4 $\pm$ 9.2 (stat.) $\pm$ - (syst.)
60-500	- $\pm$ - (stat.) $\pm$ - (syst.)	33.5 $\pm$ 6.7 (stat.) $\pm$ - (syst.)
Total	- $\pm$ - (stat.) $\pm$ - (syst.)	1139.3 $\pm$ 27.2 (stat.) $\pm$ - (syst.)

Table 20: Summary of background contributions in $W\gamma$ final states for 723.9 pb^{-1}. The quoted fake photon background yield is determined by the ratio method.

Background source	Background yield in 723.9 pb^{-1}	
	$e\nu\gamma$	$\mu\nu\gamma$
Fake photons	1139.3 $\pm$ 27.2 (stat.) $\pm$ - (syst.)	1585.7 $\pm$ 36.3 (stat.) $\pm$ - (syst.)
Fake leptons	negligible	negligible
Fake photons (misid. electrons)	449.0 $\pm$ 47.4 (stat.) $\pm$ - (syst.)	- $\pm$ - (stat.) $\pm$ - (syst.)
$W(\tau\nu)\gamma$	26.2 $\pm$ 1.1 (stat.) $\pm$ - (syst.)	28.9 $\pm$ - (stat.) $\pm$ - (syst.)
$Z\gamma$	32.8 $\pm$ 1.2 (stat.) $\pm$ - (syst.)	94.5 $\pm$ - (stat.) $\pm$ - (syst.)

Table 21: Summary of systematic uncertainties for the $W\gamma$ cross section measurement.

		$e\nu\gamma$	$\mu\nu\gamma$
Source	Systematic uncertainty	Effect on $\mathcal{F} = A \cdot \epsilon_{MC}$	
Electron energy scale	0.07% 0.04% (EB), 0.22% 0.18% (EE)	0.2%	n/a
Electron energy resolution	1.48% 2.02% (EB), 5.01% 3.91% (EE)	0.2%	n/a
Muon p_T scale	1%	n/a	-%
Muon p_T resolution	1%	n/a	-%
Photon energy scale	0.07% 0.04% (EB), 0.22% 0.18% (EE)	0.1%	-%
Photon energy resolution	1.48% 2.02% (EB), 5.01% 3.91% (EE)	0.1%	-%
Pileup		-%	-%
PDF		-%	-%
Total uncertainty on $\mathcal{F} = A \cdot \epsilon_{MC}$		-%	-%
Source	Systematic uncertainty	Effect on ρ_{eff}	
Electron trigger	0.05% 0.37% (EB), 0.1% 0.72% (EE)	0.02%	n/a
Electron reconstruction	0.05% 0.13% (EB), 0.02% 0.2% (EE)	0.03%	n/a
Electron ID and isolation	0.17% 0.7% (EB), 0.35% 3.6% (EE)	0.13%	n/a
Muon trigger	0.5%	n/a	-%
Muon reconstruction	0.2%	n/a	-%
Muon ID and isolation	0.2%	n/a	-%
$\not{E}_{\mathrm{T}}$ selection	1.2%(e) 1.2%(μ)	-%	-%
Photon ID and isolation	0.8% (EB), 3.3% (EE)	-%	-%
Total uncertainty on ρ_{eff}		-%	-%
Source	Systematic uncertainty	Effect on background yield	
Background estimation	6.7% (EB), 15.6% (EE) 6.2% (EB), 18.3% (EE)	-%	-%
Source	Systematic uncertainty	Effect on luminosity	
Luminosity	6.0%	6.0%	6.0%

Table 22: Summary of parameters for the $W\gamma \to e\nu\gamma$ cross section measurement.

Parameter	Number
N_{events}	2845 $\pm$ 53.3 (stat.)
N_{bkg}^{Wjet}	1139.3 $\pm$ 27.2 (stat.) $\pm$ - (syst.)
$N_{bkg}^{ee\mathrm{X}}$	449.0 $\pm$ 47.4 (stat.) $\pm$ - (syst.)
$N_{bkg}^{W(\tau\nu)\gamma}$	26.2 $\pm$ 1.1 (stat.) $\pm$ - (syst.)
$N_{bkg}^{Z\gamma}$	32.8 $\pm$ 1.2 (stat.) $\pm$ - (syst.)
N_S	1197.7 $\pm$ 76.4 (stat.) $\pm$ - (syst.)
$A \cdot \epsilon_{MC,W\gamma\to\ell\nu\gamma}$	0.0361 $\pm$ - (syst.)
ρ_{eff}	1.009 $\pm$ - (syst.)
$\int \mathcal{L}\, dt$	723.9 $\pm$ 43.4 (syst.)

Table 23: Background yields for $W\gamma$ process in the muon channel.

Background source	yield
Fake photons (template method)	1585.7 $\pm$ 36.3
$Z\gamma$ (MC)	94.5 $\pm$ - (stat.) $\pm$ - (syst.)
$W\gamma \to \tau\nu_\tau\nu_\mu\gamma$ (MC)	28.9 $\pm$ - (stat.) $\pm$ - (syst.)
Dibosons (MC)	147.3 $\pm$ - (stat.) $\pm$ - (syst.)
QCD (MC)	38.9 $\pm$ - (stat.)
Total background events	1895.3 $\pm$ - (stat.) $\pm$ - (syst.)

Table 24: Parameters used to calculate the $W\gamma$ cross-section in the muon channel.

Parameters	$W\gamma \to \mu\nu\gamma$
N_{events}	3228 $\pm$ 57 (stat.)
$N_{bkg}^{\text{Fake photons}}$	1585.7 $\pm$ 36.3
$N_{bkg}^{Z\gamma}$	94.5
$N_{bkg}^{W\gamma\to\tau\nu_\tau\nu_\mu\gamma}$	28.9
$N_{bkg}^{\text{Dibosons}}$	147.3
N_{bkg}^{QCD}	38.9 (stat.)
N_S	1332.7
$A \cdot \epsilon_{MC}$	0.0389
ρ_{eff}	0.993
$\int \mathcal{L}\, dt$	711
$\sigma(pp \to W\gamma \to \mu\nu\gamma + X)$	48.59

Table 25: Summary of parameters for the $W\gamma$ cross section measurement.

Parameters	$W\gamma \to e\nu\gamma$	$W\gamma \to \mu\nu\gamma$
$N_{observed}$	2845 $\pm$ 53.3 (stat.)	3228 $\pm$ 57 (stat.)
$N_{background}$	1647.3 $\pm$ 54.7 (stat.) $\pm$ - (syst.)	1895.3 $\pm$ - (stat.) $\pm$ - (syst.)
$A \cdot \epsilon_{MC,W\gamma\to\ell\nu\gamma}$	0.0361 $\pm$ - (syst.)	0.0389 $\pm$ - (syst.)
ρ_{eff}	1.009 $\pm$ - (syst.)	0.993 $\pm$ - (syst.)
$\int \mathcal{L}\, dt$	723.9 $\pm$ 43.4 (syst.)	711 $\pm$ 4.2 (syst.)

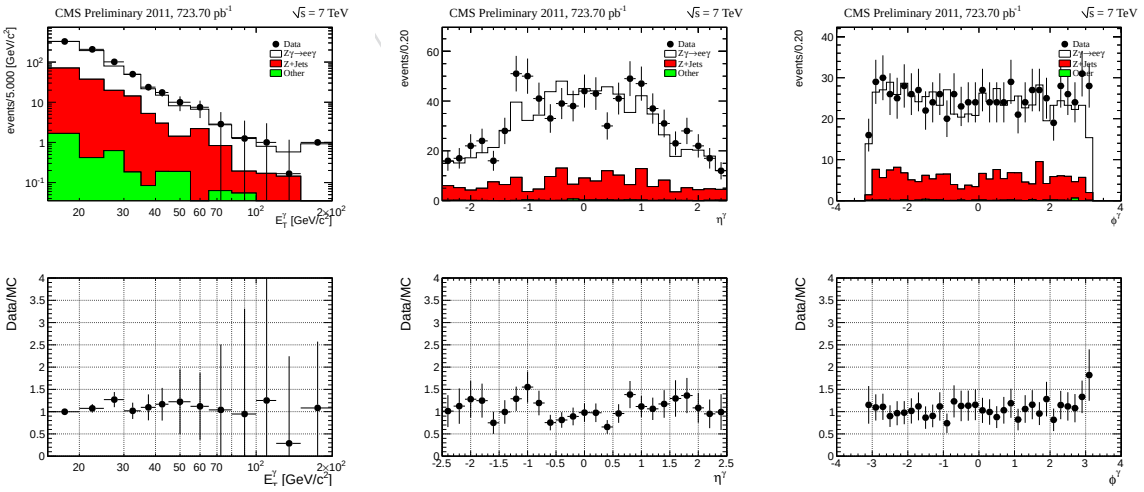

Figure 22: Photon candidate E_T spectrum (left), photon pseudorapidity (middle), photon ϕ distribution (right), for data (black dots), Zγ signal (white histogram), Z/γ^*+jets and other backgrounds are given as red and green filled hisograms respectively.

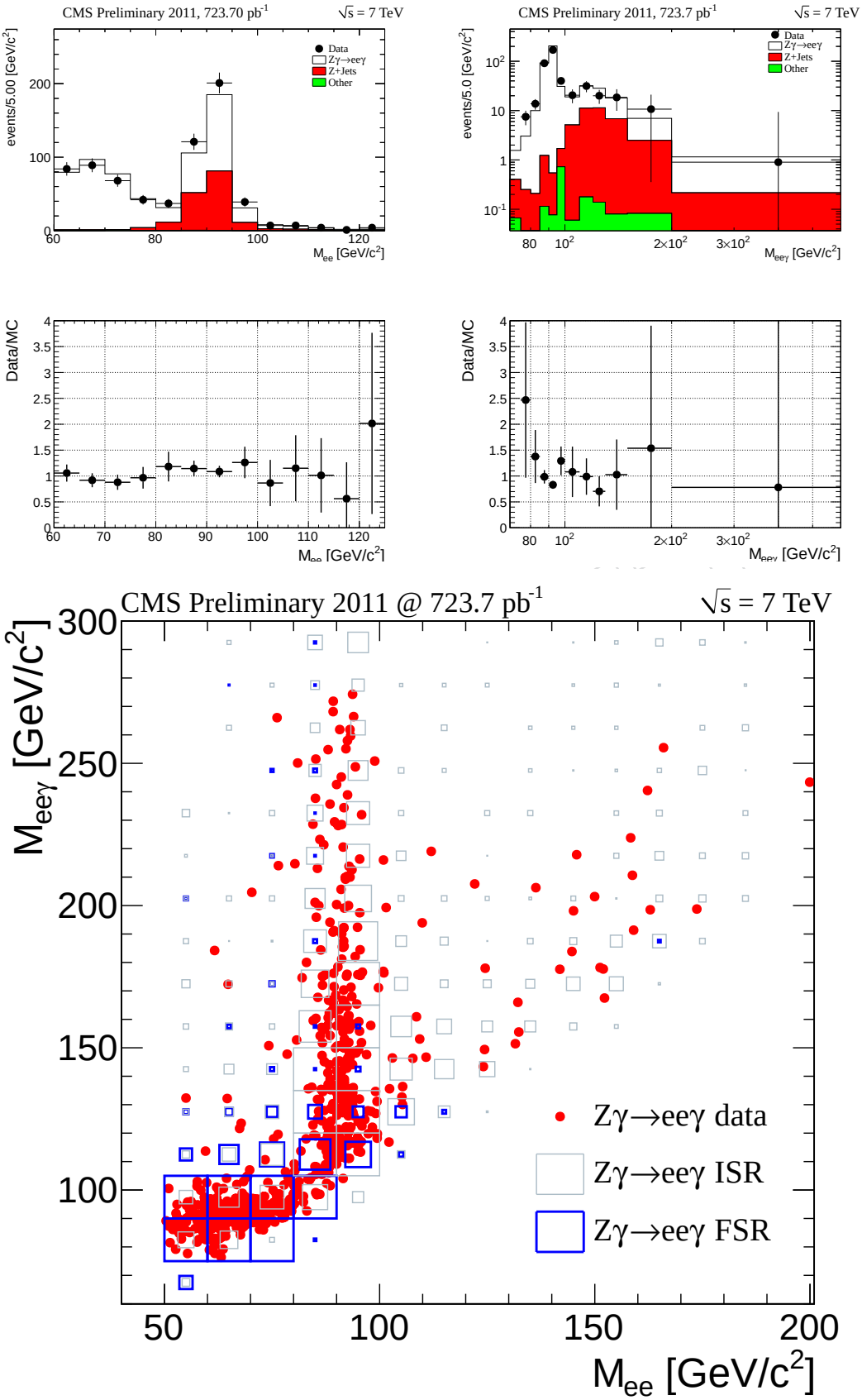

Figure 23: Di-electron invariant mass (left), di-electron + photon invariant mass (right), two-dimensional plot (bottom).

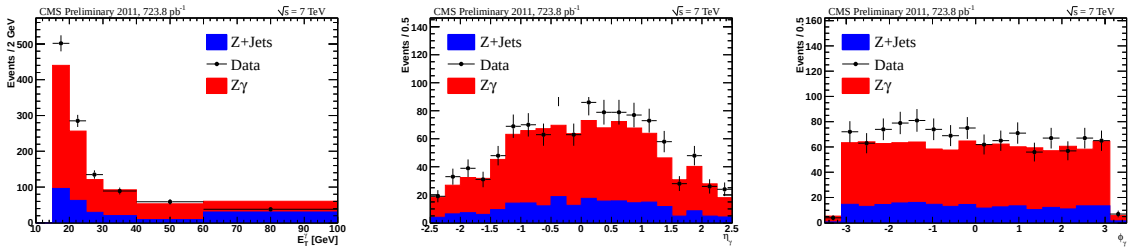

Figure 24: Photon candidate E_T spectrum (left), photon pseudorapidity (middle), photon ϕ distribution (right), for data (black dots), $Z\gamma$ signal (white histogram), Z/γ^*+jets and other backgrounds are given as red and green filled hisograms respectively.

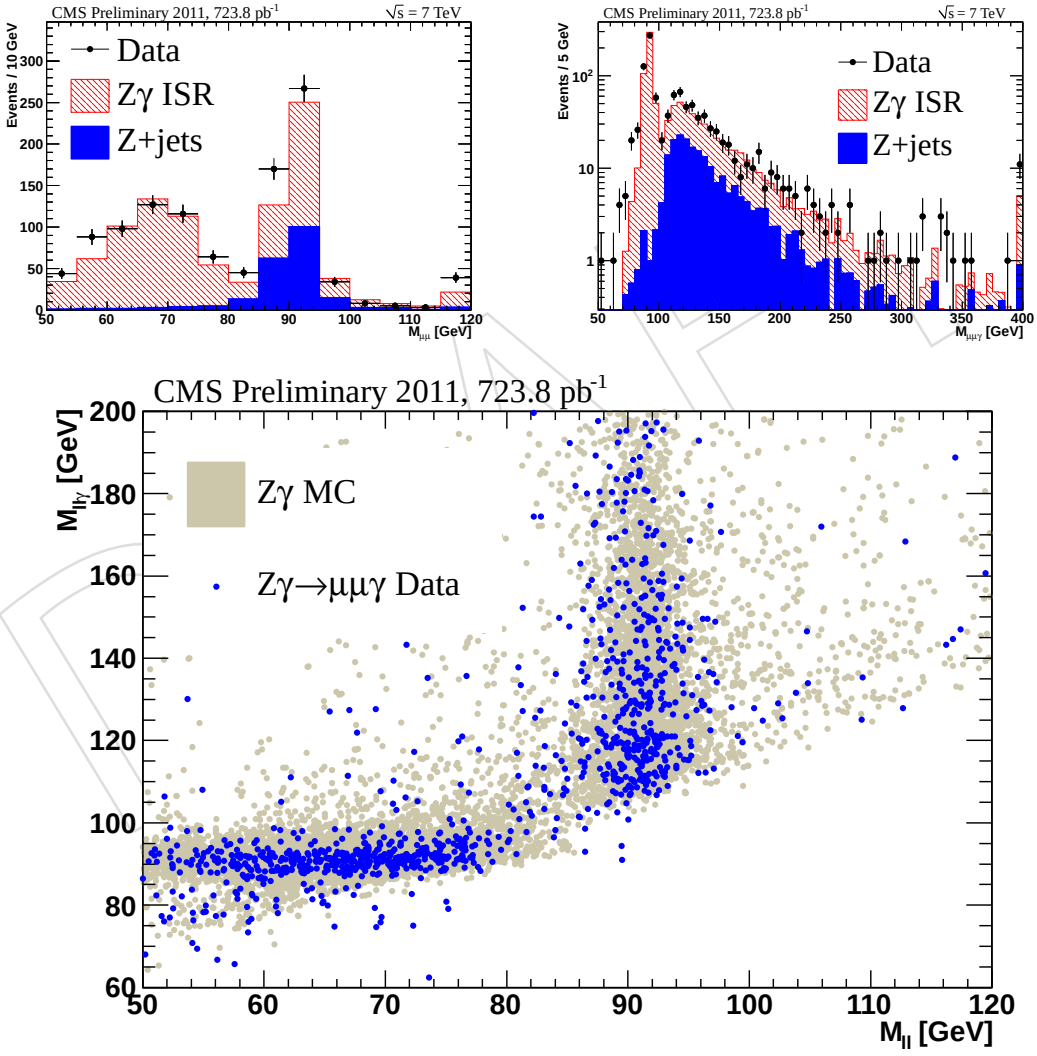

Figure 25: Di-muon invariant mass (left), di-muon + photon invariant mass (right), two-dimensional plot (bottom).

Table 26: Z/γ^*+jets background estimation for the template method compared to MC truth. The uncertainty for the data-driven method is statistical and systematic, while the MC truth uncertainty is statistical only.

	$Z\gamma \to ee\gamma$		$Z\gamma \to \mu\mu\gamma$	
ECAL	Template	MC truth	Template	MC truth
Barrel	118.2 ± 10.3 (stat.)	87.19 ± 2.4	168.0 ± 8.5 (stat.) ± 27.5 (syst.)	128.8 ± 7.7
Endcap	47.2 ± 19.1 (stat.)	33.81 ± 1.5	48.4 ± 5.1 (stat.) ± 0.5 (syst.)	48.4 ± 6.8
Total	165.4 ± 21.7 (stat.)	121.0 ± 2.8	217.1 ± 13.5 (stat.) ± 28.0 (syst.)	177.2 ± 14.5

6 Objectives of the "Ratio" Photon Fake Method

For events where the leading two photon candidates are really jets, we find the ratio $\frac{f}{e}$. We define the probability, f, that a jet from such an event will be observed as a tight-photon. The probability that a jet from such an event will be observed as a fake-able object is defined as e. This ratio can be utilized to estimate the amount of jet-jet contamination in a di-photon sample, either where both photon candidates pass tight selection, or where one passes tight selection and the other is a fake-able object. This may have the advantage over other photon fake rate methods of incorporating the correct quark to gluon fraction of dijet and multijet events. Here we calculate $\frac{f}{e}$ for several p_T ranges, where both photon candidates are in the same p_T bin, and both photon candidates are in the barrel.

The ratio $\frac{f}{e}$ can be used in the following ways:

- To estimate the number of jets contaminating a single photon sample, first select fake-able objects using the definitions below. Then multiply the number of fake-able objects by f/e to find the number of jets passing tight photon selection. This will be the number of jets contaminating the photon signal sample.
- To evaluate the number of tight-tight events [1] which have both tight photons coming from jets within a p_T range: First count the number of fake-fake events for that p_T range. This is the number of events where the sub-leading photon candidates both pass the fake-able object selection, are both in the barrel or both in the end cap, and both in this p_T range. The next step is to multiply this count by $\left(\frac{f}{e}\right)^2$ to get the number of tight-tight events that had both tight objects originate from a jet.
- To evaluate the number of tight-fake events [2] which have the tight photon coming from jets within a p_T range: First count the number of fake-fake events [3] within a p_T range. It should be noted that real photons do not result in fake-able objects. Second, multiply this count by $2 \cdot \frac{f}{e}$ to get the number of tight-fake events that had both tight objects originate from a jet. The factor of 2 to account for the combinatorics.

7 Description of the Photon Fake Method

We start by selecting several p_T ranges of interest. In this case we have chosen: 32-37, 37-42. 42-48, 48-54, 54-62, 62-70, 70-85, 85-100, and 100-120 GeV. The upper most bin is not used for the end cap since the sideband runs out of statistics. First, in the data we count the number of fake-fake events for each range, where both fakes are in the barrel or both in the end cap. Photons should never be observed as fake-able objects so we are confident that they are from jets. This gives us the number of jet-jet events that result in fake-fake events (n_{JJ-FF}).

We then consider tight-fake events [2]. For the tight photon selection we apply no $\sigma_{i\eta i\eta}$ cut since this distribution is used later for fitting using a template method. This sample is a combination of photon + jet events and jet+jet events where one jet passes tight photon cuts. We determine

[1] A tight-tight event: when both the leading and sub-leading photon candidates pass tight selection, are in the barrel, and are both in the p_T range.

[2] A tight-fake event: when either the leading OR the sub-leading photon candidate passed the tight selection criteria and the other passed fake selection criteria. Again, both objects are required to be in the barrel or both in the end cap, and both in the relevant p_T range.

[3] A fake-fake event is one where the leading and sub-leading photon candidates both pass the fake-able object selection, are both in the barrel, or both in the end cap, and both in this p_T range.

how many events came from each contribution using a $\sigma_{i\eta i\eta}$ template method. For each p_T bin we fit the $\sigma_{i\eta i\eta}$ distribution of the tight photon in the data with a background fake template and a signal photon template. We then integrate the fit templates up to the tight photon $\sigma_{i\eta i\eta}$ cut to determine how many events from the signal and background distributions pass the full tight selection. This gives us the number of jet-jet events that result in a tight-fake event (n_{JJ-TF}). The probability that a jet-jet event results in tight-fake event is $2 \cdot f \cdot e$ while the probability that jet-jet event results in fake-fake event is e^2. So if there were, in truth, N_{JJ} jet-jet events, then $n_{JJ-TF} = 2 \cdot f \cdot e \cdot N_{JJ}$ and $n_{JJ-FF} = e^2 \cdot N_{JJ}$. Then $\frac{f}{e} = \frac{1}{2} \cdot \frac{n_{JJ-TF}}{n_{JJ-FF}}$.

7.1 Data and MC Samples Used

A total of 1085.57 1/pb of 2011 data is used. All data ntuples were produced using CMSSW_4_2_5 and ggNtuplizer version V04-01-05-07. The Monte Carlo was produced in CMSSW_4_2_3 using ggNtuplizer version V04-01-05-05.

```
Data:
/Photon/Run2011A-DiPhoton-May10ReReco-v1/RAW-RECO dataset (201.16 1/pb)
/castor/cern.ch/user/c/cmkuo/ggNtuple/425_V04-01-05-07/job_photon_2011a_May10rereco_May27_JSON.root

/Photon/Run2011A-PromptReco-v4/AOD dataset (0.49 1/pb, 768.72 1/pb, 115.20 1/pb respectively)
/castor/cern.ch/user/c/cmkuo/ggNtuple/425_V04-01-05-07/job_photon_2011a_May10rereco_aod_Jul6_JSON.root
/castor/cern.ch/user/c/cmkuo/ggNtuple/425_V04-01-05-07/job_photon_2011a_PR_v4_Jul1_JSON_noskim.root
/castor/cern.ch/user/c/cmkuo/ggNtuple/425_V04-01-05-07/job_photon_2011a_PR_v4_Jul6_JSON_noskim.root


Summer 2011 MC:
/GluGluToHToGG_M-115_7TeV-powheg-pythia6/Summer11-PU_S3_START42_V11-v2/AODSIM
Castor Directory /castor/cern.ch/user/c/cmkuo/ggNtuple/423_V04-01-05-05/job_ggH_115.root
```

7.2 Trigger Selection

All data is subject to the trigger requirements. For the May10 ReReco, we used:

```
HLT_DoublePhoton33
HLT_Photon36_CaloIdL_Photon22_CaloIdL
HLT_Photon32_CaloIdL_Photon26_CaloIdL
HLT_Photon75_CaloIdVL
```

Due to unavailable HLT information, HLT_DoublePhoton33 was not used for the Jul6_JSON ntuple. HLT_Photon36_CaloIdL_Photon22_CaloIdL was not used for the May10rereco_aod_Jul6_JSON ntuple. And HLT_Photon32_ CaloIdL_Photon26_CaloIdL was not used for the Jul1_JSON or the Jul6_JSON ntuples.

7.3 The Tight Barrel Photon Templates

We use $H \to \gamma\gamma$ Monte Carlo to generate the signal photon $\sigma_{i\eta i\eta}$ templates. We fill the templates with leading and sub-leading photons that originated from a higgs (phoGenGMomPID==25) and passed tight photon cuts except for the $\sigma_{i\eta i\eta}$ cut. We observe that the signal templates have no events over the $\sigma_{i\eta i\eta}$ cut anyway. The passing photons then fill the template histogram for the appropriate p_T range.

7.4 Fake-Fake counting

From the data we count events where the leading and sub-leading photon candidates pass the fake-able object selection and be in the same p_T bin, and are both in the barrel or both in the end cap.

7.5 The Fake Template

We first require that the event have at least two photon candidates, and neither have a pixel seed. We then fill the template histograms with the $\sigma_{i\eta i\eta}$ of the leading and sub-leading photon candidates that pass a modified fake-able object selection. Both objects are required to either both be in the barrel or both in the end cap. The modified fake-able object selection differs from the usual fake-able object selection only in that we do not specifically select objects over the $\sigma_{i\eta i\eta}$ cut so as to not bias the template shape.

7.6 The Data Template

Here we required that one of the two leading and sub-leading photon candidates is a fake-able object while the other passes the tight photon cuts except for the $\sigma_{i\eta i\eta}$ cut. Both objects are required to be in the barrel or both in the end cap, and in the same p_t range. We then fill the corresponding histogram with the $\sigma_{i\eta i\eta}$ of the tight photon.

Figure 27 shows the $\sigma_{i\eta i\eta}$ distributions for the tight photon in the barrel tight-fake sample and template fits for several p_T ranges, for the fitted MC photon signal template (blue), the fitted fake-able object template (magenta), and the sum of the signal and background templates (red). Figure 28 shows the same end cap tight-fake sample.

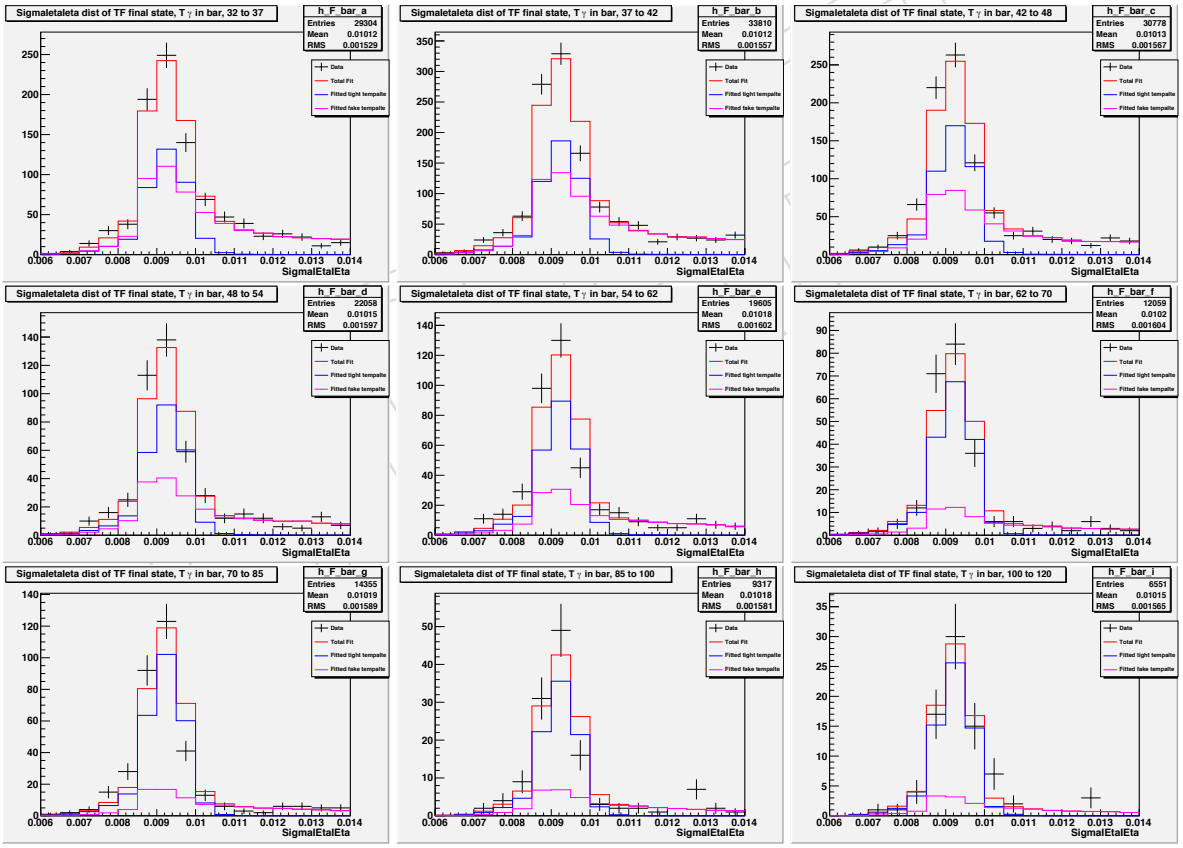

Figure 27: The $\sigma_{i\eta i\eta}$ distributions for the tight object in the barrel tight-fake sample and template fits for nine p_T ranges. In blue are the fitted MC photon signal template. In magenta are the fitted fake-able object template. In red is the sum of the signal and background templates.

7.7 Fake-able Object and Tight Object Definitions

These definitions use a $\sigma_{i\eta i\eta}$ cut of 0.011 in order to preserve the $\sigma_{i\eta i\eta}$ side band.

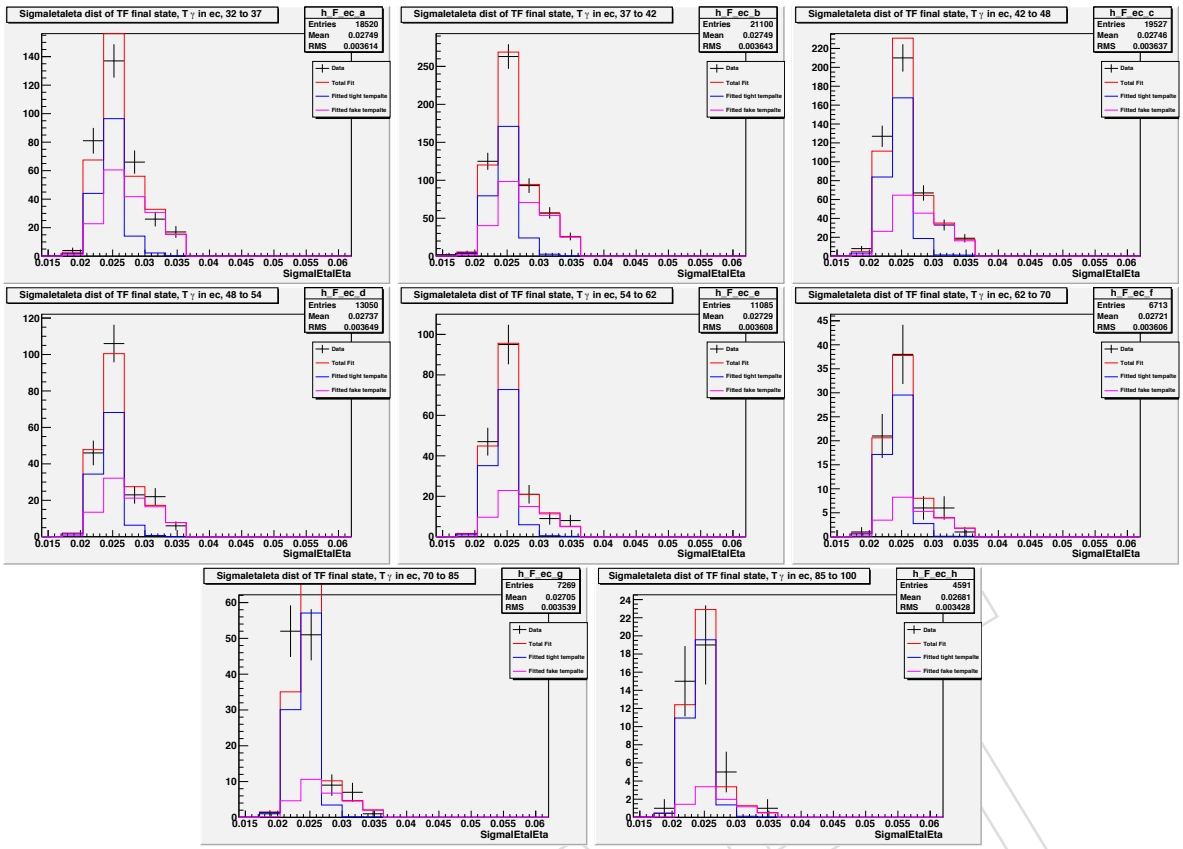

Figure 28: The $\sigma_{i\eta i\eta}$ distributions for the tight object in the end cap tight-fake sample and template fits for eight p_T ranges. In blue are the fitted MC photon signal template. In magenta are the fitted fake-able object template. In red is the sum of the signal and background templates.

```
Tight photon Definition:
For the Barrel   |phoEta| < 1.4442
 phoHoverE < 0.05 &&
 phohasPixelSeed == 0 &&
 phoTrkIsoHollowDR04  < 2.0+0.001*phoEt + 0.167*rho25 &&
 phoEcalIsoDR04  < 4.2+0.006*phoEt + 0.183*rho25 &&
 phoHcalIsoDR04  < 2.2+0.0025*phoEt + 0.062*rho25 &&
 phoSigmaIEtaIEta< 0.011

For the End Cap: 1.566 < |phoEta | < 2.6
   phoHoverE < 0.05 &&
   phohasPixelSeed == 0 &&
   phoTrkIsoHollowDR04  < 2.0+0.001*phoEt + 0.032*rho25 &&
   phoEcalIsoDR04   < 4.2+0.006*phoEt + 0.090*rho25 &&
   phoHcalIsoDR04   < 2.2+0.0025*phoEt + 0.180*rho25 &&
   phoSigmaIEtaIEta <0.030


Fake-able object Definition:
For the Barrel   |phoEta| < 1.4442

 phoHoverE < 0.05 &&
 phoSigmaIEtaIEta < 0.014 &&
 phoTrkIsoHollowDR04 < Min(5*(3.5 + 0.001*phoEt + 0.167*rho25), 0.2* phoEt) &&
 phoEcalIsoDR04 < Min( 5*(4.2 + 0.006*phoEt + 0.183*rho25), 0.2* phoEt) &&
 phoHcalIsoDR04 < Min( 5*(2.2 + 0.0025*phoEt + 0.062*rho25), 0.2* phoEt) &&
 (
       phoSigmaIEtaIEta > 0.011 or
       phoTrkIsoHollowDR04 > (3.5 + 0.001*phoEt + 0.167*rho25) or
       phoEcalIsoDR04 > (4.2+ 0.006*phoEt + 0.183*rho25) or
```

```
       phoHcalIsoDR04 > (2.2 + 0.0025*phoEt + 0.062*rho25)
 )

For the End Cap: 1.566 < |phoEta | < 2.6

phoHoverE < 0.05 &&
phoSigmaIEtaIEta <0.035 &&
phoTrkIsoHollowDR04 < Min( 5*(3.5 + 0.001 * phoEt + 0.032*rho25), 0.2* phoEt) &&
phoEcalIsoDR04 < Min( 5*(4.2+0.006* phoEt + 0.090*rho25 ), 0.2* phoEt) &&
phoHcalIsoDR04 < Min( 5*(2.2+0.0025* phoEt + 0.180*rho25), 0.2* phoEt) &&
(
       phoSigmaIEtaIEta >0.030 or
       phoTrkIsoHollowDR04 > (3.5 + 0.001 * phoEt + 0.032*rho25) or
       phoEcalIsoDR04 > ( 4.2+ 0.006 * phoEt + 0.090*rho25) or
       phoHcalIsoDR04 > (2.2 + 0.0025 * phoEt + 0.180*rho25)
)
```

8 Results

We evaluated the $\frac{f}{e}$ fake rates for several p_T ranges and are summarized in Table 29 and in Figure 29 for the barrel, and Table 31 and in Figure 30 for the end cap. We fit the $\frac{f}{e}$ fake rate vs. p_T to the functional form $\frac{f}{e} = p0 + \frac{p1}{p_T^{p2}}$. The fit parameters are listed in Table 30 and Table 32 for the barrel and end cap respectively.

The errors listed below are statical errors that do not account for the systematic uncertainty in the choice of Monte Carlo photon template. It is clear from Figure 27 that the Monte Carlo template does conform to the asymmetry of the peak in the $\sigma_{i\eta i\eta}$ distribution of tight barrel photons.

In 2010 (see AN2010_365_v3) a 20% systematic uncertainty was recommended to account for the variation in the photon fake rates derived from various methods. This 20% systematic uncertainty should be assumed for here as well on top of the statistical errors listed below.

photon E_{T} (GeV)	f/e
32-37	0.392 ± 0.035
37-42	0.223 ± 0.017
42-48	0.147 ± 0.013
48-54	0.116 ± 0.015
54-62	0.078 ± 0.011
62-70	0.053 ± 0.011
70-85	0.044 ± 0.008
85-100	0.048 ± 0.013
100-120	0.027 ± 0.010

Table 29: $\frac{f}{e}$ fake rates for barrel objects for several E_{T} ranges. The errors are statistical only.

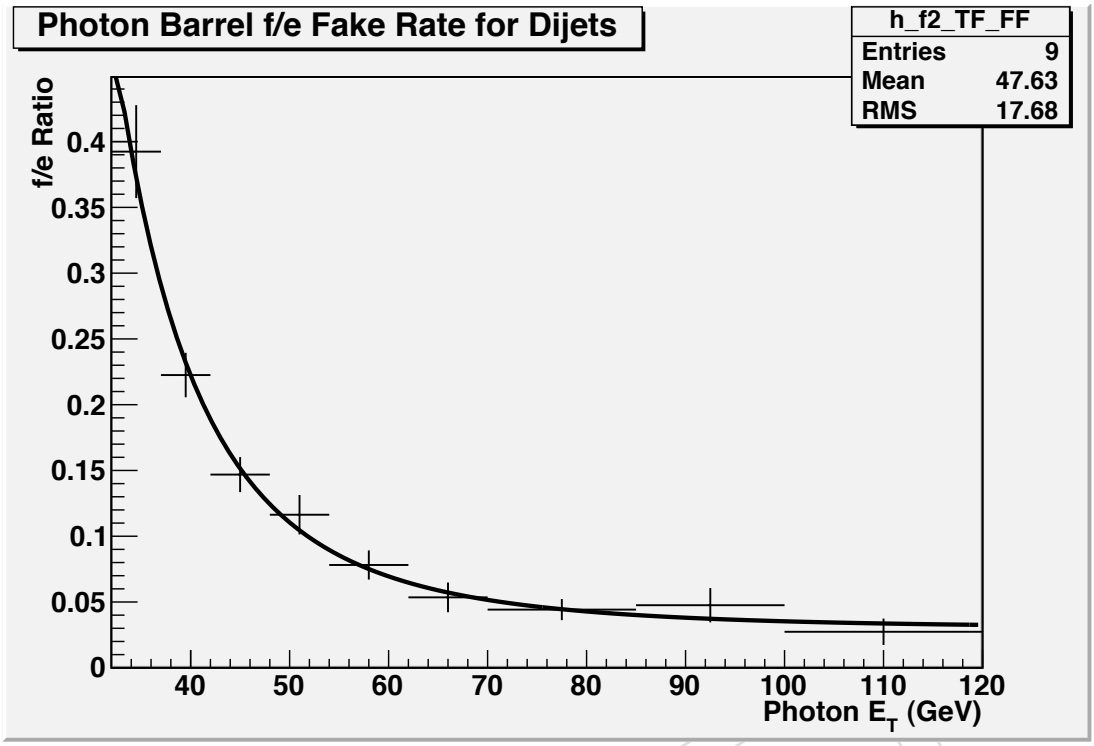

Figure 29: $\frac{f}{e}$ fake rates for the barrel for nine p_T ranges and a fitted curve of the form $\frac{f}{e} = p0 + \frac{p1}{p_T^{p2}}$ with parameters given in Table 30.

9 The Unbinned Template Method for Determining Photon Fake Rate

The template method from last year's analysis [12] has also been implemented this year with one major improvement. In this revision of the method, signal and background templates used are smoothed using kernel density estimation [13] or direct interpolation, in the case of high statistics for the template, to allow for unbinned fits of the $\sigma_{i\eta i\eta}$ distribution of selected photons to be performed. This change represents an improvement in the statistical error on the with respect to the binned template method. Additionally, studies can be performed to assess the true size of the systematic errors coming from differences in template shape between data and monte carlo.

To verify this update to the template method a monte carlo closure test was performed using the Summer11 MC samples. The test was performed by creating templates using signal and background template selections similar to those in data. The resulting unbinned templates were fit to a properly weighted mixture of Wγ and W+Jets events, accounting for pileup reweighting. We found that, to within errors, the unbinned template method agrees with the central value

NAME	VALUE	ERROR
p_0	3.0e-02 $\pm$ 0.8e-02	
p_1	3.45e+05 $\pm$ 6.2e+05	
p_2	3.904 $\pm$ 0.49	

Table 30: Barrel misidentification rate $\frac{f}{e} = p0 + \frac{p1}{p_T^{p2}}$ fit parameters

phoEt Range (GeV)	f/e
32-37	0.321 ± 0.050
37-42	0.189 ± 0.021
42-48	0.138 ± 0.018
48-54	0.128 ± 0.024
54-62	0.097 ± 0.022
62-70	0.055 ± 0.020
70-85	0.052 ± 0.017
85-100	0.044 ± 0.028

Table 31: $\frac{f}{e}$ fake rates for end cap objects for several p_T ranges. The errors are statistical only.

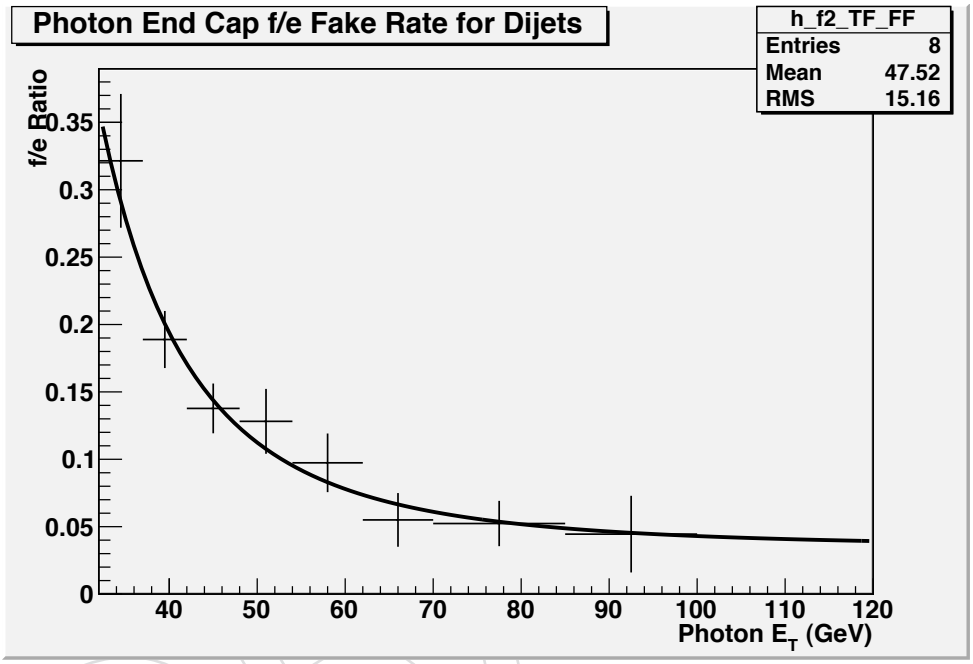

Figure 30: $\frac{f}{e}$ fake rates for the end cap for eight p_T ranges and a fitted curve of the form $\frac{f}{e} = p0 + \frac{p1}{p_T^{p2}}$ with parameters given in Table 32.

673 predicted by monte carlo (31) with the exception of two bins in the endcap.

674 The compatibility of the fake rate method using a data driven template, selection as in 2010
675 analysis, in data between the barrel and endcap regions of the ECAL was also examined. We
676 find that the fake rate estimation differs significantly for low p_T in the endcaps. This difference
677 is attributed to more stringent selection cuts for photons in the endcaps 32.

NAME	VALUE
p0	3.5e-02 $\pm$ 2.6e-02
p1	2.23e+04 $\pm$ 9.1e+04
p2	3.212 $\pm$ 1.15

Table 32: End cap rake rate fit parameters. $\frac{f}{e} = p0 + \frac{p1}{p_T^{p2}}$

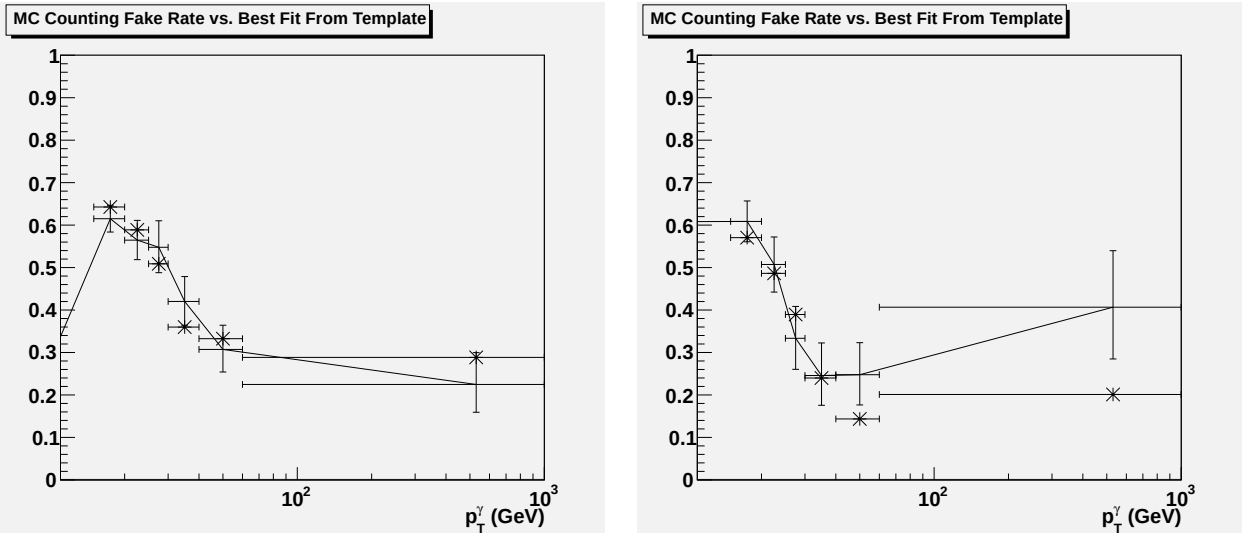

Figure 31: Results of the MC closure test in the barrel and endcaps using Summer 11 MC. Connected points are from the unbinned fit while starred points are the expectation from MC.

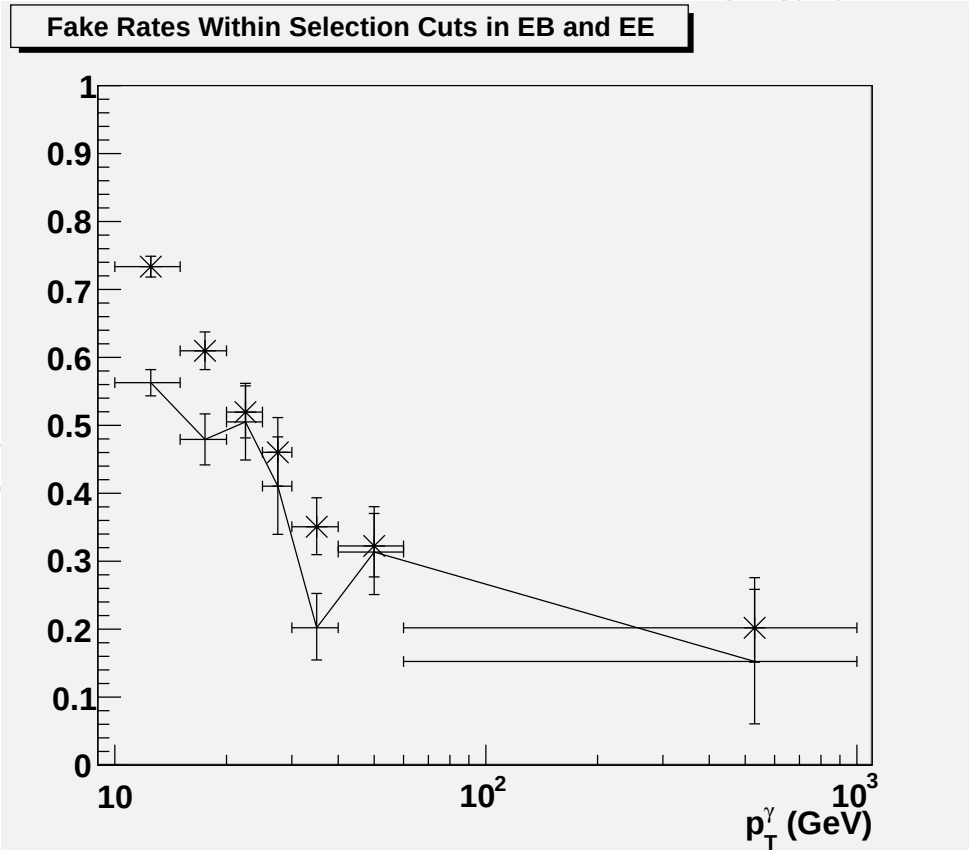

Figure 32: Results of using a data driven background template to fit Wγ events with photons in the ECAL barrel (starred) and endcap (connected). The endcap has systematically less background than the barrel due to more stringent photon ID requirements.

10 Measuring photon identification efficiency using Final State Radiation

Photon candidates from the FSR Z$\rightarrow \mu\mu\gamma$ process have the smallest background contamination from the Z+jets production due to an invariant mass constraint on the dimuon plus photon invariant mass. By requiring the dimuon mass below the nominal Z boson mass, we implicitely require a photon to be radiated off a muon. This requirement significantly reduces Z+jets contribution to a negligible level. In this study, we use FSR Zγ candidate events to cross check the photon selection efficiency obtained from MC studies and from studies of Z$\rightarrow ee$ process.

We select the FSR Zγ candidates by selecting a pair of muon candidates that satisfy the following selection criteria

- $p_{\mathrm{T}} > 20$ GeV and $|\eta| < 2.4$
- Number of pixel hits > 0
- Number of tracker hits > 10
- χ^2/n.d.f < 10
- Number of muon hits > 0
- Number of chambers with matched segments > 1
- vertex $d_0 < 0.02$ cm
- vertex $dz < 0.1$ cm

We also require the invariant mass of the dimuon candidate events to be between 30 and 82 GeV. The selected events are further required to have a photon candidate with $E_{\mathrm{T}} > 15$ GeV and $|\eta| < 2.5$. Photons from Zγ FSR process tend to be collinear to the direction of the radiating muon (see Fig. 33), and the latter spoils the photon isolation requirements (see Fig. 34).

To improve the photon selection efficiency, we modify the photon isolation by removing the muon inner transverse momentum from the photon's tracking isolation. We also remove the muon energy deposition in photon's ECAL and HCAL isolation. This procedure has a negligible impact on the backgrounds from Z+jets processes but significantly improves the efficiency of Zγ FSR selection criteria.

To esitmate the efficiency of a given photon identification requirement we estimate the number of the FSR Zγ candidate events before and after applying a given criterion by fitting the dimuon plus photon invariant mass to a Crystal Ball function convoluted with a Gaussian distribution for signal and sum of two Gaussian distributions for background. An example of such fits are given in Fig 35.

The final results for the photon ID efficiency are shown in Fig. 36. The efficiencies with respect to the different components of the photon ID can be found in Appendix **??**. The results from data are shown together with those obtained using the same method in Monte Carlo simulation, as well as those obtained with the Monte Carlo truth. Averaged over the photon E_{T},

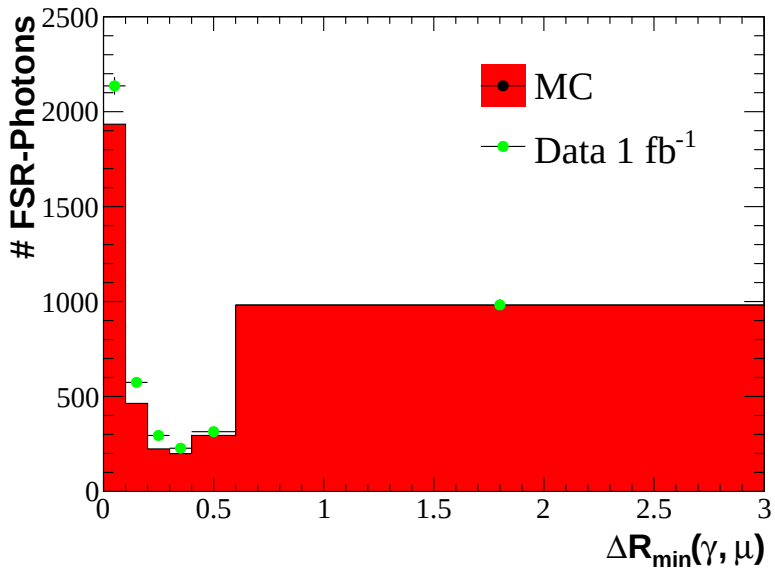

Figure 33: Spatial separation between photon and muon candidates from Zγ FSR production.

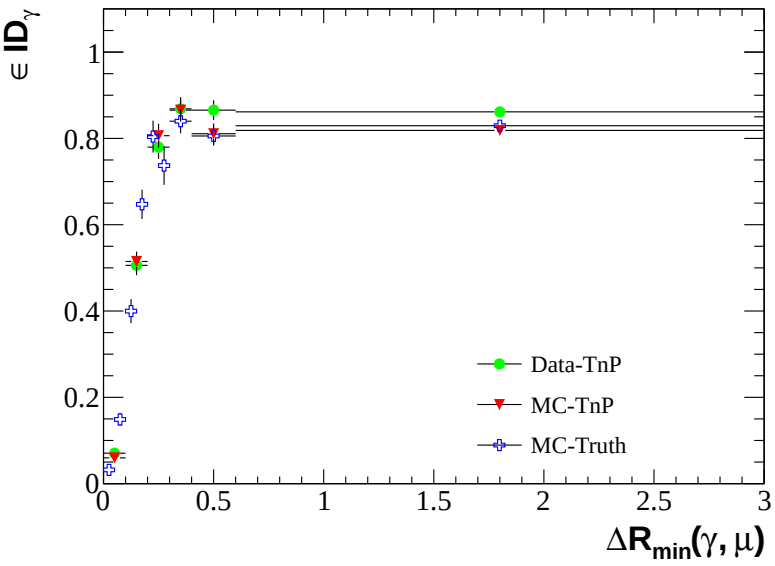

Figure 34: $\Delta R_{\mathrm{min}}(\mu, \gamma)$ dependency of photon ID.

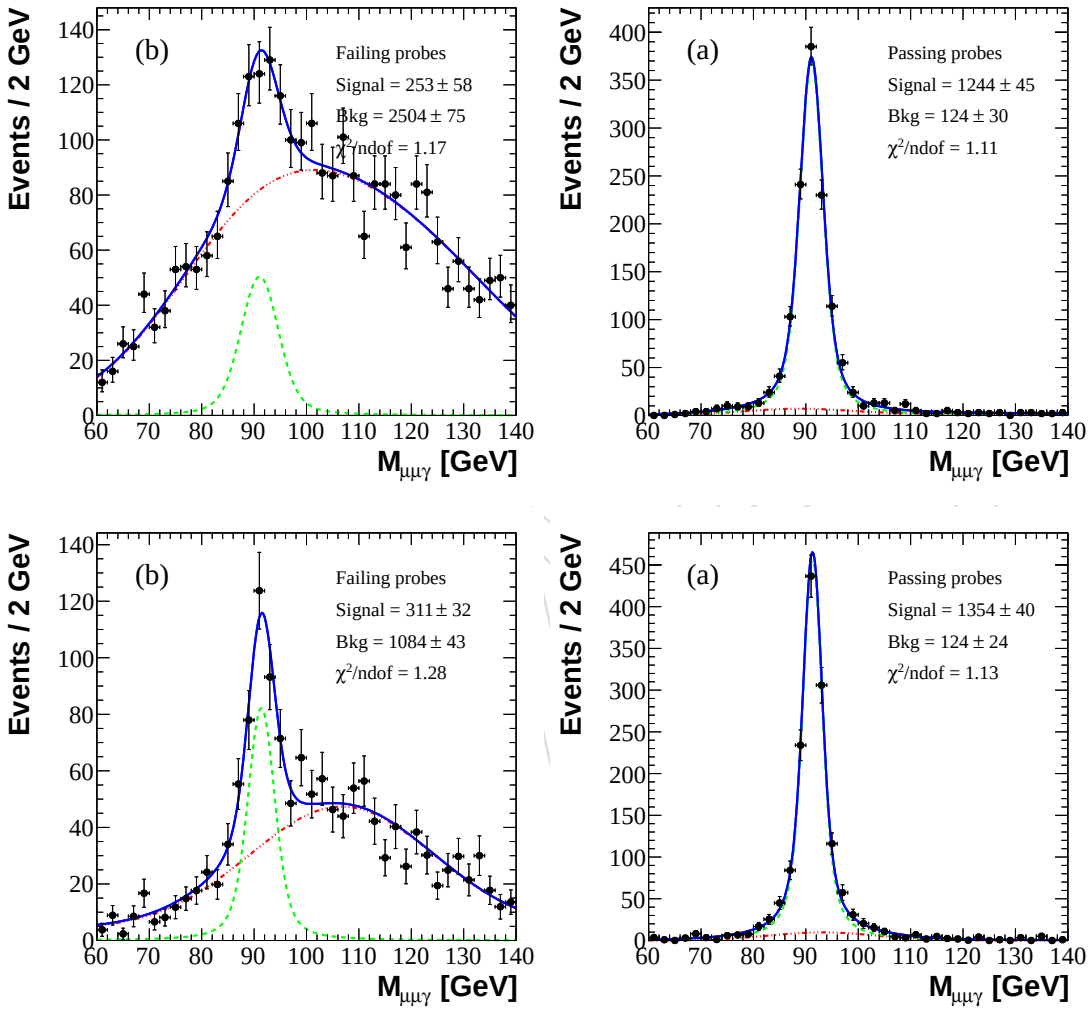

Figure 35: Top: Fit to $m_{\mu\mu\gamma}$ distribution in data for passing (a) and failing (b) photon candidates. Bottom: Fit to the same in Monte Carlo simulation for passing (a) and failing (b) probes.

we measure the photon identification efficiency of $(83.0 \pm 1.0)\%$ in data and $(81.0 \pm 1.0)\%$ in MC simulation, where the uncertainty is statistical. The systematic uncertainty is estimated to be 3% due to modeling of the background shape of the dimuon plus photon invariant mass distribution.

graphicx subfig

11 Distribution of Helicity Angles

Several other kinematic quantities characterize the $Z\gamma$ final state. These include the helicity angles, $\theta_Z, \phi_Z, \theta_{\ell^+}, \phi_{\ell^+}$. The first two represent the polar and azimuthal angles of the Z-boson in the $Z\gamma$ rest frame. The last two denote the polar and azimuthal angles of the positively charged lepton in the rest frame of the Z-boson. The quantity $\psi = \phi_{\ell^+} - \phi_Z$ can be interpreted as the angle between the $Z\gamma$ production plane and the Z decay plane.

Figures 38, 39 and 40 compare the distributions of $\cos\theta_Z$, $\cos\theta_{\ell^+}$, and ψ observed in the data to those predicted by the standard model. The agreement between data and Monte Carlo verifies detailed aspects of the CMS efficiency corrections.

A future analysis will extract the helicity parameters underlying these angular distributions. The helicity analysis may be sensitive to interference effects not present in the distributions of photon p_T.

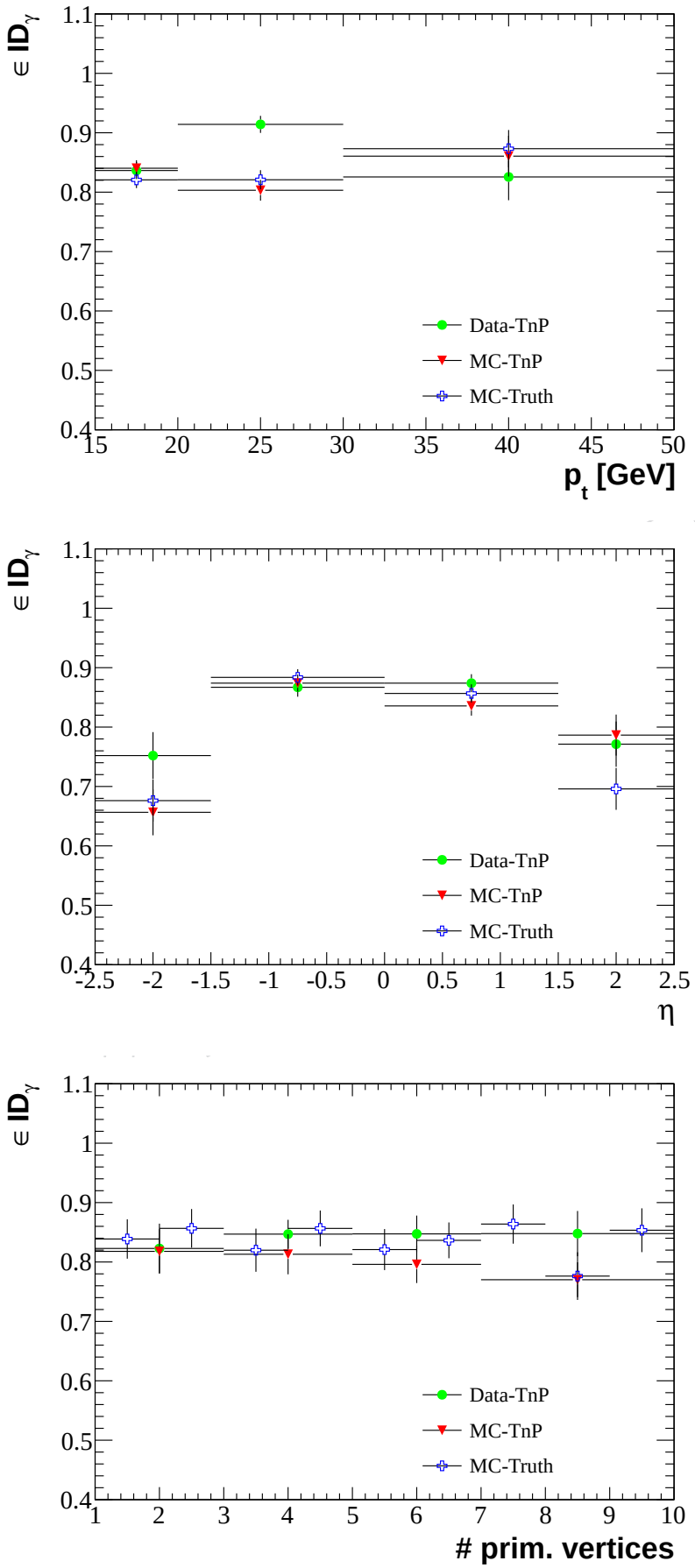

Figure 36: Photon identification efficiency as a function of photon E_{T}, η and the number of primary vertices.

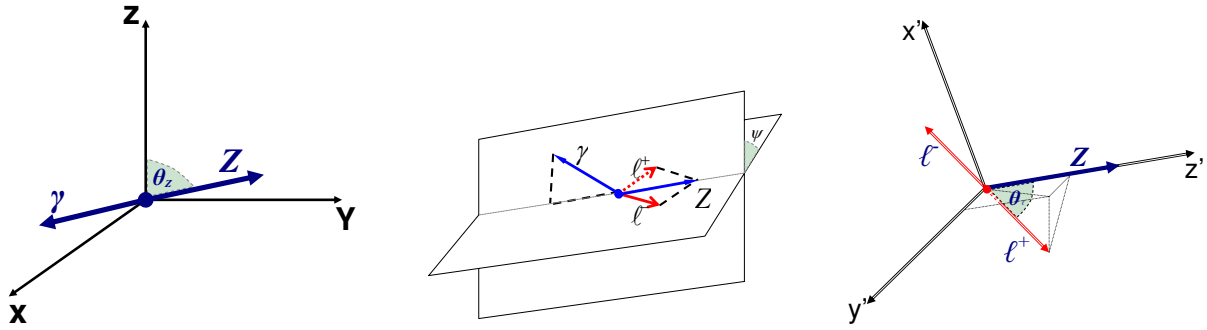

(a) Production helicity angle (θ_Z) in the rest frame of Zγ

(b) Angle (ψ) between Zγ production and Z decay planes

(c) Decay helicity angle (θ_ℓ) in the rest frame of Z boson

Figure 37: Description of Angles

A MCFM - Madgraph comparison for $W\gamma$ channel

MC $W\gamma$ sample is generated using Madgraph generator and contains up to 1 jet. However, Madgraph generator does not contain virtual loop. New MCFM generator (MCFM 6.0) can provide both LO and NLO cross section and also contains both FSR and ISR processes.

In this section, we compare the generator level information for the Wγ channel between MCFM and Madgraph generators.

The following cuts were used for production in both generators:

- photon $E_T^\gamma > 10$ GeV,
- lepton $p_T^l > 35$ GeV,
- MET ¿ 25 GeV,
- $|\eta^e| < 2.5$ and $|\eta^\gamma| < 2.5$,
- the photon must be spatially separated by $\Delta R_{l,\gamma} > 0.7$ from either lepton,
- for the Madgraph generator sample, we apply a minimum jet transverse momentum cut of 10 GeV.

MCFM used *CTEQ6L1* PDF set for LO and *CTEQ66M* PDF set for NLO. Madgraph used *CTEQ6L1* PDF set. Both generators used running scale.

The cross sections calculated by MCFM and Madgraph generators are given in Table 33. The k-factor as a function of photon transverse momentum is calculated by MCFM and shown in Fig.41.

The comparison plots for LO between MCFM and Madgraph Wγ+0Jet can be seen in Fig. 42 for the photon transverse momentum(P_T^γ), pseudorapidity (η^γ), $\Delta R_{l,\gamma}$, electron transverse momentun (P_T^e), pseudorapidity (η^e) distributions.

The comparison plots for NLO between MCFM and Madgraph Wγ+0Jet can be seen in Fig. 43 for the photon transverse momentum(P_T^γ), pseudorapidity (η^γ), $\Delta R_{l,\gamma}$, electron transverse momentun (P_T^e), pseudorapidity (η^e) distributions. Madgraph Wγ+0Jet distributions are normalized to the k-factor as a function of photon transverse momentum.

The comparison plots for NLO between MCFM and Madgraph Wγ+1Jet can be seen in Fig. 44 for the photon transverse momentum(P_T^γ), pseudorapidity (η^γ), $\Delta R_{l,\gamma}$, electron transverse momentun (P_T^e), pseudorapidity (η^e) distributions. Madgraph Wγ+0Jet distributions are normalized to MCFM NLO cross section and the k-factor as a function of photon transverse momen-

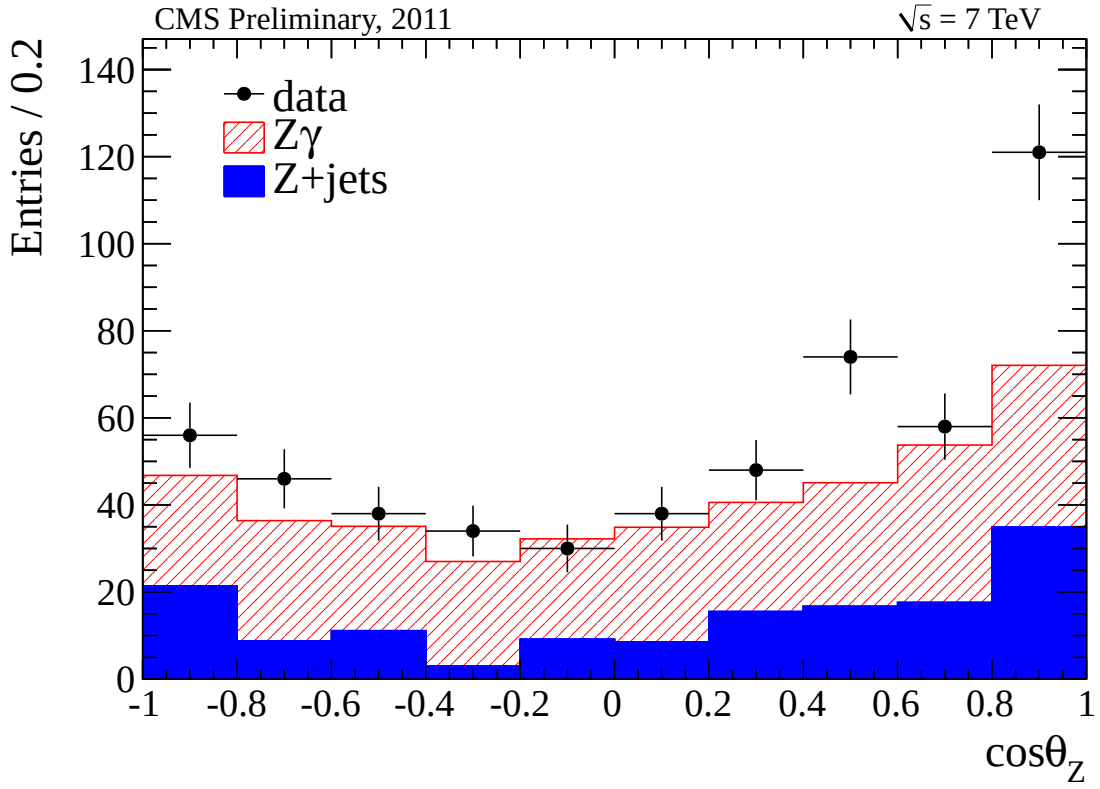

Figure 38: Comparison between data and SM prediction for $\cos\theta_Z$

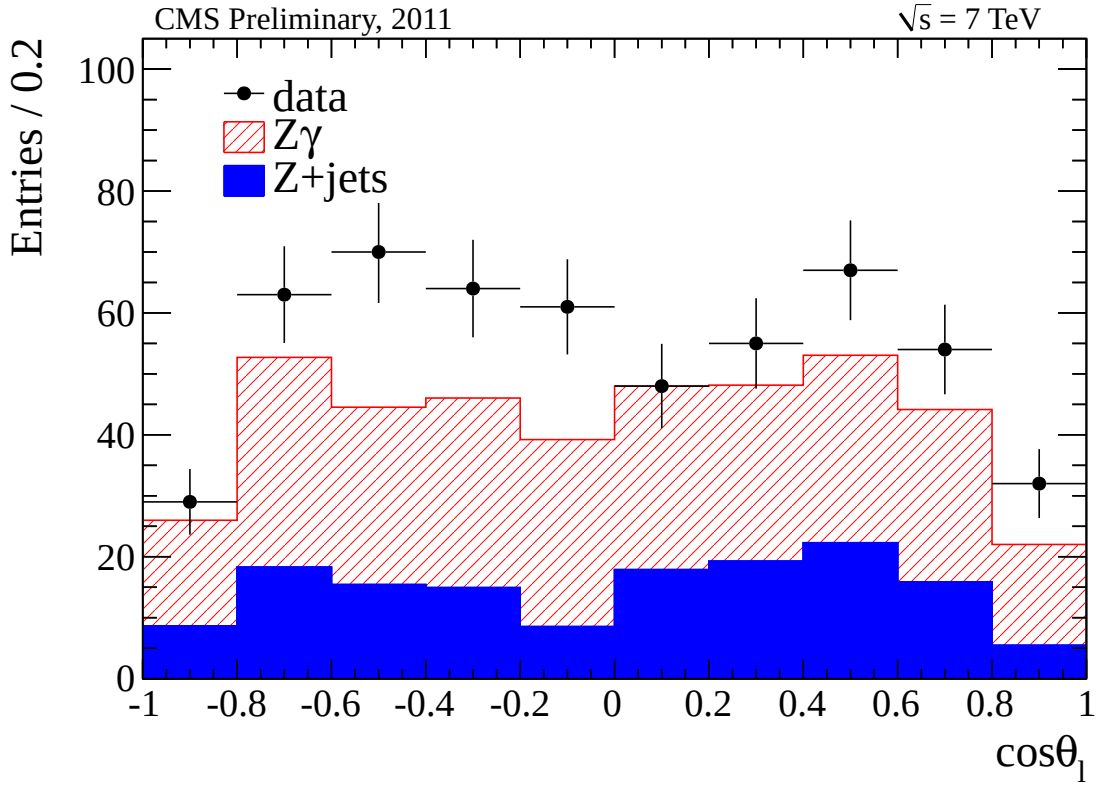

Figure 39: Comparison between data and SM prediction for $\cos\theta_\ell$

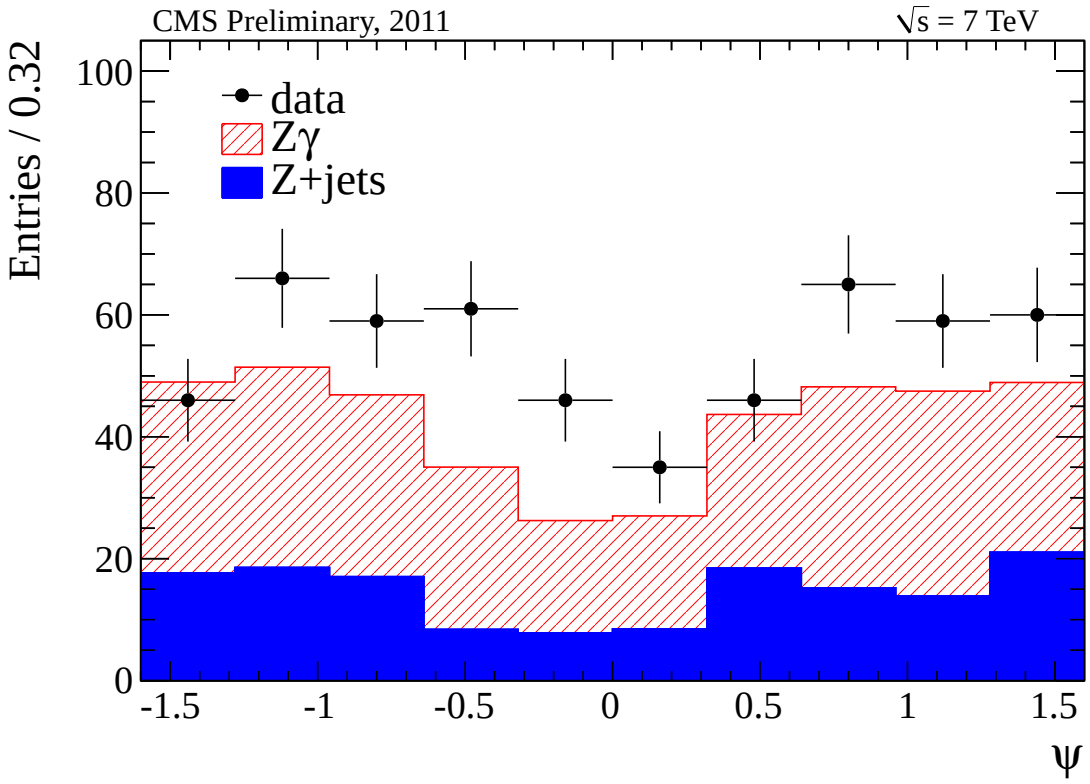

Figure 40: Comparison between data and SM prediction for ψ

Table 33: Cross sections estimated by the MCFM and Madgraph generators for the $W(\rightarrow e\nu)\gamma$ channel. The jet multiplicity numbers are exclusive.

NLO σ_{MCFM}	LO σ_{MCFM}	LO $\sigma_{Madgraph+0Jets}$
3.57 pb	1.71 pb	1.78 pb

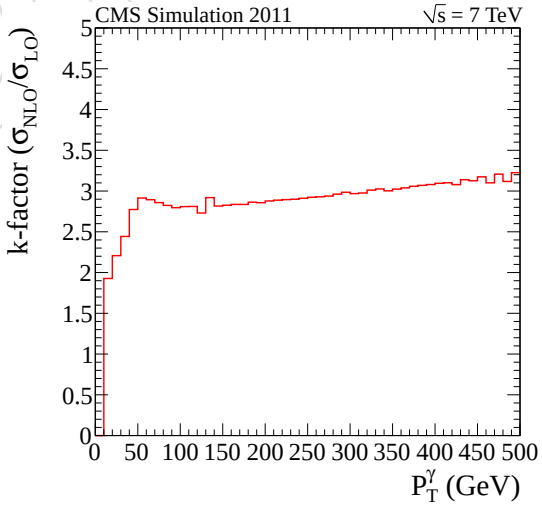

Figure 41: The k-factor as a function of photon transverse momentum.

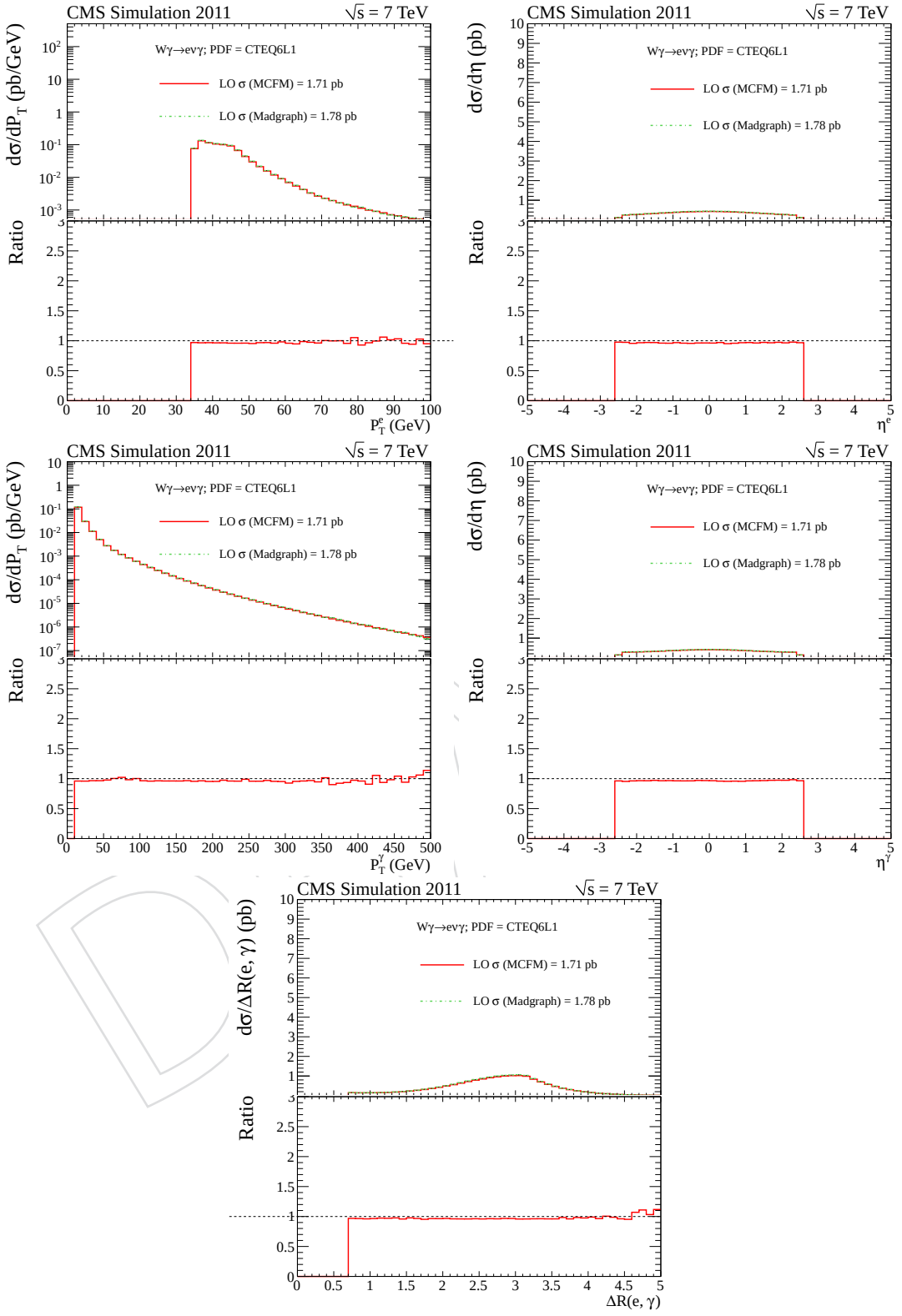

Figure 42: The distributions of Electron candidate E_T, pseudorapidity, photon candidate E_T, pseudorapidity, and $\Delta R(e, \gamma)$. MCFM results are shown in red line and Madgraph results are shown in green dash line.

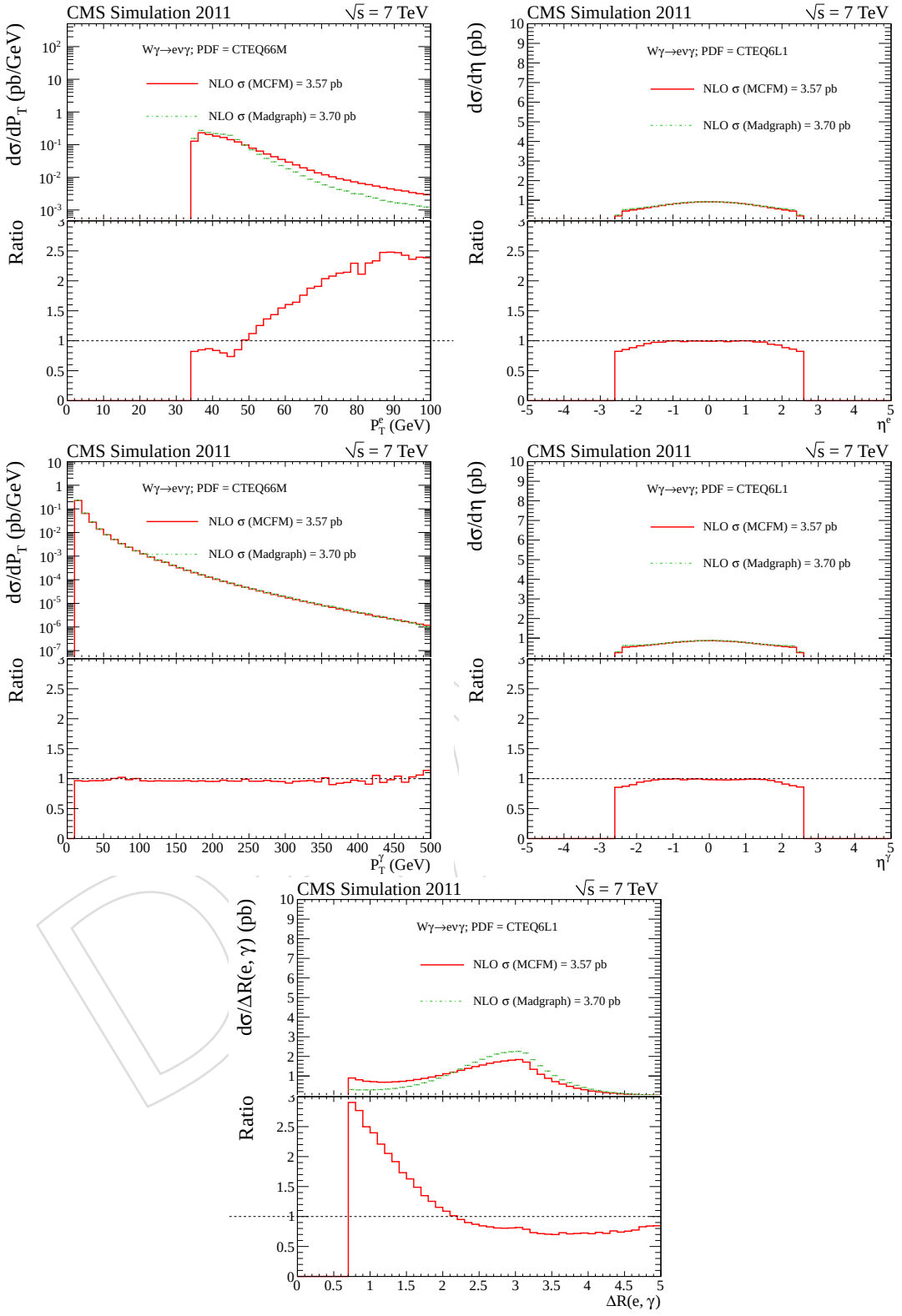

Figure 43: The distributions of Electron candidate E_T, pseudorapidity, photon candidate E_T, pseudorapidity, and $\Delta R(e, \gamma)$. MCFM results are shown in red line and Madgraph results are shown in green dash line.

769 tum, respectively.

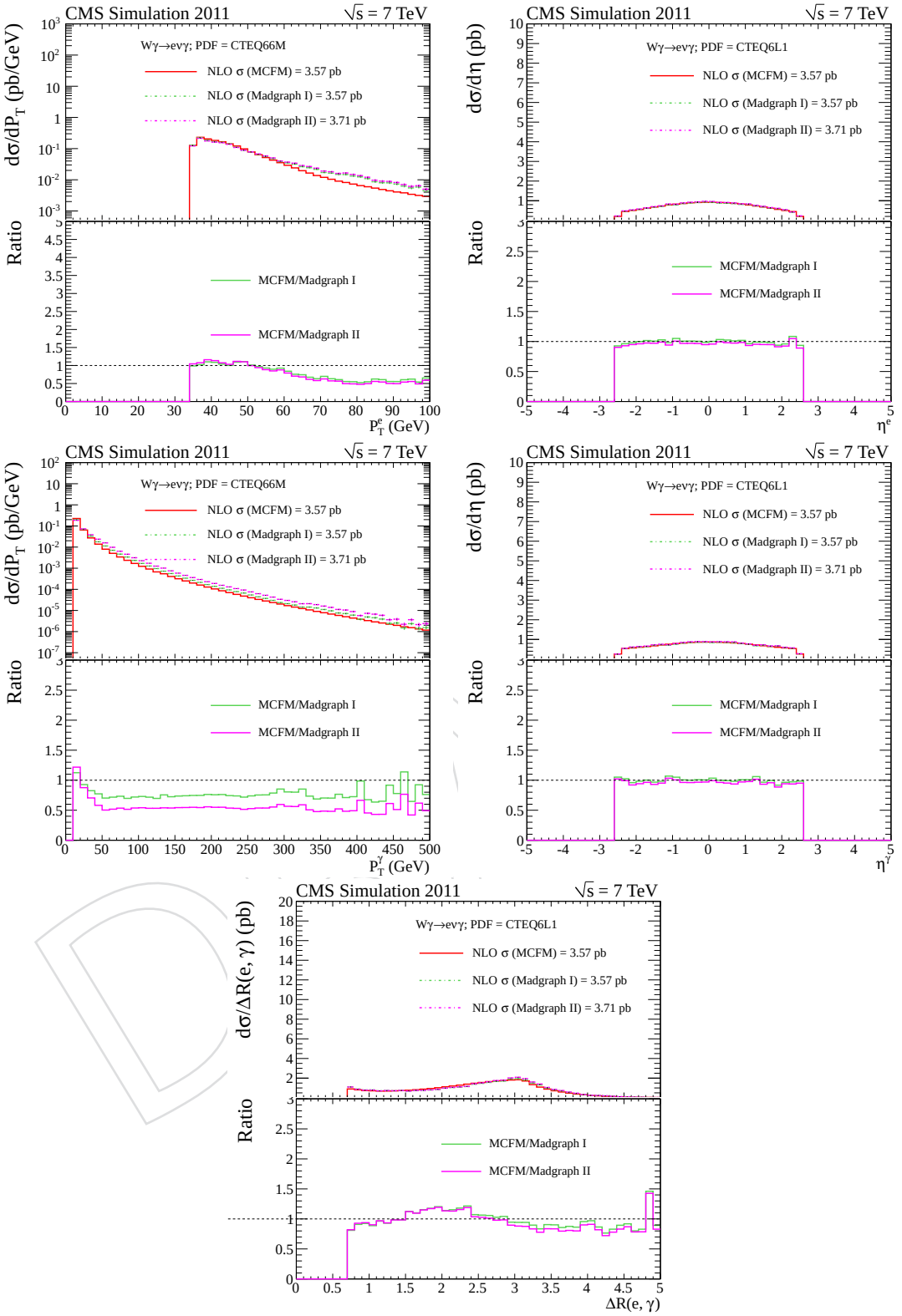

Figure 44: The distributions of Electron candidate E_T, pseudorapidity, photon candidate E_T, pseudorapidity, and $\Delta R(e, \gamma)$. MCFM results are shown in red line. Madgraph results normalized to MCFM NLO cross section are shown in green dash line. Madgraph results normalized to k-factor are shown in pink dash line.

References

[1] LEP Electroweak Working Group Collaboration, "A combination of preliminary electroweak measurements and constraints on the standard model", *arXiv:hep-ex/0412015v2* (2004).

[2] L3 Collaboration, "Measurement of energetic single photon production at LEP", *Phys. Lett. B* **346** (1995) 190.

[3] L3 Collaboration, "Study of the $e^+e^- \to Z\gamma$ process at LEP and limits on triple neutral-gauge-boson couplings", *Phys. Lett. B* **597** (2004) 119.

[4] OPAL Collaboration, "Study of Z pair production and anomalous couplings in e^+e^- collisions at $\sqrt{s}$ between 190 GeV and 209 GeV", *Eur. Phys. J. C* **32** (2003) 303.

[5] D0 Collaboration, "Measurement of $p\bar{p} \to W\gamma + X$ cross section at $\sqrt{s} = 1.96$ TeV and $WW\gamma$ anomalous coupling limits", *Phys. Rev. D* **71** (2005) 091108.

[6] D0 Collaboration, "First study of radiation-amplitude zero in $W\gamma$ production and limits on anomalous $WW\gamma$ couplings at $\sqrt{s} = 1.96$ TeV", *Phys. Rev. Lett* **100** (2008) 241805.

[7] D0 Collaboration, "Combined measurements of anomalous charged trilinear gauge-boson couplings from diboson production in p-pbar c ollisions at $sqrt(s) = 1.96$ TeV", *arXiv:hep-ex/0907.4952v2* (2009).

[8] CDF Collaboration, "Measurement of $Z\gamma$ production in $p\bar{p}$ collisions at $\sqrt{s} = 1.96$ TeV", *Phys. Rev.* **D82** (2010) 031103.

[9] D0 Collaboration, "$Z\gamma$ production and limits on anomalous $ZZ\gamma$ and $Z\gamma\gamma$ couplings in $p\bar{p}$ collisions at $\sqrt{s} = 1.96$ TeV", *Phys. Lett. B* **653** (2007) 378.

[10] D0 Collaboration, "Measurement of the $Z\gamma \to \nu\nu\gamma$ cross section and limits on anomalous $ZZ\gamma$ and $Z\gamma\gamma$ couplings in $p\bar{p}$ collisions at $\sqrt{s} = 1.96$ TeV", *Phys. Rev. Lett.* **102** (2009) 201802.

[11] CMS Collaboration, "Measurement of W^+W^- production and search for the Higgs boson in pp collisions at $\sqrt{s} = 7$ TeV", *Phys. Lett. B* **699** (2011) 25.

[12] CMS Collaboration, "Measurement of $W\gamma$ and $Z\gamma$ production in pp collisions at $\sqrt{s} = 7$ TeV", *Phys. Lett. B* **701** (2011) 535.

[13] K. S. Cranmer, "Kernel estimation in high-energy physics", *Comput. Phys. Commun.* **136** (2001) 198–207, arXiv:hep-ex/0011057. doi:10.1016/S0010-4655(00)00243-5.